Vol. 35/1 & 2
January, 2023

ISRAPS Bulletin

NSRP - 2023
SPECIAL ISSUE

ISRAPS

Guest Editors
Nandita Maiti
Mainak Banerjee

A Publication of
**Indian Society for
Radiation and Photochemical Sciences**

Published by ISRAPS, C/o RPCD, BARC, Mumbai - 400 085

Printed in India
January - 2023

Printed By
Sharda Stationery & Xerox
Shop No. 4, Arjun Centre, Govandi East, Mumbai - 400088
Tel. : 022 2548 0808
Mobile : +91 9869004377
Email : shubhamxerox@gmail.com

Message from the President and Secretary, ISRAPS

Dear ISRAPS members,

Greetings from the Executive Council of ISRAPS for a very happy & prosperous new year 2023!

We take this opportunity to acknowledge the contribution of all the members who have actively participated in organizing various activities of ISRAPS.

As in preceding years, ISRAPS has been actively involved in organizing thematic discussion meetings in the field of radiation and photochemistry. Recently, we have successfully organized ISRAPS One-day Seminar (hybrid mode) on “Emerging Role of Radiation in Nanotechnology: Fundamental to Translational Research” on October 15, 2022, at Shivaji University, Kolhapur, Maharashtra. Experts from leading research groups in the country, delivered talks in their areas of research.

During the last few months our efforts have been directed towards organizing the National Symposium on Radiation and Photochemistry (NSRP-2023), which will be held at BITS Pilani, K. K. Birla Goa Campus, Goa during January 5-7, 2023. On this occasion, ISRAPS has brought out an ISRAPS bulletin (NSRP-2023 special issue) comprising of research articles from eminent scientists invited in NSRP-2023. The Executive council of ISRAPS takes this opportunity to thank all the contributors for making this special issue very enlightening. On behalf of ISRAPS and the Symposium Organizing Committee, we invite all the young researchers to share their knowledge in the advanced areas of radiation and photochemistry in the upcoming NSRP-2023.

We would like to thank Dr. Nandita Maiti and Prof. Mainak Banerjee, Guest Editors of this special issue for their efforts to bring out a scientifically rich bulletin containing nine articles of varied interests in the field of radiation and photochemistry.

Finally, we wish to express our sincere gratitude to all the life members for their constant support, encouragement and active participation in the all the scientific events organized by ISRAPS.

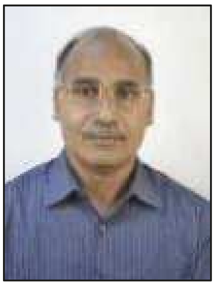

Dr. Awadhesh Kumar
President, ISRAPS

Dr. (Mrs.) J. Mohanty
Secretary, ISRAPS

INDIAN SOCIETY FOR RADIATION AND PHOTOCHEMICAL SCIENCES (ISRAPS)

EXECUTIVE COUNCIL (2021-2023)

President
Dr. Awadhesh Kumar

Vice-President
Prof. C. T. Aravindakumar
Prof. A. S. Kumbhar

Secretary
Dr. (Mrs.) J. Mohanty

Joint Secretary
Dr. P. Mathi

Treasurer
Dr. Atanu Barik

Executive Members

Dr. N. Choudhury
Dr. G. R. Dey
Prof. K. R. Genwa
Prof. S. K. Gundimeda
Dr. Virendra Kumar
Dr. M. Kumbhakar
Dr. M. C. Rath
Dr. (Mrs.) S. SenGupta
Dr. P. Sharma
Dr. V. S. Tripathi
Dr. P. D. Naik
Dr. A. C. Bhasikuttan

Co-opted Members

Prof. Santosh Chidangil
Prof. Anindya Datta
Dr. S. Dutta Choudhury
Prof. J. P. Mittal
Dr. D. B. Naik
Dr. C. N. Patra
Dr. R. Puspalata
Dr. S. K. Sarkar
Prof. K. K. Sharma
Prof. A. K. Singh
Dr. Avesh K. Tyagi
Prof. S. Wategaonkar

Web Master
Dr. Abhishek Das

Contact details:
C/o Radiation & Photochemistry Division
Bhabha Atomic Research Centre, Mumbai – 400085
E-mail: israps.secretary@gmail.com
Telephone: (022)-25593771/ 25592668/ 25590302

ISRAPS Bulletin
A Publication of
Indian Society for Radiation and Photochemical Sciences

Editor's Desk...

Radiation and photo-induced processes have attracted enormous attention across interdisciplinary research areas, viz. chemistry, biology and materials science. Indian Society for Radiation and Photochemical Sciences (ISRAPS) aims to promote research in these areas by organizing several symposia, workshops and discussion meetings. During 5th -7th Jan. 2023, ISRAPS is organizing the 15th National Symposium on Radiation and Photochemistry (NSRP-2023) at BITS Pilani, Goa Campus. It is our privilege to guest-edit a special issue of ISRAPS bulletin, Vol. 35 (1 &2), Jan. 2023 on the occasion of NSRP-2023. This issue contains nine articles in frontier research areas of radiation and photochemistry. The first article gives a brief perspective on CO_2 chemistry, discussing its origin, proliferation, chemical reactions and chemical evolution channels along different radiation tracks. The importance of vibrational sum frequency generation (VSFG) spectroscopy in probing complex biological interfaces, which provides in-depth information about the structure and dynamics at the interface is highlighted in the second article. The third article brings out the significance of matrix isolation infrared spectroscopy and electronic structure calculations for understanding the intermolecular interactions between halogenated solvents and alcohols. The photochemistry of a spin-trapping agent is explored by quantum chemistry in the fourth article. The fifth article demonstrates the use of Pd(II) complexes of *meso*-substituted porphyrins as highly efficient photocatalysts for photo-oxidation processes. The synthesis of biocompatible and water dispersible blue-emitting C-dots for the selective and sensitive detection of hyaluronic acid (HA) and hyaluronidase (HAase) is discussed in the sixth article. The application of albumin and gelatine based protein nanoparticles for drug delivery is demonstrated in the seventh article. The eighth article explores the photophysical heterogeneity in the distribution of fluorescein on interaction with unilamellar vesicles by fluorescence lifetime imaging microscopy. The last article summarizes the importance of single molecule localization microscopy for the accurate determination of position and orientation of the oscillating dipoles in protein fibril bound dye using defocused orientation and position imaging.

Finally, on behalf of ISRAPS, we sincerely thank all the contributing authors for their kind support. We also acknowledge ISRAPS for giving us the opportunity to guest-edit this special issue.

Nandita Maiti & Mainak Banerjee
(Guest Editors)

Dr. Nandita Maiti *holds a Ph.D. in Chemistry from Indian Institute of Science, Bangalore. She has received fellowship from Alexander von Humboldt Foundation, Germany for her post doctoral work. Presently, she is working as a Scientific Officer (G) at BARC and is an Associate Professor (honorary) at Homi Bhabha National Institute, Mumbai. Her research work focusses in the frontier areas of Nano-Raman Spectroscopy that involves the fabrication of novel plasmonic nanomaterials for the detection of drugs and pollutants, viz. toxic heavy metal ions, pesticides, food adulterants, etc. using colorimetry and surface-enhanced Raman scattering. She is involved in the development of simple, user-friendly and cost-effective "Milk Adulterant-Melamine Testing Kit" for melamine detection in milk samples and nanoparticle loaded polymeric films for radiosensitization applications. Apart from research, she is involved as an editorial board member of Spectrochim. Acta A.*

Dr. Mainak Banerjee *is working as a Professor in the Department of Chemistry at BITS Pilani- K. K. Birla Goa Campus. He has obtained his Ph.D. form Indian Institute of Chemical Biology in 2006. After two post-doctoral studies in Pusan National University and POSTECH, South Korea he joined BITS, Goa as Assistant Professor in 2009 and has been working there since then. He is actively working in the areas like mechanochemical synthesis, green chemistry, molecular sensor, and supramolecular chemistry. He has published more than 60 papers in reputed international journals and has two patents. He has also authored several review papers. He is an elected member of Royal Society of Chemistry (MRSC) and recipient of BK 21 fellowship of Korea Government for Postdoctoral studies.*

Contents

ISRAPS Bulletin *Vol. 35, Issue Number 1&2* *January, 2023*

A perspective on CO_2 chemistry in space

Daly Davis[a*] and Sajeev Y.[b]

[a]*Department of Polymer Science, S K Somiya College, Somaiya Vidyavihar University, Mumbai -77*
[b]*Theoretical Chemistry, Bhabha Atomic Research Centre, Mumbai -85*
**Email: daly@somaiya.edu*

Abstract

The ubiquity of carbon dioxide in the universe arouses the greatest curiosity about its origin, distribution, and astrochemistry. Spectral data from the ISM and experimental modeling of different astrophysical conditions can be used in the lab to understand the origin of CO_2 and its astrochemical channels. The rheology of CO_2 under different astrophysical environments is a key objective of various planetary missions. The origin, proliferation, chemical reactions, and chemical evolution channels of CO_2 along different radiation tracks are critical not only in astrochemistry but also in the investigation of origin of life. Low-energy electron-induced chemical reactions offer excellent means of simulating astrochemistry and prebiotic chemistry of CO_2.

1. Introduction

Carbon dioxide is ubiquitous in the Universe [1]. In our solar system CO_2 is the most abundant carbon bearing species followed by carbon monoxide and methanol [2]. It is present in comets [3] and has been identified in massive protostars [4], dense clouds and young stellar objects [5]. CO_2 is also the most abundant species in the interstellar medium (ISM) next to water [6]. Recently, James Webb telescope confirmed the presence of CO_2 in exoplanet WASP-39 b [7]. Yet its origin, proliferation, and astrochemical significance are not fully understood or investigated [2,8].

ISM is a rich reservoir of simple and complex molecules. It contains about 180 molecules in the gaseous state and about 20 molecular species in the interstellar dust, i.e., condensed phase [6]. It has been predicted and observed that CO_2 exists predominantly in the solid phase and to a lesser extent in the gaseous state [9,10]. While pure solid CO_2 exists in the amorphous phase below 30 K, above it a crystalline cubic structure is achieved due to phase-transition [2, 11]. It has been shown that crystalline CO_2 ice is produced due to the slow deposition of CO_2 in the ice grain conditions of the ISM (20–30K) [12]. Based on the existing spectral observations of CO_2 from ISM and the laboratory experiments, it is concluded that the pure CO_2 ice in space exists mostly crystalline [12].

Solid CO_2 being the major component of the icy mantle coating sub-micron-sized dust grains [13], it is very important to understand its origin, proliferation, rheology, and chemistry through ISM spectral data and laboratory experiments under ISM conditions. These data help in simulating ISM environments for several occasions such as different space programs, astronaut training, creating outer space station environments, designing space flight etc. Here, we are depicting possible CO_2 based theoretical and experimental simulations which can give better understanding about CO_2 chemistry in ISM. Furthermore, we share here a possibility to unravel space chemistry through low-energy electron-induced reaction channels involving CO_2.

2. Discussion

Rheology of outer space

The matter in ISM includes gas in ionic, atomic, and molecular form, as well as dust and cosmic rays. In the extreme conditions of ISM with temperatures ranging between 10 and 100 K, this matter exists in very low number densities varying from 10^{-4}–10^{8} cm^{-3}. Despite these extreme conditions, more than 200 simple and complex molecular species are discovered since the discovery of first polyatomic molecule 50 years ago [14]. Gas phase reactions alone are not able to explain the molecular abundances in ISM. The chemical reactions that occur on interstellar dust particles, that is to say condensed phase reactions, are crucial to explain the formation of even simple species like most abundant H_2 species. Interstellar grains provide the surface for accreted species to meet and react with each other. 90% of grain mantle is composed of water, methanol and CO_2. Understanding the rheology of CO_2 ice is thus important for understanding the grain formation and chemical evolution of ISM.

In solar system all the planets and their moons are covered with CO_2 ices [2]. Understanding the physical processes of material formation and chemical reactions on planets and satellites require detailed knowledge of rheological properties of these ice covers, especially on the polar regions of the planets and satellites. Ice rheology is controlled by a number of factors, including temperature, grain size, porosity and stress, most of which are highly influenced by impurities or crystalline form. Hence understanding the form of pure and mixtures of CO_2 ices and their rheology at different solar system conditions are very important to do simulations for different planetary mission. For example, CO_2 condensation and sublimation is a part of CO_2 cycle on mars. During this process equatorial CO_2 is getting deposited near polar region, and the latent heat released is the major energy source during these periods [15]. The knowledge on rheology of CO_2 during this CO_2 cycle helps mars mission simulations. Also, the grain size and rheology on Mars polar deposits (MPD) which includes a large percentage of CO_2 ices are important in modeling flow on Martian surface [16].

As indicated earlier, amorphous to crystalline phase change of pure CO_2 happens at 30 K, and above this temperature of ISM conditions pure CO_2 exists as crystalline form. However, even below 30 K, CO_2 can be formed in crystalline form depending upon the rate of deposition [12]. The electron induced reaction cross sections of pure crystalline and amorphous CO_2 are different [17]. This indicates the importance of data on morphology of CO_2 during ISM and solar system simulations. There is also much less experimental laboratory simulation data on CO_2 ice mixtures. Laboratory experiments, including deposition of CO_2 with other molecules such as H_2O, methanol, CO at various ISM and planetary conditions as well as rheological understanding of grain and ice formation are the requisites for space simulation data. It also enables us to understand the evolution of the pre-stellar phase in the formation of planets and comets.

Radiolysis reactions of CO_2

Abundance of CO_2 in different ISM and planetary atmosphere [1, 18] indicates that in space CO_2 can be formed by various routes either in gas phase or in solid phase or in a mixture state. Most of the work suggest an activation energy barrier mechanism which further indicates a third body or requirement of energy source in CO_2 formation either in ice or gas form [1, 19]. The laboratory astrochemical simulations experiment as well as theoretical calculations proposed different pathways using different radiational energy sources such as ultraviolet, X-rays, high energy charged particles or electrons [19]. Even if the first-time detection of ISM CO_2 has been confirmed through the laboratory simulation of radiolysis reaction of H_2O and CO [20], the exact mechanism of the oxidation of carbon monoxide and the intermediates formed in the process are still under some dispute. Experimental observations of HOCO· radical intermediate of this reaction is not theoretically supported [1]. That means, even for confirming the mechanism of the formation of CO_2 in space, laboratory and theoretical simulations are needed. We can create all the simulation atmosphere in laboratory and study the mechanism of CO_2 formation under different conditions in presence of various ices such as H_2O, CO and other C bearing molecules such as CH_3OH. Detailed theoretical calculations are also required to remove the ambiguity about the transient species.

Several other reactions can happen between the mixtures of ice layers by radiation energy. Astrochemical laboratory simulation experiments are designed to explore them. Several simulation studies are reported on H_2O and CO_2 ices. If CO_2 and H_2O are forming ice together, its lattice formation and neighboring interactions can also be different in the occluded state. Depending upon the interactions in condensed phase and radiation energy, CO_2-H_2O mixtures can produce several molecules such as HCOOH, CH_3OH, CH_3COOH etc which are already been detected in the ISM [2,21]. Secrets of chemical synthesis in ISM lays in the ambient conditions of ice mixtures such as morphology of ice mixture formation at different ISM temperatures and pressures, influence of other gases and ices etc. Experimental and theoretical Simulation studies on clathrate and occluded state formation of CO_2- H_2O ices are needed to learn unravel the ISM synthesis.

Detection of chemical species is mainly depending upon the identification of spectral lines available from several space mission spectrometers [20,22]. This identification legs on the laboratory spectra created under similar ISM conditions. Even though laboratories produced gas phase data condensed phase data, on different synthesis are very less. Several chemical reactions using CO_2 ices under different ambient and energy conditions are required to decipher the spectral lines obtaining from ISM as well as understanding the ISM chemical synthetic routes.

Electron induced chemical reactions on CO_2 ices

The role of low energy electrons (LEE) in ISM synthesis has long been studied and reviewed [23]. Studies revealed that in the “grain factories” of ISM interactions of ubiquitous secondary electrons with several existing molecules or ions can form new species [1]. In the case of CO_2, despite different radiation energies of UV light, irradiation of electron beams and X-rays in condensed H_2O:CO mixtures produce same chemical products formaldehyde (H_2CO), formic acid (HCCOH) andCH_3OH along with CO_2 [1]. These leads to the preposition that all these radiation energy mechanisms going through secondary route which involve secondary electrons with very low energy. This has been experimentally validated by electron impact studies by Schmidt et al [24]. CO_2 can be produced not only by H_2O and CO ices, but there are several ways to form CO_2 in the ISM [19, 25] such as CO and O channel. The exact mechanisms of all these channels are not known. We can use LEE channel to study these mechanisms theoretically and experimentally and it may be possible to understand the possible mechanisms of CO_2 production in the ISM. Many of the synthetic routes of CO_2 formation in the ISM are demonstrated only using theoretical models [25]. Feasibility of such reactions can be studied using laboratory simulation experiments.

As mentioned in previous section, CO_2 ices can produced complex molecules starting from formic acid (HCOOH) on the ISM dust grain surfaces. These astrochemical reactions involving CO_2 can also be simulated using LEE induced reactions in the condensed phase. For understanding such synthetic route properties of CO_2, interaction with LEE in the gaseous state as well as solid state should be explored.

Considering the possibility of studying astrochemical synthesis our groups developed a experimental set up to simulate condensed phase electron induced reactions in ISM conditions. One of the reactions we had been studied is electron attachment on CO_2 ices. CO_2 is deposited in amorphous and crystalline form under ISM conditions (18 K, 2×10^{-10} Torr) depending upon the thickness of CO_2 film. The film characterization is done by reflection absorption infrared (RAIR) spectrometry. The study shows that the O^- desorption from amorphous phase is considerably larger than crystalline phase. Also, electron energy for O^- desorption from gas phase CO_2 is different that of condensed phase O^- desorption. As mentioned earlier most of the ISM CO_2 ices exists in the solid crystalline condition. This indicates electron induced chemistry of CO_2 is different even in different phases of the CO_2 in the ISM condition. Exploring more on the aspects of atmosphere dependent phases and their electron induced reactivity will enable us to understand ISM synthesis in such poor reactivity conditions with very low temperature and pressure.

Another electron impact experiment from our group on formic acid shows the production of CO_2 and H_2 by dissociative electron attachment channel [26]. Formic acid being the first complex molecule detected in the ISM and its formation is proposed from $CO_2 + H_2$ channel. The information that very low energy electrons (6 eV) can produce CO_2 out of formic acid has a lot of impact on simulation studies on CO_2 cycle on mars and other solar plants. It also helps in other chemical synthesis simulation experiments in ISM conditions.

Prebiotic chemistry of CO_2 induced by LEE

The chemical evolution of life, i.e., the hypothesis that life could have evolved from the physico-chemical conditions of the primitive Earth, is the most widely accepted theory of the origin of life [27,28,29]. Chemical evolution began with small primary reactants produced by energy sources on the primitive Earth and continued over time both in the atmosphere (gas-phase synthesis) as well as in the geochemical environments of the hydrosphere and lithosphere (condensed-phase synthesis) to form advanced molecules. There are many possible energy sources that could have been available on the primitive Earth for prebiotic synthesis. In 1959, Miller and Urey suggested that electrical discharge could have been the most favorable energy source available for the direct synthesis of advanced prebiotic molecules on the early Earth [30]. The electric discharge phenomenon is also a copious source of low-energy electrons (LEEs). Observations have indicated that electromagnetic waves injected by electric discharges can even precipitate a significant amount of the low energy electrons out of radiation belts. The importance of LEE in the context of prebiotic synthesis comes from the fact that, upon collision with a primordial molecule, a low-energy electron (LEE) can produce chemically reactive radical anions, which in turn induce chemical reactions that could be of prebiotic importance.

Short-wave UV (<300nm), is a highly active part of solar radiation, is another energy source for LEEs. For example, Sagan [31] analyzed the flux of solar UV light that penetrated the earth's primitive reducing atmosphere. His analysis indicated that unprotected microorganisms of the type existing today would receive a mean lethal dose at 2600 angstroms within 0.3 seconds. A constant dose of intense short-wave UV radiation is a source for the abundance of low-energy electrons (LEEs)--one of the most reactive species that causes the molecular damage-- in a chemical environment. When multiple subunits of a chemical environment absorb UVB, they relax via ejecting LEEs through an efficient mechanism known as intermolecular Coulombic decay [32]. The electric discharge phenomenon and the ionizing radiations are sources for copious amount of LEEs to the atmosphere. Observations have indicated that electromagnetic waves injected by electric discharges can even precipitate a significant amount of the energetic electrons out of radiation belts [33].

Geometrically bent radical anion of CO_2, i.e., reductively activated CO_2 ($RACO_2$), is a primary reactant and is believed to be the precursor of oxygen-containing functional groups and carbon-carbon coupling products in the prebiotic synthesis of advanced molecules [34]. Reductively activated CO ($RACO_2$) is a primary reactant for the prebiotic synthesis of advanced molecules. However, the $RACO_2$ molecule in the gas phase is thermodynamically mestastable. The prebiotic synthetic pathways involving $RACO_2$ have been hypothesized to occur in the condensed phase where the $RACO_2$ exists as part of a stable chemical environment [34]. Recently, we have reported that a stable gas phase primary reactant containing the $RACO_2$ moiety is possible via the low-energy electron (LEE) capture processes [34]. The implication of a stable gas phase $RACO_2$ moiety is that it opens up a wide range of organic synthetic routes for a CO_2 rich primordial atmosphere, which otherwise had been thought to be unsuitable for producing organic molecules. To understand the basic role in the prebiotic chemistry it may be necessary to start with a closer examination of the physiochemical environment of the early Earth and the chemical reaction inherent to $RACO_2$.

3. Conclusions

Given the fact that CO_2 contributes a large amount of ISM ices and grain mantle, the rheology of CO_2 ice and its interactions under ISM conditions are important for understanding chemical synthesis in the ISM. Alternatively, ISM synthesis involving CO_2 channels can also be understood through lab experiments that accomplish chemical synthesis under ISM conditions. Efforts to generate ISM conditions in the laboratory using computational and experimental methods are therefore of great importance to mimic the ISM synthesis. State-of-the-art photochemical methods and radiation chemistry with secondary electrons play a key role in this mission.

References

1. J. H. Bredehöft (2020) *Front. Astron. Space Sci.* **7,** 33. (2020) doi: 10.3389/fspas.2020.00033
2. C. Ahrens, H.Meraviglia, C. A. Bennett, *Geosciences***12**, 51 (2022) (*references therein*)
3. W. M. Irvine, F. P. Schloerb, J. Crovisier, B. Fegley, and M. J. Mumma, *Comets: a link between interstellar and nebular chemistry. In: Protostars and Planets IV, eds V. Mannings, A. P. Boss, and S. S. Russell (Tucson, AZ: University of Arizona Press)* 1159–1200 (2000).

4. E. L. Gibb, D. C. B. Whittet, A. C. A. Boogert, and A. G. G. M Tielens. *ApJS***151**, 35 (2004)
5. P. Ehrenfreund, and S. B. Charnley, *Annu. Rev. Astron. Astrophys.* 38:427–483 (2000). doi: 10.1146/annurev.astro.38.1.427
6. A. Das, S. K. Chakrabarti, L. Majumdar, and D. Sahu, *40th COSPAR Scientific Assembly Chemical composition of interstellar dust* Abstract id. B0.5-4-14. (2014)
7. E.-M. Ahrer et al.*Nature***609**, 229-230 (2022)
8. M. Minissale1, E. Congiu, G.Manicò2, V. Pirronello, and F. Dulieu1 *A&A***559**, A49 (2013) DOI: 10.1051/0004-6361/201321453
9. E. Herbst, and C. M. Leung, C. M., MNRAS, **222**, 689 (1986)
10. E. F. van Dishoeck, et al.*A&A,***315**, L349 (1996)
11. C. De Bergh, B. Schmitt, L. V. Moroz, E. Quirico, D.P. Cruikshank, *Laboratory data on ices, refractory carbonaceous materials,and minerals relevant to transneptunian objects and Centaurs. In The Solar System Beyond Neptune; University of Arizona:Tucson, AZ, USA,* pp. 483–506. (2008)
12. R. M. Escribano, G. M. Muoz Caro, G. A. Cruz-Diaz, Y. Rodrguez-Lazcano and B. Mat, *Proc. Natl. Acad. Sci. U. S. A.***110**, 12899–12904 (2013)
13. U. Raut, D. Fulvio, M.J. Loeffler, R. A. Baragiola*Astrophys. J.***752**, 159 (2012).
14. a) L. E. Snyder, D. Buhl, B. Zuckerman and P. Palmer *Phys. Rev. Lett.***22** 679-681 (1969) b) Masatoshi Ohishi J, Phy.: Conference Series 728 (2016) 052002
15. P.B. James,H. H. Kieffer, and D. A. Paige, D. A., "The seasonal cycle of carbon dioxide on Mars.", in *Mars*, pp. 934–968 (1992)
16. C. A Barr, S. M. Milkovich*Icarus***194**, 513–518 (2008)
17. D. Davis, S. Kundu, V. S. Prabhudesaia and E. Krishnakumar*Phys. Chem. Chem. Phys.***16**, 8582-8588 (2014)
18. D. C. B. Whittet et al *The Astrophysical Journal*, **655**:332-341, (2007)
19. M. Minissale1, E. Congiu1, G.Manicò2, V. Pirronello2, and F. Dulieu *A&A***559**, A49 (2013)
20. d'Hendecourt, L. B., &Jourdain de Muizon, M. A&A, **223**, L5 (1989)
21. M. L. Delitsky and A. L. Lane *J. Geophys. Res.***103**,31391-31403 (1998).
22. E. Herbst, Annu. Rev. Phys. Chern. **46**: 27-53 (1995)
23. M. C. Boyer, N. Rivas, A. A. Tran, C. A. Verish, C. R. Arumainayagam*Surface Science* **652**, 26-32 (2016)
24. F. Schmidt, P. Swiderek, and J. H. Bredehöft*ACS Earth Space Chem.***3**, 1974–1986 (2019).
25. R. T. Garrod and T. Pauly*The Astrophysical Journal*, **735,** 15 (2011)
26. D. Davis, S. Kundu, V. S. Prabhudesai1, Y. Sajeev, and E. Krishnakumar*J. Chem. Phys.***149**, 064308 (2018)
27. A. I. Oparin, *The Origin of Life (Macmillan, New York)* (1938)
28. J. B. S. Haldane*,Rationalist Annual* **148**,3 (1928)
29. S. L. Miller and H. C Urey, *Science***130,** *245-251 (1959)*
30. C. Sagan *J. Theor. Bio.* **39**, 295-200, (1973)
31. S. Barik, S. Dutta, N.R. Behera, R. K. Kushawaha, and Y. Sajeev, Y. and G. Aravind, *Nat. Chem.***14**, 1098-1102 (2022)
32. H. D. Voss et al. *Nature*,**312**, 740-742 (1984)
33. X. V. Zhang et al. *J. Am. Chem. Soc .**126,*** 11247-11253 (2004)
34. D. Davis and Y.Sajeev Phys. Chem. Chem. Phys. **16,** 17408-17411 (2014)

About the authors

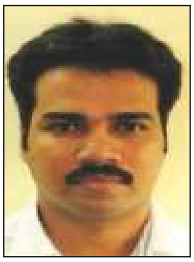

Dr. Y. Sajeev *obtained his PhD in 2005 from the Department of Theoretical Chemistry, National Chemical Laboratory, Pune. His main research interest has been the formulation and implementation of ab-initio quantum chemical methodologies for computing the autoionizing electronic resonance states. His recent research activity includes the study of low energy electron controlled chemical reactions.*

Dr. Daly Davis *is currently working as an Assistant Professor at Somaiya Vidyavihar University, Mumbai. She completed her PhD in 2005 from Cochin University of Science and Technology. Her field of research is electron transfer systems. She is currently active in electron – molecule collision experiments and electron induced chemistry with a focus on Astrochemistry and electron induced chemical reactions in biological systems.*

Vibrational Sum Frequency Generation Spectroscopy: A Tool to Probe Complex Biological Interfaces

Vineet Gunwant, Preeti Gahtori and Ravindra Pandey*
Department of Chemistry,
Indian Institute of Technology Roorkee, Roorkee 247667, Uttarakhand, India.
**Email: rpandey@cy.iitr.ac.in*

Abstract:

In this mini-review article, we discuss the potential application of vibrational sum frequency generation (VSFG) spectroscopy to probe complex biological interfaces. We will provide the basic principle of VSFG spectroscopy and explain why it can exclusively probe different interfaces by giving some specific examples of air/water interfaces, and interactions of nanoparticles (NPs) with different lipid membranes. Further, we will explain how VSFG can be used to probe the aggregation and ice nucleation properties of specific proteins. Combining the heterodyne and time-resolved measurements, the VSFG experiments can provide in-depth information about the structure and dynamics at different interfaces. Such information can be useful for various applications from fundamental understanding to translational research.

1. Behaviour of biomolecules at the interface

Biomolecules such as proteins, peptides, amino acids, polysaccharides, lipids, and nucleic acids are important natural machinery as they drive key biological processes such as sensing, drug transport, immune response etc. Most of these processes occurs at the interface of biomembranes, generally known as biological interface[1]. The interfacial water present at these biological interfaces play an important role in the hydration of the membranes, proton transfer to biomolecules etc. which ultimately makes the biological interface comprising of three components i.e. water, membranes and biomolecules[2]. It is well known that the processes taking place at interfaces are distinguished from those in the bulk, and therefore it is expected that biomolecules may show a different behaviour at the interface due to the unique hydrophobic hydrophilic environment present at the interfaces. The interfacial behaviour of such biomolecules can be further tuned to different interfacial conditions such as pH, the concentration of biomolecules, and the chemical potential of a particular interface etc. Therefore, probing the structure and dynamics of the biomolecules at the interface may provide a deeper understanding of the interfacial processes for the optimization and development of novel materials for biomedical applications[1].

Over the years, several techniques have emerged such as solid-state NMR, atomic force microscopy (AFM), surface-enhanced Raman scattering (SERS), and surface plasmon resonance (SPR) that give information about biomolecules adsorbed at interface. However, the molecular level information about the structure and dynamic of the biomolecules at the interface remains poorly understood because of the difficulties involved in probing extremely thin interfaces. Recently, the Vibrational Sum Frequency Generation (VSFG) spectroscopic technique has evolved as an efficient surface-sensitive tool to monitor the structure and dynamics of interfacial biomolecules.

2. Sum Frequency Generation (SFG) Spectroscopy

SFG is a coherent, non-linear spectroscopic method. It is highly sensitive to interfacial molecules. It is active in a non-centrosymmetric medium and possesses the characteristics of Raman-IR spectroscopy. In SFG two incident photons of frequency ω_1 and ω_2 spatially and temporally combine at interfaces and produce a photon of summed frequency ($\omega_1+\omega_2$). The interaction of the photons and material induces a polarization within a material which is equal to

$$P = \chi^{(1)}E^{(1)} + \chi^{(2)}E^{(2)} + \cdots$$

where the first term is responsible for linear absorption and the second term is for the sum frequency generation method. The intensity of the SFG signal depends on the susceptibility tensor and the electric field of the two incident beams $I_{SFG}(\omega_1+\omega_2) = |\chi^{(2)}|^2 E_1 E_2$. Here $\chi^{(2)}$is a second-order susceptibility term. In a centrosymmetric environment, all directions are equivalent and the value of $\chi_{ijk}^{(2)}$ for two opposing directions must, therefore, be identical, viz., $\chi_{ijk}^{(2)} = \chi_{-i,-j,-k}^{(2)}$. However, as $\chi_{ijk}^{(2)}$ is a third-rank tensor, a change in the sign of the three subscripts is simply equivalent to reversing the axis system, $\chi_{ijk}^{(2)} = -\chi_{-i,-j,-k}^{(2)}$.

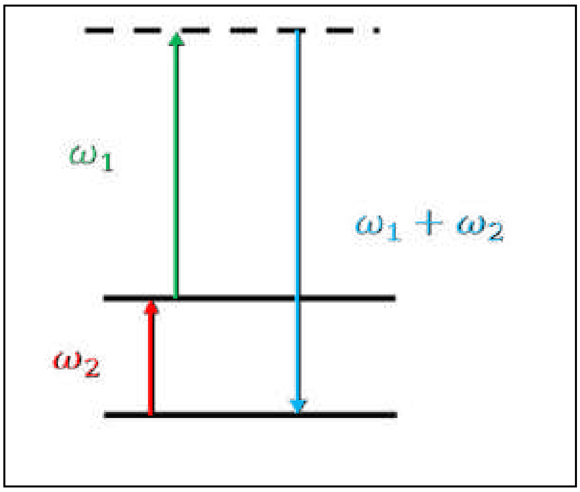

Figure 1: *Energy-level description of Sum Frequency Generation.*

In the VSFG process, two pulsed laser beams, one tunable infrared and the other visible beam are used. Here one of the incident beam photons is in resonance with vibrational transition of interest and gives characteristics of the molecule. The electronic analogue of VSFG spectroscopy known as electronic SFG has a potential to probe the electronic states present at the interfaces. The density of state information obtained from ESFG measurements can be used for optimizing the efficiency of various optoelectronic devices. We have also developed ESFG measurements in our laboratory at IIT Roorkee, but for this article we have restricted the discussion to VSFG applications. The intensity of the SFG signal at a certain frequency is dependent on the non-resonant signal and resonant signal. The measured VSFG intensity is proportional to the square of the second order nonlinear susceptibility $\chi^{(2)}$ of the sample and the intensities of the visible and infrared beams.

$$I_{SFG}\ \alpha \left|\chi^{(2)}\right|^2 I_{VIS} I_{IR} \qquad (1)$$

When the frequency of the incident infrared field is resonant with the vibrational mode n, the VSFG field can be resonantly enhanced. Thus, the susceptibility $\chi^{(2)}$ consists of non resonant (NR) and resonant (R) terms[3,4].

$$I_{SFG}\ \alpha \left| A_{NR} e^{i\phi} + \sum_{j=1}^{N} \frac{A_j}{(\omega_{IR} - \omega_j) + \Gamma_j} \right|^2 \qquad (2)$$

where A_{NR} represents the amplitude of the non resonant susceptibility, φ is its phase, A_j is the amplitude of the j^{th} vibrational mode with resonant frequency ω_j, and Γ_j is the line width of the vibrational transition.

3. Water at interfaces

Water molecules in the bulk are stabilized by a tetrahedral bonding network with their neighbours. At interfaces, this molecular arrangement is not possible, due to increased surface energy. Each interfacial water molecule tries to have more number of hydrogen bonds to minimize the excess surface free energy. This can be achieved if surface water molecules assume a hexagonal lattice-type structure, with the surface terminated by free -OH bonds, which is the characteristic of the free water-air interface[3]. The vibrational spectra of interfacial water is shown in fig. 2(a), peak at $3700cm^{-1}$ represents free -OH while peaks at $3200cm^{-1}$ and $3400cm^{-1}$ correspond to strongly and weakly hydrogen-bonded water molecules at the interface. The unique structure of interfacial water turns out to be important for understanding the surface chemistry of mineral-water interface, atmospheric aerosols, membrane biochemistry etc. Moreover, anything which passes through biological membranes has to interact with interfacial water. The water then determines the fate of any biomolecule as to how it will interact with membranes. The interfacial water molecules facilitate energy transfer between membrane leaflets of DPPC, which is the most ubiquitous phospholipid membrane. This was attributed to the emergence of extended vibrational modes in the membrane due to the hydration of lipid head groups[5]. The presence of water near the surface of biomolecules is crucial for maintaining sufficient structural flexibility so that the necessary motion of biomolecules can take place.

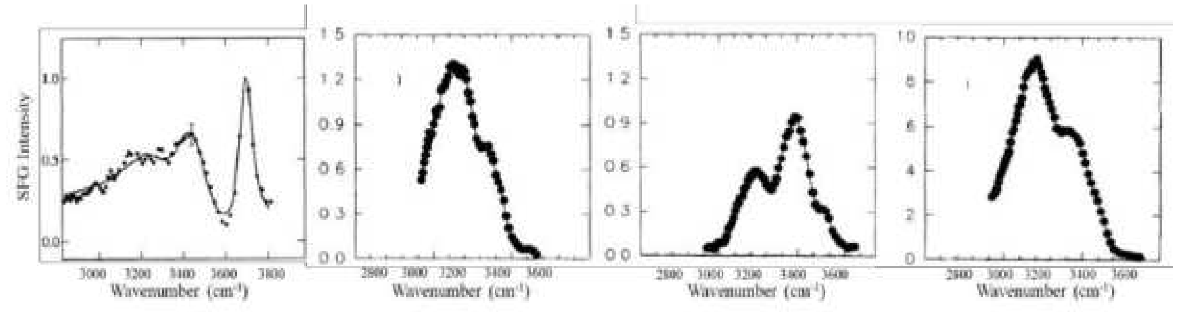

Figure 2: *Vibrational SFG spectra of water at (a) free water-air interface, showing a peak at 3700* cm^{-1} *corresponding to free –OH (b) water in contact with quartz surface at pH 1.5, free -OH signal diminished due to ionization of interface (c) water in contact with quartz at pH 5.6 and* ***(d)*** *at pH 12.3.Reproduced with permission from ref*[3,4]*. Copyright 1993 by Physical Review Letters.*

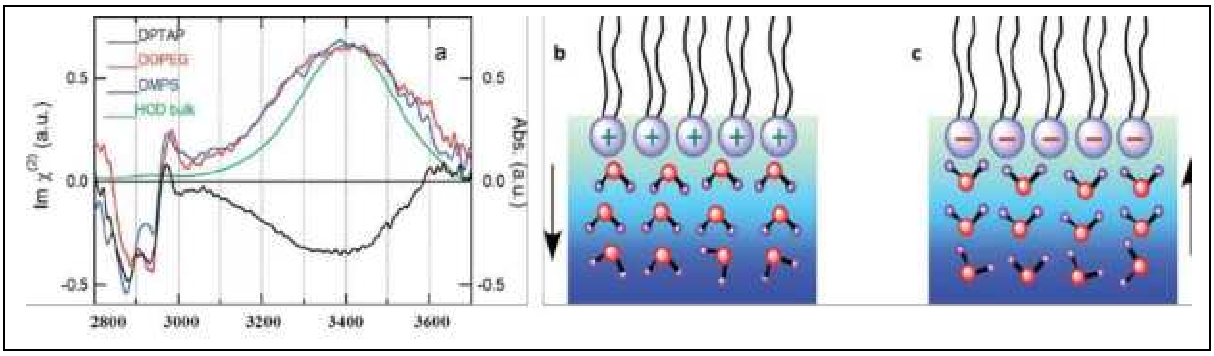

Figure. 3: *(a) HD-VSFG spectrum in the -OH stretch region of water molecules at differently charged lipid monolayers, (b) In the presence of positively charged lipid, water dipoles are oriented away from the interface while, (c) In the presence of negatively charged lipid, water dipoles are oriented towards the interface.Reproduced with permission from ref* [6]*. Copyright 2010 by American Chemical Society.*

Apart from the free water-air interface, buried water interfaces can be applied to many surface sciences such as electrochemistry, micelle formation, membrane stability etc. For the first time, Shen *et al.* presented the SFG spectra of a fused quartz/water interface under various conditions[3,4]. The results indicate that interfacial water molecules can interact with quartz by two forces: hydrogen bonding and electrostatic attraction which result from the ionization and deionization of surface silanol (SiOH) groups. At a high pH value of 12.3, the surface silanol groups are all ionized, and the negative surface charge produced by quartz aligns some water molecules towards itself giving a strong SFG signal (fig. 2d). However, if the quartz surface was neutral (pH 1.5, fig. 2b), the water molecules formed hydrogen bonds with quartz surface pointing their oxygen towards the surface. In this case, the signal intensity was low compared to high pH value therefore it was expected that only 1 or 2 monolayers of water was oriented. At intermediate pH value of 5.6, the surface was partially ionized due to which some of the water molecules are pointing towards quartz surface while some point away from it ultimately, disturbing the order of interfacial water molecules which can be corroborated to even more decrease in SFG intensity as compared to pH 1.5 and pH 12.3(fig. 2c).

The interfacial water structure can undergo an order-disorder-order pattern depending on the pH of the bulk solution. At specific pH, when the surface becomes completely ionized, more water molecules can be aligned thus giving rise to an intense SFG signal. In addition, surfactants/lipid membranes can also orient water molecules at the interface depending upon the charge of lipid membrane. Tahara *et al.* have demonstrated that water is oriented differently at different charged lipid membranes using heterodyne-detected vibrational sum frequency generation (HD-VSFG) spectroscopy[6]. The beauty of HD-VSFG measurements is that they can provide information about $\chi^{(2)}$ which is lost in simple VSFG measurements as it measures $|\chi^{(2)}|^2$. The direct measurement of $\chi^{(2)}$ allows for retrieval of the phase information in the HD-VSFG measurements. For the negatively charged lipid DOPG and DMPS, the Im $\chi^{(2)}$ spectrum has positive sign (fig. 3) which represent that the water dipole is oriented towards the interface (H-up orientation) while for positively charged lipid DPTAP, the Im $\chi^{(2)}$ spectrum shows negative sign which represent that the water dipole is oriented away from the interface (H-down orientation). So, the net charge on lipid head groups governs the net orientation of water molecules at the interface.

4. Interfacial water mediates the interaction between Gold Nanoparticles and bio membranes

The surface charge of gold nanoparticles (GNPs) influences their interaction with the biological membranes. It is reported that anionic and cationic GNPs follow different cell internalization pathways, which predominantly rely on the surface charge of GNPs. The interactions of NPs with cell membrane are governed by the nature of the molecules, surface characteristics, and solution (Water) environment. Having considerable attention aimed at NPs membrane interaction it becomes important to know the role of interfacial water. Gahtori *et al.* used Vibrational Sum Frequency Generation (VSFG) spectroscopy to show the effect of NPs charge to perturb the interfacial potential and stern layer configuration at lipid-water interface[7]. Cationic and anionic GNPs were prepared and their interaction with model lipid membranes (1,2-dipalmitoyl-sn-glycero-3-phosphoglycerol (DPPG, negative charged), 1,2-dipalmitoyl-3-trimethyl ammonium-propane (DPTAP, positively charged), and 1,2-dipalmitoyl-sn-glycero-3-phosphocholine (DPPC, zwitterionic) was monitored. It was found that cationic GNPs induced a significant change in the water spectra when interacted with negatively charged DPPG lipid (fig. 4a), while anionic GNPs do not bring any noticeable change in the water spectra.

For DPTAP being a positively charged lipid monolayer, there were counter intuitive trends in the water spectra. Both cationic and anionic GNPs show depreciation in water intensity, moreover cationic GNPs show more depreciation compared to anionic GNPs (fig. 4b). The results were explained on the basis of stern layer configuration. The stern layer formed at DPTAP monolayer consists of charged-lipid-surface/water/Cl$^-$ ions transform to charged-lipid-surface/water/Cl$^-$ ions/water/cationic GNPs

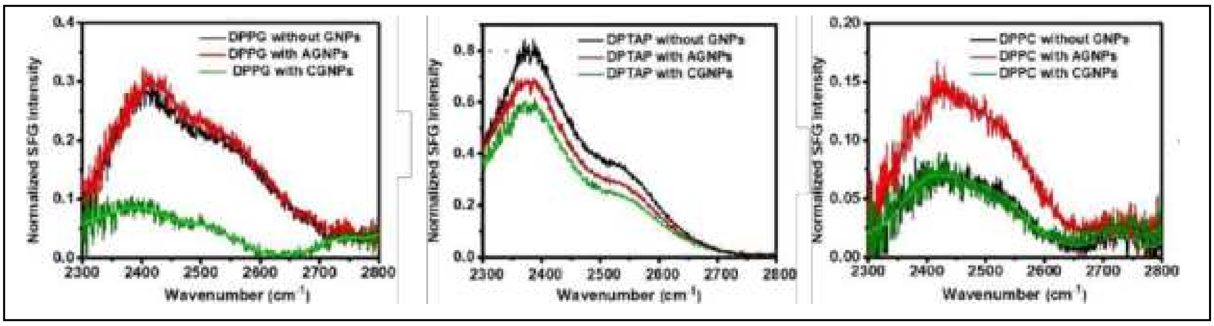

Figure 4: *Interfacial water SFG spectra when cationic and anionic GNPs are added in presence of (a) negatively charged DPPG monolayer (b) positively charged DPTAP monolayer and (c) zwitterionic DPPC monolayer. Reproduced with permission from ref*[7]. *Copyright 2021 by American Chemical Society.*

in presence of cationic GNPs which results in the cancellation of the net dipole of water molecules near DPTAP monolayer and SFG intensity of water stretch vibrations decreases. In the presence of anionic GNPs, Cl^- ions of lipid membranes be likely pushed toward the lipid head groups because of repulsion between Cl^- ions and anionic GNPs thus making the interface positively charged DPTAP monolayer/Cl^- ions/water/anionic GNPs. This configuration also results in the decrement of SFG intensity. In the case of zwitterionic lipid monolayer, DPPC, it was observed that anionic GNPs enhance the water SFG intensity (fig. 4c). DPPC composed of both positive and negative charged head groups with the positive group facing towards the water surface. When anionic GNPs were added to the monolayer, they attracted toward the positive head group thereby neutralizing the effect of positive charge, in this way only the negative charge of the lipid remains at the interface. The effect of neutralization of charge by anionic GNPs increases the interfacial water alignment which results in an increment of SFG intensity. Whereas in the presence of a cationic GNPs, there are only subtle changes in the dipolar orientation profile which results almost no change in the VSFG spectrum. This study reveals, how interfacial water mediates the interaction between GNPs with different lipid membranes.

5. Hydration and lipid-mediated lysozyme oligomerization at the model cell membrane

Protein aggregation is a cause of many neurodegenerative disorders such as Alzheimer, Parkinson diseases. In presence of cell membranes, the aggregation is extensively enhanced due to protein misfolding in the cellular environment. To understand the molecular-level insights of protein aggregation induced by membranes, it is essential to study the role played by lipid chains, interfacial water molecules and protein hydration near the lipid/water interface. Four major factors are relevant to understand protein aggregation near the lipid membrane. These are (a) conformational change in protein while in contact with lipids, (b) accumulation of protein at the interface, (c) change in the orientation of

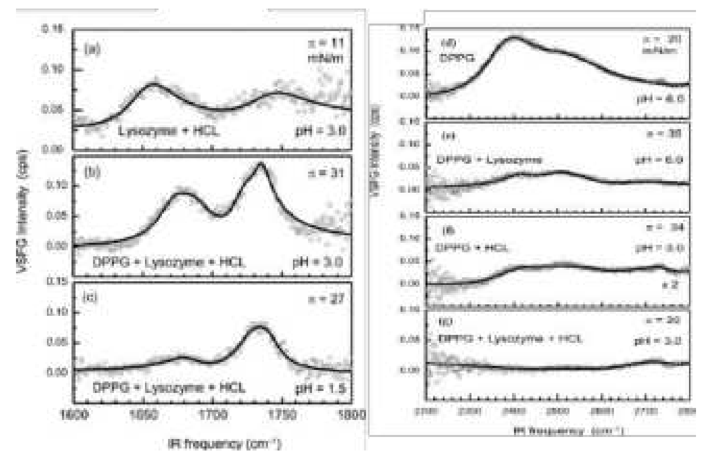

Figure 5: *VSFG spectra in the C=O region for (a) lysozyme monolayer at pH3 (b)DPPG in presence of lysozyme at pH 3, peak at 1685 cm^{-1} was attributed due to the formation of small aggregates of lysozyme(c) DPPG in presence of lysozyme at pH 1.5,the decrease in intensity of aggregates was due to the departure of lipid-lysozyme aggregates domains from the interface.(d-g) VSFG spectra in the O-D stretching region, as lysozyme was added to the DPPG monolayer interface, the water intensity decreased, which indicated significant dehydration of lipids. Reproduced with permission from ref*[2]*. Copyright 2014 by American Chemical Society.*

protein upon interaction with lipids, and (d) templating effects of the membrane. Rzeznicka *et al.* studied an aggregation of lysozyme oligomers at a negatively charged DPPG lipid monolayer while varying the pH[2]. At low pH conditions, basic amino acids of the protein backbone get protonated which may increase the side chain charge repulsions thus exposing the hydrophobic and aggregation-prone sites to the water. This facilitates the protein-protein interaction which ultimately leads to aggregation.

It was found that, at the air/water interface, lysozyme maintains its native structure even at pH 1.5 because in an acidic environment most of the amino acids are protonated which induces repulsion between side chains of lysozyme and consequently prevents aggregation. However, in presence of lipids at the air/water interface the aggregation of lysozyme starts as the solution pH is reduced (fig.5a-c). The process of aggregation was mainly derived from the dehydration of lipids and an increase in lipid order. The DPPG lipid, being negatively charged, attracts protonated, positively charged side chains of lysozyme towards itself, which can be observed by the interfacial water SFG spectra (fig. 5d-g) that decreases when lysozyme is added at the DPPG-lipid/water interface. The extra added lysozyme molecules adsorb at the peripheral sites of the DPPG monolayer which ultimately results in the dehydration of lipids and an increase in the lipid order. The increase in lipid order decreases the area occupied by each lipid molecule which in turn reduces the distance between lysozyme oligomers adsorbed at the peripheral sites of DPPG. In this way, lysozyme molecules act as coupling units which favor aggregation.

6. Ordered water structure facilitates ice nucleation

The ice nucleation process starts when small ice

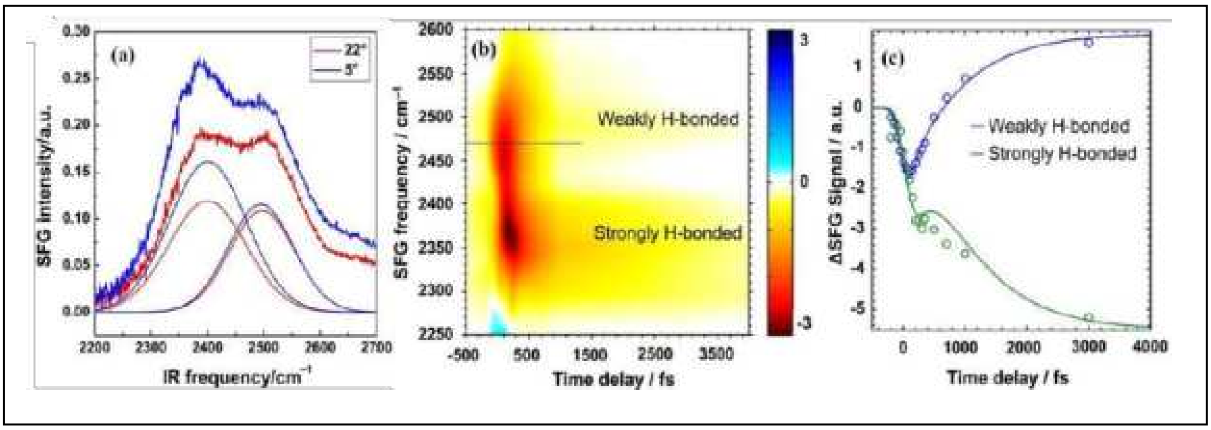

Figure 6: *(a)VSFG spectra of water near P. syringae bacteria surface, as the temperature was reduced to 5°C the strongly hydrogen bonded population of water molecules increases(b) time-resolved SFG spectrum of the bacteria-water interface after excitation with a 2470cm^{-1} pulse, the signal bleach is very intense in the low-frequency region that corresponds to strongly hydrogen-bonded water molecules(c)time-resolved bleach for strongly and weakly hydrogen-bonded water molecules. Reproduced with permission from ref[5]. Copyright 2016 by American Association for the Advancement of Science.*

crystal embryos form on the protein surface. The ice crystals are formed which further facilitated by the ordered water arrangement at the protein surface. Protein "inaZ" is a membrane protein, present at the outer cell membrane of *P. syringae* bacteria which is known to form ice crystals close to the melting point of ice. The bacteria are used for artificial snow production in winter sports around the world. For farmers, ice nucleation can be devastating as it can damage the crops. To test the model, of forming ice crystals near the protein surface, experimentally, Pandey *et. al* studied the interfacial water arrangement around the ice-nucleating protein inaZ using SFG spectroscopy[5]. It was found that the two conditions favor ice nucleation: (a) arrangement of water in an ordered structure, (b) removal of latent heat due to phase transition. To test the first condition, SFG spectra were taken in the O-D range. Fig.6a shows the temperature dependence of interfacial water in the presence of inaZ protein. When the temperature was lowered from 22^{o}C to 5^{o}C, the strongly hydrogen-bonded population of water molecules at 2390cm^{-1} increased, whereas the weakly hydrogen-bonded population at 2500cm^{-1} remained unchanged. Also, using MD simulations it was found that, at lower temperatures the water is ordered which is mainly driven by hydrophilic end groups of the protein whereas inner (hydrophobic) regions of the protein did not show a pronounced effect. So, the commonly assumed fact that the presence of only hydrophilic sites promote ice nucleation was not sufficient to explain the ice nucleating properties of *P. syringae* bacteria, but a pattern of hydrophobic-hydrophilic regions can induce optimum water alignment and thus ice nucleation. Near hydrophilic regions, the water molecules are strongly aligned and therefore their mutual dipole-dipole interaction is increased. The strong hydrogen bonding network promotes energetic coupling between the dipoles which results in effectively removing heat away from that region ultimately promoting ice nucleation. The long-range coupling of water dipoles has a direct impact on the removal of latent heat which is the second requirement of ice nucleation. Using time-resolved IR pump/SFG probe spectroscopy, the group has explored the possibility of ice nucleation by estimating vibrational energy transfer dynamics of interfacial O-D groups (fig. 6b-c). At 5^{o}C, the energy transfer from weakly hydrogen-bonded to strongly hydrogen-bonded water molecules were more efficient in the case of *P. syringae* sample compared to the ice-inactive lysozyme water interface which was used in control experiments. Therefore, the study reveals that the mechanism involved in the ice nucleation of *P. syringae* bacteria is optimized for temperatures close to the freezing point of ice.

7. Conclusion

This review has highlighted the potential of SFG spectroscopy to elucidate the orientation and conformation of biomolecules such as protein/peptides and lipid membranes at the interface. Depending upon the different surface environment like the presence of charge and pH at the interface, there is an average preferential orientation of water molecules which govern the organization of biomolecules. The ideas, concepts, and knowledge learned from these bio interfaces at such molecular level can be useful for understanding of complex biomolecular system.

References

1. Hosseinpour, S.; Roeters, S. J.; Bonn, M.; Peukert, W.; Woutersen, S.; Weidner, T. Structure and Dynamics of Interfacial Peptides and Proteins from Vibrational Sum-Frequency Generation Spectroscopy. *Chem. Rev.***2020**, *120* (7), 3420–3465.
2. Rzeźnicka, I. I.; Pandey, R.; Schleeger, M.; Bonn, M.; Weidner, T. Formation of Lysozyme Oligomers at Model Cell Membranes Monitored with Sum Frequency Generation Spectroscopy. *Langmuir***2014**, *30* (26), 7736–7744.
3. Du, Q.; Superfine, R.; Freysz, E.; Shen, Y. R. Vibrational Spectroscopy of Water at the Vapor/Water Interface. *Phys. Rev. Lett.***1993**, *70* (15), 2313–2316.
4. Du, Q.; Freysz, E.; Shen, Y. R. Vibrational Spectra of Water Molecules at Quartz/Water Interfaces. *Phys. Rev. Lett.***1994**, *72* (2), 238–241.
5. Pandey, R.; Usui, K.; Livingstone, R. A.; Fischer, S. A.; Pfaendtner, J.; Backus, E. H. G.; Nagata, Y.; Fröhlich-Nowoisky, J.; Schmüser, L.; Mauri, S.; Scheel, J. F.; Knopf, D. A.; Pöschl, U.; Bonn, M.; Weidner, T. Ice-Nucleating Bacteria Control the Order and Dynamics of Interfacial Water. *Sci. Adv.***2016**, *2* (4).
6. Mondal, J. A.; Nihonyanagi, S.; Yamaguchi, S.; Tahara, T. Structure and Orientation of Water at Charged Lipid Monolayer/Water Interfaces Probed by Heterodyne-Detected Vibrational Sum Frequency Generation Spectroscopy. *J. Am. Chem. Soc.***2010**, *132* (31), 10656–10657.
7. Gahtori, P.; Varanasi, S. R.; Pandey, R. Spectral Response of Interfacial Water at Different Lipid Monolayer Interfaces upon Interaction with Charged Gold Nanoparticles. *J. Phys. Chem. C***2021**, *125* (38), 21234–21245.

About the authors

Mr. Vineet Gunwant *joined the Department of Chemistry, IIT Roorkee as a PhD. scholar under the guidance of Prof. Ravindra Pandey in the year 2020. He did his Bachelor's and Master's degrees in Physical Chemistry from Kumaun University Nainital.Currently his PhD. work is focused on probing structure and dynamics of complex protein at air/water interface with the help of vibrational sum frequency generation spectroscopy.*

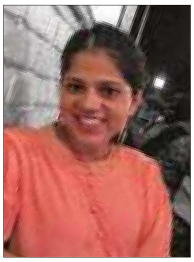

Ms. Preeti Gahtori *is currently working as a Ph.D. scholar in the Department of Chemistry, IIT Roorkee under the supervision of Prof. Ravindra Pandey. She did her Bachelor's and Master's degrees in Chemistry from Delhi University. Her work is primarily related to the investigation of the interaction between the nanoparticles with the cell membranes with the help of vibrational sum frequency generation spectroscopy.*

Prof. Ravindra Pandey *is currently working as an Assistant Professor in the Department of Chemistry at IIT Roorkee. He received his PhD in Physical Chemistry from Indian Institute of Science, Bangalore in 2012 under the guidance of Prof. Puspendu K. Das. His PhD work was focused on probing the equilibrium geometry of weakly interacting systems in solution by hyper-Rayleigh scattering. From July 2012 to September 2014, he has worked with Prof. Mischa Bonn at the Max Planck Institute for Polymer Research, Mainz, Germany as a postdoctoral fellow. He probed the role of ice nucleating proteins in controlling the order and dynamics of interfacial water molecules. From October 2014 to April 2017, he has worked with Prof. Sean T. Roberts at the University of Texas at Austin, USA, where he demonstrated that electronic sum frequency generation can be used to noninvasively probe the interfacial electronic structure of organic semiconductor films. Ravindra has joined IACS Kolkata in April 2017 and then moved to IIT Roorkee in April 2018. The primary goal of his research is to use the tools of ultrafast nonlinear spectroscopy to provide a comprehensive picture of the interfacial structure and dynamics at the complex interfaces. He has been awarded the Ramanujan Fellowship in 2017 by the Department of Science and Technology and ASEM-DUO award in 2019.*

Intermolecular interactions in solvent mixtures: Matrix-isolation IR study of CCl_4/$CHCl_3$-Alcohol mixtures

Dhritabrata Pal, Sumit Kumar Agrawal, Amrita Chakraborty and Shamik Chakraborty*
Department of Chemistry, Birla Institute of Technology and Science, Pilani, Pilani campus, Vidya Vihar, Rajasthan 333-031, INDIA
**Email: shamik@pilani.bits-pilani.ac.in*

Abstract

Molecular level understanding of the non-covalent interactions in solvent mixtures are important as they are used in different areas of chemistry and chemical processes. Herein, specific interaction between 1:1 complex of halogenated solvents (CCl_4 and $CHCl_3$) with alcohols (CH_3OH and C_2H_5OH) have been studied using matrix isolation infrared spectroscopy and electronic structure calculations. The specific interaction between [CCl_4–CH_3OH/C_2H_5OH] can be twofold: halogen bond (C-Cl···O) and hydrogen bond (O-H···Cl), while for [$CHCl_3$–CH_3OH/C_2H_5OH], the interaction can be threefold: hydrogen bond (C-H···O), hydrogen bond (O-H···Cl), and halogen bond (C-Cl···O). It has been concluded from the experimental and theoretical spectra that 1:1 mixture of [CCl_4–CH_3OH/C_2H_5OH] is stabilised by only halogen bond interaction while [$CHCl_3$–CH_3OH/C_2H_5OH] is stabilised by both hydrogen and halogen bond interaction. Favourable formation of the complexes has been explained using natural bond orbital analysis and energy decomposition analysis.

1. Introduction

Molecular level investigation of weakly bound clusters is important to understand the solute-solvent and solvent-solvent interactions, thermodynamic properties of liquid mixtures, onset of aerosol formation, and validation of theory[1]. The general understanding of weak non-covalent interactions in solvent mixtures is revolved based on hydrogen bond (H-Bond) interaction[2,3]. Halogen bond (X-Bond) interaction has emerged as another important weak non-covalent interaction[4,5]. The propensity of the formation of H-Bond and X-Bond interaction in a solvent pair with H-Bond and X-Bond donor-acceptors, is a subject of great importance. Molecular level information of the nature of non-covalent interaction is essential to predict the structure, function, and reactivity of chemical systems with the options of forming both H-Bond and X-Bond interactions. Herein, the competition between the H-Bond and X-Bond interaction has been investigated in mixtures of polar protic solvents (CH_3OH and C_2H_5OH) and non-polar or hydrophobic polar solvents (CCl_4 and $CHCl_3$).

Mixtures of alcohols with non-polar solvents are an important class of non-aqueous mixtures that have been investigated widely to estimate the thermodynamic and spectroscopic properties[6-9]. The reaction pathway, kinetics, and energetics of a chemical reaction is often modulated by the physical properties of a solvent mixture. The mixture of polar and non-polar solventsare important because mixtures of alcohols with CCl_4 and $CHCl_3$ exhibit a large a deviation from the Raoult's law. The deviation from the Raoult's law has been explained using the concept of heterogeneity at the molecular level and self-association. Hence, the investigation of the 1:1 clusters of alcohols with non-polar or hydrophobic polar solvents would provide valuable information about the non-covalent interactions at the molecular level.The propensity for the H-Bond and X-Bond interaction is going to define solvent interaction at the molecular level. Recently, attenuated total reflection-Fourier transform infrared spectroscopy of tert-butyl alcohol and its binary solutions with CCl_4 and $CHCl_3$ have been investigated[10]. It has been concluded that in both the solvents, the O−H stretching frequency is red-shifted compared to the free O−H band. Hence, $CCl_4$and $CHCl_3$ are not inert as it is considered and has some effect on the O−H stretching frequency of tert-butyl alcohol. The main aim of the current article is to discuss the specific interaction at the molecular level between alcohols (CH_3OH and C_2H_5OH) and halogenated solvents (CCl_4 and $CHCl_3$). The 1:1 complexes have been formed under matrix isolation conditions and studied using Fourier Transform Infrared spectroscopy. Experimental observations are supported by electronic structure calculations.

2. Experimental and Theoretical methods

All the experiments have been performed using Matrix Isolation Fourier Transformed Infrared spectroscopy set-up. CCl_4−CH_3OH, CCl_4−C_2H_5OH, $CHCl_3$−CH_3OH, and $CHCl_3$−C_2H_5OH mixtures were premixed with Ar and N_2 in 1:1:5000 ratio. Each mixture was deposited at 8 K on KBr window for 60 mins. The initially deposited matrix is annealed to 35 K (Ar) and 30 K (N_2) for 60 min. to form the 1:1 complexes. Afterwards the matrix is cooled to 8 K to record the IR spectrum. All the calculations were performed using Turbomole v7.3 at the MP2/aug-cc-pVDZ level[11]. The stabilisation energy (D_0) has been calculated with zero point vibrational energy and basis set superposition error correction. Electrostatic surface potential (ESP) of the monomers have been calculated using Multiwfn program package[12]. Nature and origin of the non-covalent interaction in the complexes have been investigated using Natural Bond Orbital analysis (NBO 6.0[13]) and Energy Decomposition Analysis (PSI4 [14]).

3. Results and discussion

The plausible electrophilic and nucleophilic centres on the monomers have been estimated using ESP plots (Figure 1). The $CCl_4$is characterised with a positive potential (~18 kcal/mol) on the top most part of the Cl atoms along the C−Cl bond along with a negative potential of ~3.5 kcal/mol on the lateral sides of Cl atoms. The $CHCl_3$ has a positive potential of ~35 and ~14 kcal/mol on the H atom and on top of the Cl atoms, respectively. A negative potential of ~7 kcal/mol is observed on the lateral sides of Cl atoms. The ESP of CH_3OH and C_2H_5OH are similar. A positive potential of ~40 kcal/mol is observed on the H atom of O-H group while a negative potential (~33 kcal/mol) is observed over the O atom. Possible binding modes between the molecules is predicted from the ESP plots. In case of CCl_4, possible interactions are C-Cl···O X-bond and

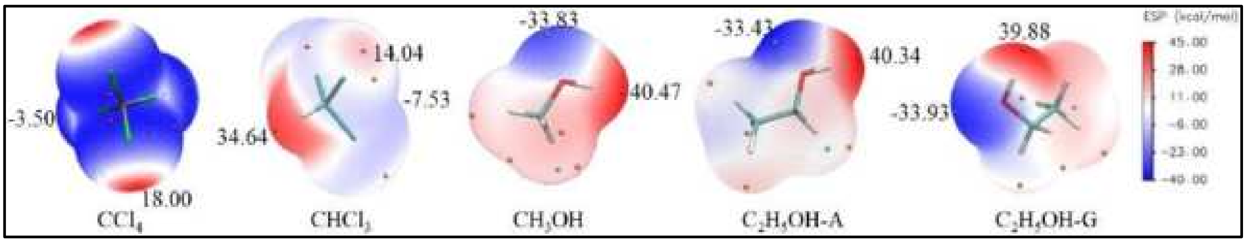

Figure 1: *Electrostatic Surface Potential (ESP) plot for all the molecules obtained at the MP2/aug-cc-pVDZ. All the values are in kcal/mol.*

O-H···Cl H-bond whereas for $CHCl_3$ the possible interactions are C-H···O and O-H···Cl H-bond, and C-Cl···O X-bond.

The experimental IR spectra of CCl_4, CH_3OH, and [CCl_4−CH_3OH] mixture are presented in Figure 2. The asymmetric stretching of C-Cl (ν_3) and combination band of (ν_1 + ν_4) are observed at 789 cm^{-1} and 767 cm^{-1}, respectively[15]. Presence of multiple IR peaks are due to the isotope effect.The C-O (ν_{CO}) and the O-H (ν_{OH}) stretching vibrations of CH_3OH are observed at 1034 cm^{-1} and 3664 cm^{-1}, respectively.Annealing of the [CH_3OH−CCl_4] mixture results in new peaks those are absent in the IR spectraof the monomers. In the ν_3 region, a new peak is observed at 800 cm^{-1}that is blue-shifted by 13 cm^{-1} from the monomer ν_3 peak. A new peak is observed at 1029 cm^{-1} corresponding to the ν_{CO} mode and matches with the position of the ν_{CO} mode of $(CH_3OH)_2$. The relative intensity of this peak in [CCl_4−CH_3OH] mixture is much higher compared to the intensity observed in CH_3OH alone. The 1029 cm^{-1} peak is red-shifted by 5 cm^{-1} compared to the ν_{CO} of the monomer. A new peak is observed at 3657 cm^{-1}which is present in the IR spectrum of [CCl_4−CH_3OH] mixture at 8 K just after deposition and gains intensity after annealing the matrix.This peak is red-shifted by 7 cm^{-1} from the monomer ν_{OH}. All the new peaks observed in the IR spectra of the mixture are assigned to the formation of the 1:1 complex of [CCl_4−CH_3OH].

Three minima have been obtained on the dimer potential energy surface (Figure 2, ii). The most stable structure corresponds to the X-Bond

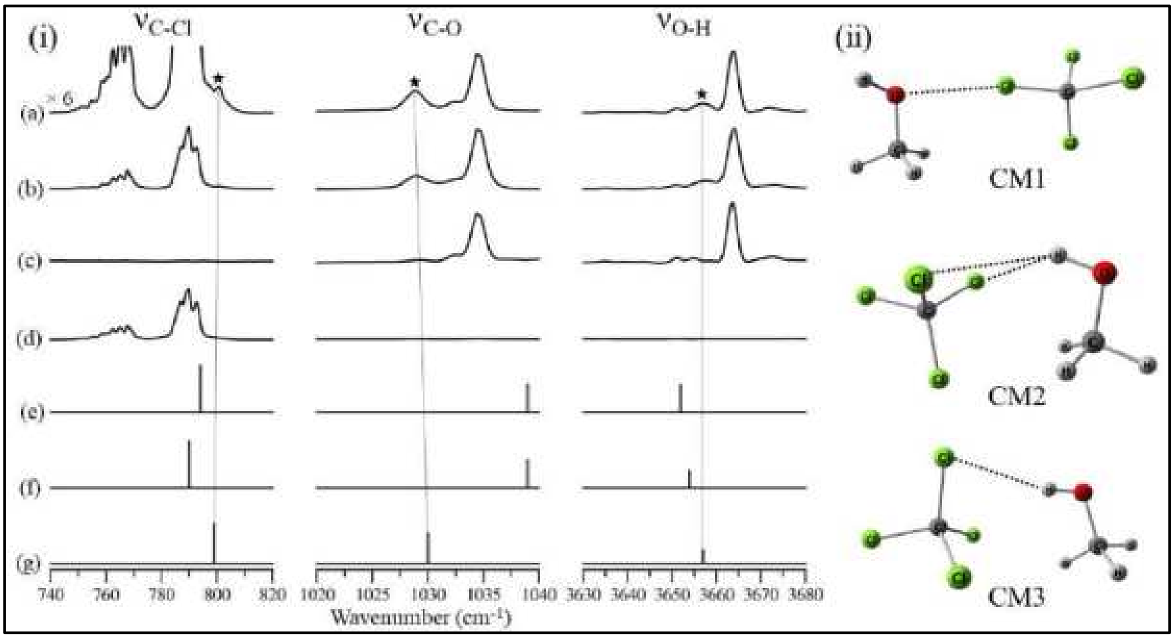

Figure 2: *(i) Comparison of the matrix-isolation IR spectra in the N_2 matrix and simulated IR stick spectra of thecomplexes obtained at the MP2/aug-cc-pVDZ level of calculation in the ν_3, ν_{CO}, and ν_{OH} regions. All the IR spectra are recorded at 8 K. Matrix-isolation IR spectra of [CCl_4−CH_3OH] mixture after annealing at 30 K (a), [CCl_4−CH_3OH] mixture after deposition at 8 K (b), CH_3OH after annealing at 30 K (c), CCl_4 after annealing at 30 K (d), simulated IR stick spectra of the complex CM3 (e), CM2 (f), and CM1 (g). (ii) Optimised geometry of the three conformers at the MP2/aug-cc-pVDZ level.*

isomer (CM1) stabilised by C-Cl···O interaction with stabilisation energy (D_0) of 2.30 kcal/mol. The next stable minimum (CM2) is stabilised by bifurcated H-bond of O-H···Cl type (D_0= 2.00 kcal/mol). The least stable minimum (CM3) with D_0 of 1.70 kcal/mol is stabilised by single O-H···Cl H-bond. Simulated frequency of CM1 predicts a blue-shift of 12 cm^{-1} in the ν_3 mode and a red-shift of 3 and 9 cm^{-1} in the ν_{CO} and ν_{OH} modes, respectively. A blue-shift of 3 and 6 cm^{-1}is simulated in the ν_3 and ν_{CO} modes, respectively, along with a red-shift of 12 cm^{-1} in the ν_{OH} mode of CM2. A blue-shift of 7 and 5 cm^{-1} is predicted for the CM3 isomer in the ν_3 and ν_{CO} modes, respectively, while the ν_{OH} mode is red-shifted by 14 cm^{-1}. The experimental IR spectra is compared with the simulated spectra and is concluded that the 1:1 complex of [CCl_4−CH_3OH] is formed by C-Cl···O X-Bond interaction in N_2 matrix.

The experimental IR spectra of CCl_4, C_2H_5OH, and [CCl_4−C_2H_5OH] mixture are presented in Figure 3. The CCl_4 spectra shows peaks corresponding to the ν_3 and $\nu_1 + \nu_4$ modes as described previously. The C_2H_5OH exists in anti and gauche conformers in the gas phase[16]. The C-O stretching mode (ν_{CO}) of C_2H_5OH is observed at 1092 cm^{-1} corresponds to the anticonformer of C_2H_5OH. New peaks are observed after annealing the [CCl_4−C_2H_5OH] mixture matrix, those are absent in the monomer spectra.In the ν_3 region, a new peak is observed at 803 cm^{-1} which is 15 cm^{-1} blue-

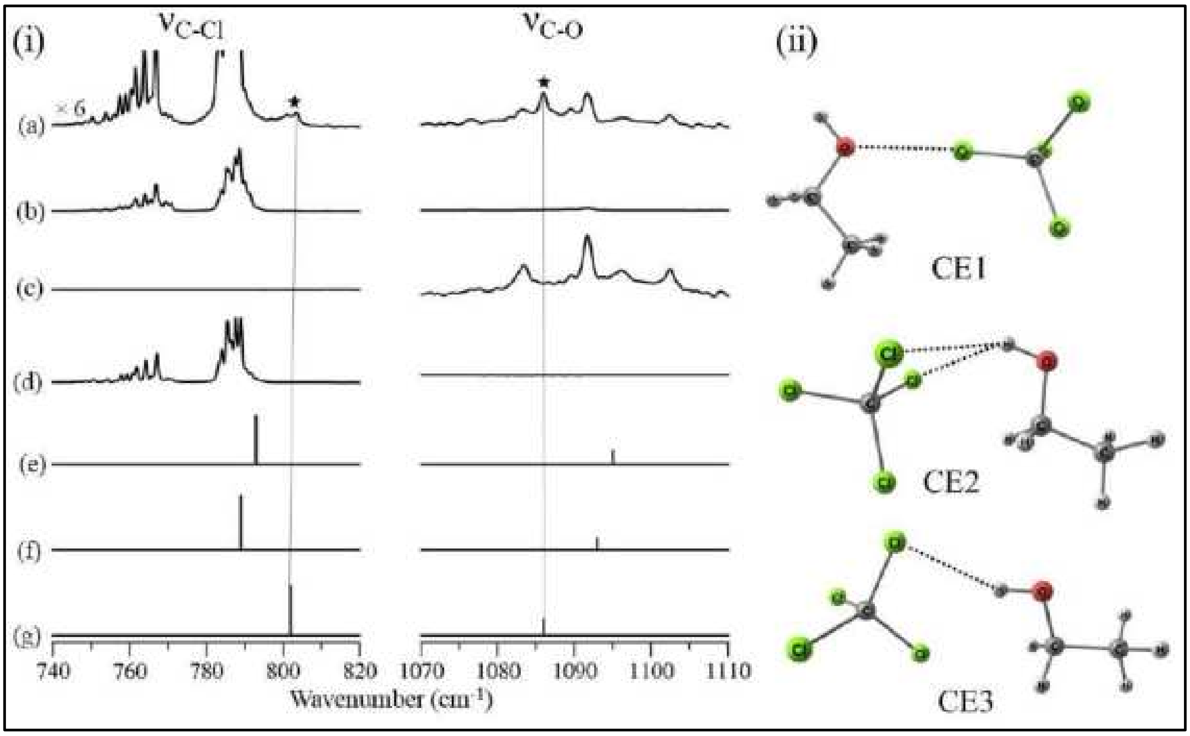

Figure 3: *(i) Comparison of the matrix-isolation IR spectra in the Ar matrix and simulated IR stick spectra of the complexes obtained at the MP2/aug-cc-pVDZ level of calculation in the* ν_3 *and*ν_{CO} *regions. All the IR spectra are recorded at 8 K. Matrix-isolation IR spectra of [*CCl_4*−*C_2H_5OH*] mixture after annealing at 35 K (a), [*CCl_4*−*C_2H_5OH*] mixture after deposition at 8 K (b),* C_2H_5OH *after annealing at 35 K (c),* CCl_4 *after annealing at 35 K (d), simulated IR stick spectra of the complex CE3 (e), CE2 (f), and CE1 (g). (ii) Optimised geometry of the three conformers at the MP2/aug-cc-pVDZ level.*

shifted compared to the monomer ν_3 peak. A new peak is observed at the 1086 cm^{-1} corresponding to the ν_{CO} of the complex.This peak is 6 cm^{-1} red-shifted compared to the ν_{CO} of the monomer. All the new peaks are assigned to the 1:1 [CCl_4−C_2H_5OH] complex.

Three minima have been obtained on the dimer potential energy surface (Figure 3, ii) corresponding to the anticonformer of C_2H_5OH. Similar complex structures are also obtained for the gauche conformer of C_2H_5OH. Herein, the discussion is based on structures for the anticonformer of C_2H_5OH. The most stable structure corresponds to the X-Bond isomer (CE1) stabilised by C-Cl···O interaction with D_0 of 2.36 kcal/mol. The next stable minimum (CE2) is stabilised by bifurcated H-bond of O-H···Cl type (D_0= 1.88 kcal/mol).The least stable minimum (CE3) with D_0 of 1.58 kcal/mol is stabilised by single O-H···Cl H-bond. A blue-shift of 15 cm^{-1} is simulated in the ν_3 mode and a red-shift of 4 cm^{-1} in the ν_{CO} mode of CE1. A blue-shift of 2 and 3 cm^{-1}is predicted for CE2 in theν_3 and ν_{CO} modes, respectively. A blue-shift of 6 and 5 cm^{-1} is predicted for the CE3 isomer in the ν_3 and ν_{CO} modes, respectively. Formation of 1:1 complex of [CCl_4−C_2H_5OH] by C-Cl···O X-Bond interaction is concluded in Ar matrix (Figure 3).

The experimental IR spectra of $CHCl_3$, CH_3OH, and [$CHCl_3$−CH_3OH] mixture are presented in Figure 4. The C−H stretching (ν_{CH}) of $CHCl_3$ is observed at 3066 cm^{-1}.The

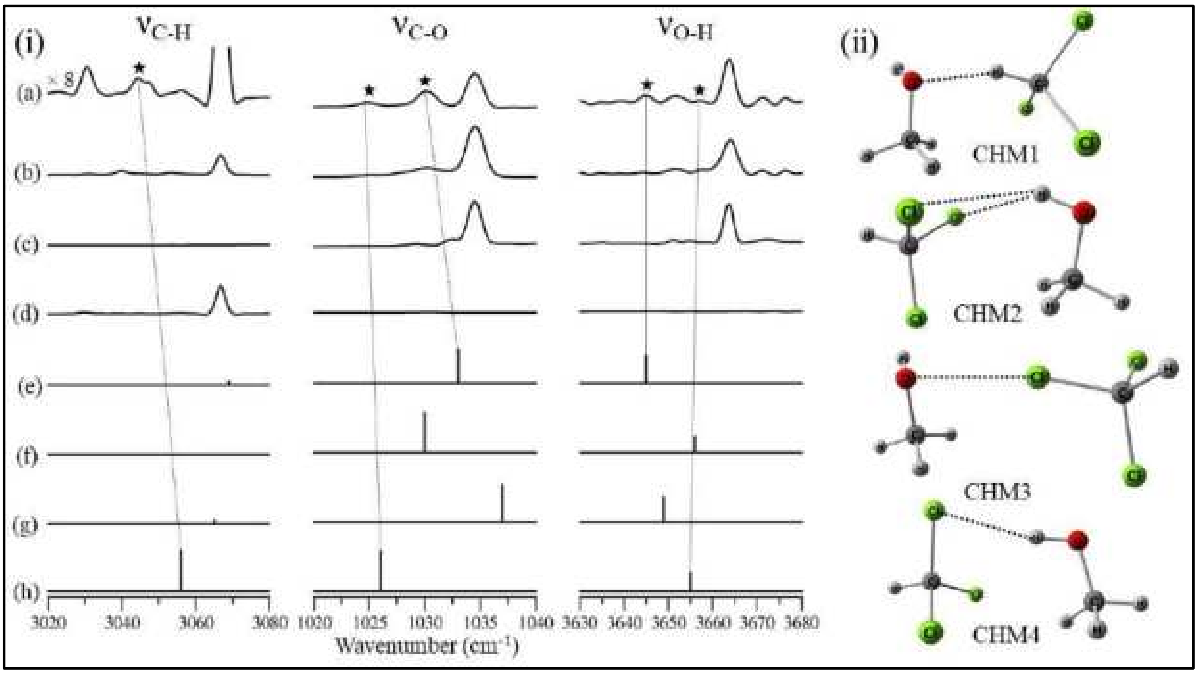

Figure 4: (i) Comparison of the matrix-isolation IR spectra in the N_2 matrix and simulated IR stick spectra of the complexes obtained at the MP2/aug-cc-pVDZ level of calculation in the ν_{CH}, ν_{CO}, and ν_{OH} regions. All the IR spectra are recorded at 8 K. Matrix-isolation IR spectra of [$CHCl_3$−CH_3OH] mixture after annealing at 30 K (a), [$CHCl_3$−CH_3OH] mixture after deposition at 8 K (b), CH_3OH after annealing at 30 K (c), $CHCl_3$ after annealing at 30 K (d), simulated IR stick spectra of the complex CHM4 (e), CHM3 (f), CHM2 (g), and CHM1 (h). (ii) Optimised geometry of the four conformers at the MP2/aug-cc-pVDZ level.

C-O (ν_{CO}) and the O-H (ν_{OH}) stretching modes of CH_3OH are observed at 1034 cm^{-1} and 3664 cm^{-1}, respectively. New peaks are observed after annealing [$CHCl_3-CH_3OH$] mixture matrix those are absent in the monomer spectra.In the ν_{CH} region, a new peak is observed at 3045 cm^{-1}that is 21 cm^{-1} red-shifted compared to the monomer. Two new peaks are observed at 1024 and 1030 cm^{-1}. These peaks are red-shifted by 10 and 4 cm^{-1} compared to theν_{CO} of the monomer. Two new peaks are observed at the 3645 and 3657 cm^{-1} in the IR spectrum of [$CHCl_3-CH_3OH$] mixture just after deposition at 8 K and gains intensity after annealing the matrix. These peaks are red-shifted by 19 and 7 cm^{-1} compared to the monomer ν_{OH}. All the new peaks are assigned to the 1:1 [$CHCl_3-CH_3OH$] complex.

Four minima have been obtained on the [$CHCl_3-CH_3OH$] dimer potential energy surface (Figure 4, ii). The most stable structure corresponds to the H-Bond isomer (CHM1) stabilised by C-H···O interaction with D_0 of 3.65 kcal/mol. The next stable minimum (CHM2) is stabilised by bifurcated H-bond of O-H···Cl type (D_0 = 1.57 kcal/mol). The third stable minimum (CHM3) with D_0 of 1.25 kcal/mol is stabilised by C-Cl···O X-Bond interaction. The least stable minimum is stabilised by single O-H···Cl H-bond with $D_0$of 1.17 kcal/mol. A red-shift of 10, 1, 3, and 1 cm^{-1} are simulated in the ν_{CH} mode of CHM1, CHM2, CHM3, and CHM4, respectively. A simulated red-shift of 8, 4, and 1 cm^{-1} are observed corresponding to ν_{CO} mode for CHM1, CHM3, and CHM4, respectively. A blue-shift of 3 cm^{-1} is simulated for the ν_{CO} mode of CHM2. A red-shift of 9, 15, 8, and 19 cm^{-1} are predicted in the ν_{OH} modefor CHM1, CHM2, CHM3, and CHM4, respectively. Experimental IR spectra is compared with the simulated IR spectra of all the complexes. It has been concluded that the 1:1 complex of [$CHCl_3-CH_3OH$] is stabilised by C-H···O H-Bond and C-Cl···O X-Bond interaction in N_2 matrix.

The IR spectra in the C-Cl stretch (ν_{CCl}) and ν_{CH} modes of $CHCl_3$, and in the ν_{OH} and O-H bending (δ_{OH}) vibration modes of C_2H_5OH in N_2 matrix are presented in Figure 5. The ν_{CCl} appears at 765 cm^{-1} with splitting due to the isotope effect.The C_2H_5OH exists in anti and gauche conformers in the gas phase and are observed under experimental conditions from the ν_{OH} peaks at 3652 and 3649 cm^{-1}, respectively[16]. Thermal isomerisation from the anti to the gauche conformer has been observed in N_2 matrix. The δ_{OH} for the anti and gauche conformers appear at 1256 and 1261 cm^{-1}, respectively. Two new peaks are observed at 757 and 777 cm^{-1} for ν_{CCl} mode after annealing the [$CHCl_3-C_2H_5OH$] mixture matrix and are red and blue-shifted by 8 and 12 cm^{-1}, respectively, compared to the monomer ν_{CCl}. Two new peaks are observed at 3034 and 3039 cm^{-1} corresponding to the ν_{CH} mode of $CHCl_3$ and are red-shifted by 32 and 27 cm^{-1}, respectively, compared to the monomer. Two new peaks are observed for ν_{OH} mode at 3639 and 3642 cm^{-1}. These two peaks are red-shifted by 10 cm^{-1}compared to the ν_{OH} of the gauche and anticonformers of C_2H_5OH. Two new peaks are observed at 1251 and 1266 cm^{-1} for the δ_{OH} mode those are red and blue-shifted by 4 and 5 cm^{-1} compared to the monomer peaks. All the observed new peaks are assigned to the 1:1 [$CHCl_3-C_2H_5OH$] complex.

Three minima have been obtained on the [$CHCl_3-C_2H_5OH$] dimer potential energy surface for both anti and gauche conformers of C_2H_5OH. Herein, the complex structure and simulated vibrational frequencies of anticonformer is discussed (Figure 5). The most stable structure corresponds to the H-Bond isomer (CHE1) stabilised by C-H···O H-Bond interaction with D_0 of 4.47 kcal/mol. The next stable minimum (CHE2) is characterised by H-bond of O-H···Cl type with D_0 of 1.86 kcal/mol. The third stable minimum (CHE3) is characterised by C-Cl···O halogen bonding interaction with D_0 of 1.81 kcal/mol. Simulated harmonic vibrational frequency exhibit a red-shift of 12 and 7 cm^{-1} for CHE1 and CHE2, respectively, and a blue-shift of 9 cm^{-1} for CHE3, in the ν_{CCl} mode. The ν_{CH} mode is red-shifted by 26 and 4 cm^{-1} compared to the monomer in CHE1 and CHE3, respectively. A blue-shift of 2 cm^{-1} is simulated in the ν_{CH} mode for CHE2. The simulated ν_{OH} mode for CHE1, CHE2, and CHE3 are red-shifted by 14, 14, and 4 cm^{-1}, respectively. The δ_{OH} mode is predicted to be red-shifted by 4 cm^{-1} in CHE1, blue-shifted by 10 cm^{-1} in CHE2, and no shift in CHE3. The peaks at 757 and 777 cm^{-1} are assigned to the H-Bond complex (CHE1 and CHE2) and X-Bond complex (CHE3), respectively. The 3034 and 3039 cm^{-1} peaks corresponding to the ν_{CH} mode are assigned to the CHE1 type complex of anti and gauche conformers of C_2H_5OH, respectively. The ν_{CH} mode of the complexes are simulated at 3040 and 3047 cm^{-1} for the anti and gauche conformer of CHE1 type complex, respectively. The two peaks at 1251 and 1266 cm^{-1} are assigned to the δ_{OH} mode of CHE1 and CHE2, respectively. The peaks at 3639 and 3642 cm^{-1} are assigned to the ν_{OH} mode of H-Bond and X-Bond complexes, respectively. Thus, all the three complexes of $[CHCl_3{-}C_2H_5OH]$are being formed in the N_2 matrix under the experimental conditions. Moreover, the signatures of the complexes of both anti and gauche conformers

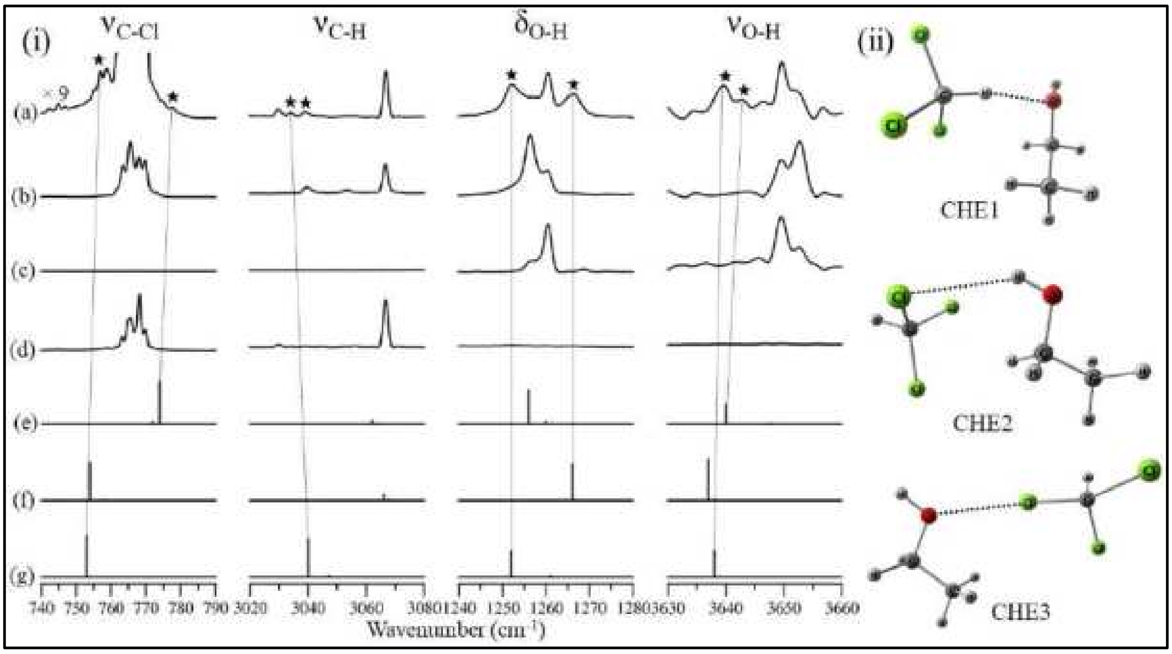

Figure 5: *(i) Comparison of the matrix-isolation IR spectra in the N_2 matrix and simulated IR stick spectra of the complexes obtained at the MP2/aug-cc-pVDZ level of calculation in the ν_{CCl}, ν_{CH}, δ_{OH}, and ν_{OH} regions. All the IR spectra are recorded at 8 K. Matrix-isolation IR spectra of $[CHCl_3{-}C_2H_5OH]$ mixture after annealing at 30 K (a), $[CHCl_3{-}C_2H_5OH]$ mixture after deposition at 8 K (b), C_2H_5OH after annealing at 30 K (c), $CHCl_3$ after annealing at 30 K (d), simulated IR stick spectra of the complex CHE3 (e), CHE2 (f), and CHE1 (g). (ii) Optimised geometry of the three conformers at the MP2/aug-cc-pVDZ level.*

of C_2H_5OH are observed for [$CHCl_3$−C_2H_5OH].

The intrinsic propensity for the 1:1 complex formation between alcohols and halogenated compounds has been investigated to understand the heterogenous interactions between the solvent molecules at the molecular level. The two halogenated solvents used in the work differ by a chlorine atom. One of the chlorine atoms of CCl_4 is substituted by a hydrogen atom in $CHCl_3$. The CCl_4 is a non-polar solvent with T_d symmetry whereas $CHCl_3$ is a weakly polar solvent (1.04 D) with C_{3v} symmetry. Exclusive formation of X-Bond complex stabilised by C-Cl···O interaction have been identified in the [CCl_4−CH_3OH] and [CCl_4−C_2H_5OH] mixtures. Thus, CCl_4 exhibits specific interaction of X-Bond type with the two simplest alcohols. Situation is not so straight forward for $CHCl_3$ that participate in non-specific interactions, such as, H-Bond and X-Bond with CH_3OH and C_2H_5OH. Formation of both C-H···O and C-Cl···O interactions are evidenced in case of [$CHCl_3$−CH_3OH] and [$CHCl_3$−C_2H_5OH] mixture. Moreover, O-H···Cl H-Bond interaction is also evidenced in case of the higher alcohol, i.e., C_2H_5OH. Natural Bond Orbital (NBO) analysis and Energy Decomposition Analysis (EDA) have been performed to understand the nature and origin of the non-covalent interactions present in the complexes. In case of the most stable complex (CM1) of [CCl_4−CH_3OH], the total charge transfer from CH_3OH to the CCl_4 is 4.28 me. For CM2 and CM3, the total charge transfer is 8.63 and 9.95 me, respectively. Partitioning of the energy into the constituent components shows that CM1 is majorly stabilised by electrostatics interaction (4.33 kcal/mol) followed by CM2 (2.88 kcal/mol), and CM3 (2.09 kcal/mol). The total charge transfer in the complexes of [CCl_4−C_2H_5OH] mixture are 1.80 (CE1), 11.31 (CE2), and 9.60 (CE3) me. The electrostatic component of the total interaction energy for CE1, CE2, and CE3 are 4.20, 3.26, and 2.66 kcal/mol, respectively. The four conformers of the [$CHCl_3$−CH_3OH] complex have a total charge transfer of 12.36, 9.83, 2.46, and 11.46 me for CHM1, CHM2, CHM3, and CHM4, respectively. The electrostatic component for the four complexes are 6.85 (CHM1), 1.95 (CHM2), 2.80 (CHM3), and 1.62 (CHM4) kcal/mol, respectively. The total charge transfer in the three complexes of [$CHCl_3$−C_2H_5OH], i.e., CHE1, CHE2, and CHE3, are 10.71, 14.49, and 0.61 me, respectively. The corresponding electrostatic components of stabilisation are 8.47, 2.96, and 3.04 kcal/mol.

Formation of complexes under matrix isolation conditions is governed by the diffusion controlled process during annealing. Charge transfer is a predominant factor towards the stabilisation of hydrogen and halogen-bonded complexes. Charge transfer is a short-range interaction between overlapping pair of orbitals from the two molecules. Charge transfer interaction dominates when the distance between the individual molecules is close to the equilibrium geometry of the complex. Diffusion of the trapped molecular species must be influenced by the electrostatic interaction that is a long-range force. The X-Bond complex of [CCl_4−CH_3OH] and [CCl_4−C_2H_5OH] is dominated by the electrostatic interaction that leads to the exclusive formation of X-bond complex under matrix isolation conditions. In case of [$CHCl_3$−CH_3OH] and [$CHCl_3$−C_2H_5OH], the charge transfer along with the electrostatic component is significant for the H-Bond complexes (CHM1 and CHE1). Among the other minima, the X-Bond complexes (CHM3 and CHE3) are majorly stabilised by electrostatic interaction and hence, are formed under the low temperature matrix isolation experiments. Formation of both CHE2 and CHE3 in case of the [$CHCl_3$−C_2H_5OH] is explained from the almost equal electrostatic component towards the total stabilisation energy. Although, the charge transfer is much higher in H-Bond complex (CHE2) compared to the X-Bond complex (CHE3).

4. Conclusion

The current investigation provides a molecular level understanding of the intermolecular non-covalent interaction in the halogenated solvent-alcohol mixtures. Two halogenated solvents, CCl_4 and $CHCl_3$ have been used along with CH_3OH and C_2H_5OH. Complexes have been characterised by matrix isolation infrared spectroscopy and electronic structure calculations. Formation of the complexes are monitored by comparing the experimental IR spectra with simulated frequencies of different vibrational modes. Exclusive formation of X-Bond complex stabilised by C-Cl···O interaction is observed in the 1:1 mixture of [CCl_4-CH_3OH] and [CCl_4-C_2H_5OH]. Although, H-Bond complex stabilised by O-H···Cl interaction is almost equally stable on the dimer potential energy surface. Formation of both H-Bond complex stabilised by C-H···O interaction and X-bond complex stabilised by C-Cl···O interaction are observed in the 1:1 mixture of [$CHCl_3$-CH_3OH] and [$CHCl_3$-C_2H_5OH]. Moreover, formation of another H-bond complex, stabilised by O-H···Cl interaction is also observed in [$CHCl_3$-C_2H_5OH] mixture. Charge transfer and electrostatic interactions are the two major contributorstowards the stabilisation and formation of the complexes under matrix isolation conditions. Higher contribution of electrostatic component in the total stabilisation energy of the X-Bond complex leads to the exclusive formation of X-Bond complex in [CCl_4−CH_3OH] and [CCl_4−C_2H_5OH] mixtures. In case of [$CHCl_3$−CH_3OH] and [$CHCl_3$−C_2H_5OH], the charge transfer along with the electrostatic components are significant for the H-Bond complex. The X-Bond complex are majorly stabilised by electrostatic interaction. Hence, both the complexes are observed under the low temperature matrix isolation experiments.

Acknowledgement

This study is supported by the financial grant received from the Science and Engineering Research Board (SERB), Department of Science and Technology (DST), Government of India [EMR/2016/003756 and CRG/2020/002301]. AC would like to acknowledge financial support received under Women Scientist Scheme-A, Department of Science and Technology (DST), Government of India [SR/WOS − A/CS − 67/2017]. Authors thank computer centre of BITS-Pilani, Pilani Campus, for providing time in High-Performance Computational Facility,where all calculations were performed.

References

(1) Marcus, Y. The properties of organic liquids that are relevant to their use as solvating solvents. Chemical Society Reviews 1993, 22, 409–416.

(2) Arunan, E.; Desiraju, G. R.; Klein, R. A.; Sadlej, J.; Scheiner, S.; Alkorta, I.; Clary, D. C.; Crabtree, R. H.; Dannenberg, J. J.; Hobza, P., et al. Definition of the hydrogen bond (IUPAC Recommendations 2011). Pure and applied chemistry 2011,83, 1637–1641.

(3) Arunan, E.; Desiraju, G. R.; Klein, R. A.; Sadlej, J.; Scheiner, S.; Alkorta, I.; Clary, D. C.; Crabtree, R. H.; Dannenberg, J. J.; Hobza, P., et al. Defining the hydrogen bond: An account (IUPAC Technical Report). Pure and Applied Chemistry 2011, 83, 1619–1636.

(4) Desiraju, G. R.; Ho, P. S.; Kloo, L.; Legon, A. C.; Marquardt, R.; Metrangolo, P.; Politzer, P.; Resnati, G.; Rissanen, K. Definition of the halogen bond (IUPAC Recommendations 2013). Pure and applied chemistry 2013, 85, 1711–1713.

(5) Cavallo, G.; Metrangolo, P.; Milani, R.; Pilati, T.; Priimagi, A.; Resnati, G.; Terraneo, G. The halogen bond. Chemical reviews 2016, 116, 2478–2601.

(6)Munaò G, Costa D, Saija F, Caccamo C. Simulation and reference interaction site model theory of methanol and carbon tetrachloride mixtures. The Journal of chemical physics 2010, 132, 084506.

(7)Musso M, Torii H, Ottaviani P, Asenbaum A, Giorgini MG. Noncoincidence effect of vibrational bands of methanol/CCl4 mixtures and its relation with concentration-dependent liquid structures. The Journal of Physical Chemistry A 2002, 106, 10152-10161.

(8)Veldhuizen R, De Leeuw SW. Molecular dynamics study of the thermodynamic and structural properties of methanol and polarizable/non-polarizable carbon tetrachloride mixtures. The Journal of chemical physics 1996, 105, 2828-2836.

(9) Paraskevopoulos GC, Missen RW. Thermodynamic properties of solutions of alcohols and carbon tetrachloride. Part 1. Free energies and volumes of mixing. Transactions of the Faraday Society. 1962, 58, 869-878.

(10)Kalhor, P.; Li, Q.-Z.; Zheng, Y.-Z.; Yu, Z.-W. Is the Fourier transform infrared free-OH band of t-butanol only from free OHs? Case studies on the binary systems of the alcohol with CCl4 and CHCl3. The Journal of Physical Chemistry A 2020, 124, 6177–6185.

(11) TURBOMOLE V7.3 2017, a development of University of Karlsruhe and Forschungszentrum Karlsruhe GmbH, 1989-2007, TURBOMOLE GmbH, since 2007; available from http://www.turbomole.com.

(12) Lu T, Chen F. Multiwfn: a multifunctional wavefunction analyzer. Journal of computational chemistry 2012, 33, 580-592.

(13) Glendening, E. D.; Landis, C. R.; Weinhold, F. NBO 6.0: Natural bond orbital analysis program. Journal of computational chemistry 2013, 34, 1429–1437.

(14) Turney, J.M.;Simmonett, A.C.; Parrish, R.M.; Hohenstein, E.G.; Evangelista, F.A.;Fermann, J.T.;Mintz, B.J.; Burns, L.A.; Wilke, J.J.; Abrams, M.L.; Russ, N.J. Psi4: an open-source ab initio electronic structure program. Wiley Interdisciplinary Reviews: Computational Molecular Science 2012, 2, 556-565.

(15) Pal, D.; Agrawal, S. K.; Chakraborty, A.; Chakraborty, S. Competition between the hydrogen bond and the halogen bond in a [CH3OH–CCl4] complex: a matrix isolation IR spectroscopy and computational study. Physical Chemistry Chemical Physics 2020, 22, 22465–22476.

(16) Agrawal, S. K.; Pal, D.; Chakraborty, A.; Chakraborty, S. Ethanol monomer revisited: Thermal isomerisation between anti and gauche conformers in Ar and N2 matrix. Chemical Physics 2020, 537, 110851.

About the authors

Mr. Dhritabrata Pal *is a Ph.D. scholar in the Department of Chemistry, Birla Institute of Technology and Science, Pilani, Pilani Campus. He obtained his Master degree in Chemistry from Calcutta University in 2017. His area of research involves understanding the nature and origin of non-covalent interaction, specially Selenium centered hydrogen bonding, using Matrix Isolation Infrared Spectroscopy and electronic structure calculations.*

Mr. Sumit Kumar Agrawal *is Ph.D. scholar in the Department of Chemistry, Birla Institute of Technology and Science, Pilani, Pilani Campus. He received his BS-MS dual degree from Indian Institute of Science Education and Research (IISER), Mohali. His research interest focuses on halogen bonding interaction using a combination of matrix isolation infrared spectroscopy and various computational techniques.*

Dr. Amrita Chakraborty *joined the Department of Chemistry, Birla Institute of Technology and Science, Pilani, Pilani Campus as DST-Women scientist (WOSA) on 2018. She obtained Ph.D. degree from University of Calcutta. After completion of Ph.D she worked in Université Paris Sud (France) and Freie Universität Berlin (Germany) as postdoctoral fellow for two years. She worked as research associate in Indian Association for the Cultivation of Science (Kolkata) and S. N. Bose National Centre for Basic Sciences (Kolkata). She was attached with Techno India University (Kolkata) for more than two years. Her broad research area is molecular spectroscopy. Presently involves in understanding of non-covalent interactions (Halogen/Hydrogen bonding) in atmospherically relevant molecules and their complexes in cold matrix.*

Dr. Shamik Chakraborty*, Associate Professor, became a member of the Department of Chemistry, Birla Institute of Technology and Science, Pilani, Pilani campus in 2012. Dr. Chakraborty obtained Ph.D. from Tata Institute Fundamental Research (TIFR), Mumbai, India, in the area of high-resolution laser spectroscopy in the gas phase. Prior to his appointment at BITS, he worked in Centre Laser, University Paris Sud (France), Institute for Optics and Atomic Physics, Technical University Berlin (Germany), and Chemical Resources Laboratory, Tokyo Institute of Technology (Japan) as Post-Doctoral Research Fellow. His broad research interest focuses on (i) understanding the nature and origin of non-covalent interactions using Matrix Isolation Infrared Spectroscopy, (ii) competition between charge transfer and proton transfer processes, (iii) atmospheric science and astrochemistry.*

Photochemical Oxaziridine Conversion and Subsequent Lactam Formation Pathways of 3,5,5-trimethyl-1-pyrroline 1-oxide (3-Me-DMPO)

Sindhuja Sen[a], Dilawar Singh Sisodiya[a] and Anjan Chattopadhyay[a]*
[a]*Department of Chemistry, Birla Institute of Technology and Science (BITS), Pilani –K.K. Birla Goa Campus, Goa, 403 726, India*
Email:anjan@goa.bits-pilani.ac.in

Abstract

This computational work has explored the photochemistry of 3,5,5-trimethyl-1-pyrroline1-oxide (3-Me-DMPO), a well-known spin-trapping agent. Similar to the other members of this substituted-pyrroline1-oxide series, it forms oxaziridine on photo-irradiation. The subsequent cyclic amide or lactam was reported to form from oxaziridinewhen the cyclic nitrone was heated to 150^0C for 30 min. It was assumed to happen through a [1,2]-H shift. The quantum mechanical studies carried out in this work has clearly established the mechanisms of both oxaziridine and lactam formationsfrom 3-Me-DMPO. Photo-excitation of this cyclic nitrone system is found to strongly populate the second excited singlet state (S_2) which is dominated by the configuration arising from theHOMO→LUMO excitation. This vertically excited S_2 state then undergoes an avoided crossing (S_2/S_1). This finally leads towards the low-lying CNO-kinked S_0/S_1 conical intersection, located around 65 kcal/mol below the vertically excited S_2 state, which forms the photoproduct oxaziridine. The lactam (pyrrolidone) formation takes place from oxaziridine through a transition state on the ground state surface. This path is characterized by a H-shift to the nitrogen atom from the adjacent carbon atom of the oxaziridine ring which has established that the earlier prediction about this path was correct. Few other thermal reaction pathways of this nitrone have been also detected during our investigations

1. Introduction

Similar to 5,5-dimethyl-1-pyrroline 1-oxide (DMPO) [1-3], 3-methyl substituted-DMPO (3-Me-DMPO) is also a spin-trapping agent which is well-known in the detection of free radicals [4]. Synthesis of DMPO and its photo-irradiation studies were first done by Sir Alexander Todd and his group [5]. Kaminsky and Lamchen[6-8] investigated the photo-irradiations and subsequent product formations of several pyrroline 1-oxide systems where methyl substitutions were done at different positions on the ring.They found that an initial photo-product (oxaziridine) was formed on photo-irradiation of these cyclic nitrones, however, the subsequent steps were very different. Their observation on the post-oxaziridine formation steps for 2-Me-DMPO was different from that of DMPO and 3-Me-DMPO. Photo-irradiation on these latter cyclic nitrones gave oxaziridines and when the photo-product was heated (for 3-Me-DMPO heated to 150^0C for 30 min.) and then cooled, a solid was formed, which recrystallized as white crystals. This product was identified as the cyclic amide (lactam) or pyrrolidone. They concluded that due to the unsubstituted 2-position, both DMPO and its 3-methyl-substituted analogue (3-Me-DMPO) behave similarly. The lactam formation from oxaziridine was assumed to be due to a [1,2]-H shift in these two cases.

In recent times,Chattopadhyay and co-workers have explored the photochemistry and oxaziridine-lactam conversion reactions of

DMPO, 2-Me-DMPO and other substituted-pyrroline 1-oxides using high-level quantum mechanical calculations [9, 10]. Their computational studies have clearly supported the experimental observations of Kaminsky and Lamchen [6-8] which has now established the mechanism behind their product formations. Presence of low-lying conical intersections [11, 12] in their photochemical reaction paths leading to the photoproduct formation was noticed. In fact, similar reaction paths were also noticed for other cyclic nitrone-like compounds like 2H-imidazole 1-oxides and 2H-imidazole 1,3-dioxides [13, 14]. This current work is an attempt to check the photochemical oxaziridine conversion and the thermal lactam formation pathways of 3-Me-DMPO system. It will be interesting to find out whether similar conical intersection also governs the photochemical path of this pyrroline 1-oxide system or not. Moreover, the possibility of a [1,2]-H shift at the unsubstituted 2-position for lactam formation can be investigated, as well. A schematic diagram of these reactions is shown below (Figure 1).

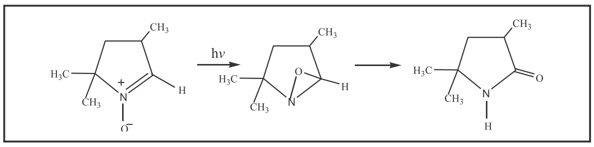

Figure 1: *A schematic diagram of the oxaziridine and lactam formation from 3-Me-DMPO*

2. Computational Details

In this present work, the quantum mechanical studies on the 3-methyl-substituted DMPO molecule are carried out using the Gaussian 09 (and 16) [15], GAMESS-US [16] and Molpro suite of program [17]. Geometries related to the photochemical paths (energy minima, conical intersections) on the potential energy surfaces (PES) are optimized at the CASSCF/6-31G* [18-22] level in Gaussian09 and at the Mixed Reference Spin-Flip (MRSF) TDDFT level using BHHYP/6-31G*[23-26] in GAMESS-US suite of program. Using the latter method, we were successful in optimizing the excited state minima, as well. It must be added here that we have avoided the LR-TDDFT method here as they may not properly capture the doubly excited state properties which is tackled properly by the SF-TDDFT methods. However, the original spin-flip method (SF-TDDFT) may suffer from spin-contamination problem. Therefore, we have employed the Mixed-Reference Spin-Flip version of this TDDFT (MRSF-TDDFT) method which does not have such deficiency. On top of the CASSCF optimized geometries, dynamic correlation treatment of CASPT2 level has been performed[27-29] through single point calculations using the Molpro program. The CASSCF calculations have been carried out using (4,4) and (6,6) active spaces. Some important orbitals of the (4,4) active space are shown in Figure 2. To verify the proposed reaction paths, we have employed the linear interpolation in internal coordinate (LIIC) plots between two geometries at the mentioned spin flip-TDDFT level. Additionally, radiative transition [30,31] calculations have been performed using the GUGA (Graphical Unitary Group Approach)-based configuration interaction singles and doubles (CISD) technique through the GAMESS suite of program. This GUGA CISD code [32-35] has been used to perform transition properties between the two configuration interaction wave functions at the ground state equilibrium geometry. In these CISD calculations, the Restricted Hartree-Fock (RHF)/6-31G* method calculates the self-consistent molecular orbital (SCFMO) of the ground states in the first step and these MOs are used for the configuration interaction steps.

The transition states (TS) have been located using the normal TS technique which is based on the Berny algorithm[36]. The thermal oxaziridine-lactam conversion path involving the TS has been carried out at both CASSCF and DFT (B3LYP/6-311G**) level of calculations. Other thermal reaction paths were calculated only at the above-mentioned DFT level of theory. Electrostatic potential-based atomic charges are calculated using the Merz−Kollman[37, 38] scheme at different geometries. For visualization of the output files, we have used Chem Craft software in this work.

3. Results & discussions

Photochemical reaction pathway CASSCF, CASPT2, CISD results

The ground state geometry of 3-Me-DMPO has been optimized at the CASSCF/6-31G* level. The important MOs of the (4,4) active space are shown in Figure 2. The optimized geometries with the bond lengths are shown in Figure 3. Studies of transition properties have revealed that the S_0-S_1 is a weakly allowed transition while the S_0-S_2 is a strongly allowed one (Table 1). The vertical excitation energies (VEE) corresponding to the S_0-S_1 and S_0-S_2 transitions are found to be 110 and 127 kcal/mol, respectively, at the CASPT2 level of calculation (Table 1).

Table 1.Transition properties of S_0-S_1 and S_0-S_2 transitions at the ground state optimized geometry of 3-Me-DMPO

Transition	Transition Moment (Debye)	Oscillator Strength	VEE (at CASPT2)	VEE (at MRSF TDDFT)
S_0-S_1	0.073	0.0002	110	102
S_0-S_2	3.355	0.4861	127	142

The first excited singlet state (S_1) is mostly contributed by the HOMO–1→LUMO excitation while the second excited singlet state (S_2) is largely contributed by HOMO→LUMO excitation. Some contribution from the doubly excited configuration has been also noticed here. The allowed S_0-S_2 transition is associated with a transition moment value of 3.36 Debye. On the other hand, the S_0-S_1 transition is comparatively much weaker.

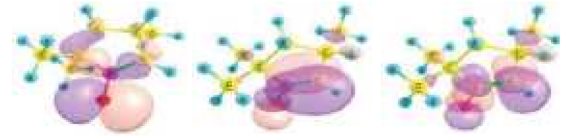

Figure 2: *Important orbitals in the active space of 3-Me-DMPO*

The low-lying conical intersection (S_0/S_1) geometry (Figure 3c) named as CI, is found to be responsible for the oxaziridine (OX) formation (Figure 3b). This CI is situated around 64 kcal/mol below the vertically excited S_2 state. Following its gradient difference (GD) vectors, the oxaziridine geometry was located at 2 kcal/mol (Table 2) above the ground state nitrone geometry (GS).

The atomic charge analysis (Table 3) clearly indicates that an electronic cloud is transferred from the oxygen atom towards the nitrogen during the photo-excitation process. During the nitrone-oxaziridine conversion the CNO ring is formed where the sp^2 nitrogen (in nitrone) becomes sp^3 hybridized with a lone pair on it in oxaziridine.

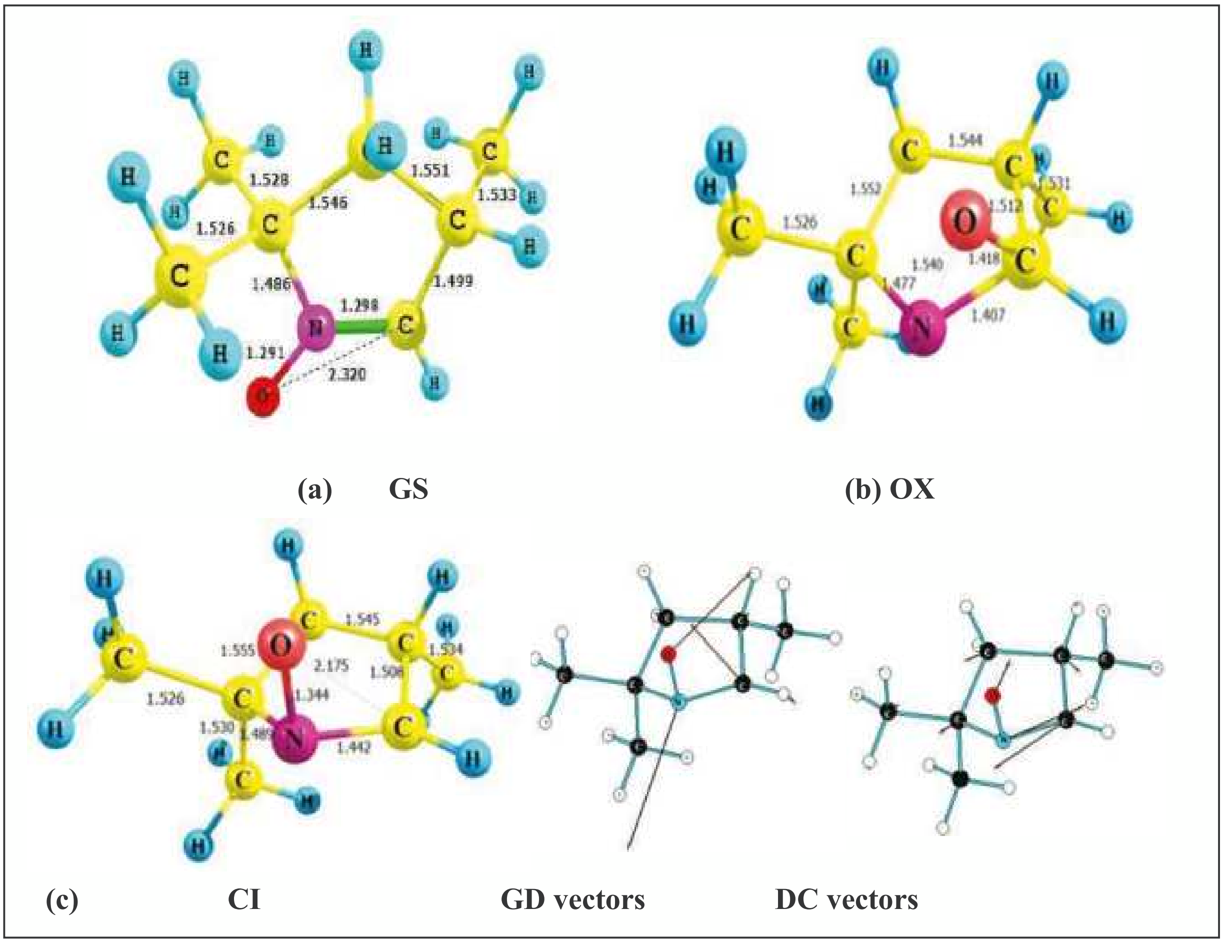

(a) GS **(b) OX**

(c) CI **GD vectors** **DC vectors**

Figure 3: *Optimized geometries of 3-Me-DMPO (a) ground state GS and (b) oxaziridine OX (c) CI with respective GD and DC vectors at the CASSCF level.*

MRSF-TDDFT results

Though we were able to track the path of oxaziridine formation from the low-lying CNO-kinked S_0/S_1CI at the CASSCF level, the link between the vertically excited state and the mentioned CI was not clear. This is primarily due to our failure to optimize any minimum energy geometry on the S_2 surface or S_2/S_1

Table 2: *Absolute and Relative Energies at CASSCF, CASPT2, MRSF-TDDFT level for geometries involved in the oxaziridine formation from 3-Me DMPO.*

Geometry	CASSCF		CASPT2		MRSF-TDDFT	
	Absolute energy (in Hartree)	Relative energy (in kcal/mol)	Absolute energy (in Hartree)	Relative energy (in kcal/mol)	Absolute energy (in Hartree)	Relative energy (in kcal/mol)
GS	-401.90825^a -401.97242^b	0^a 0^b	-403.13982^a	0^a	-404.2293275	0
S_1 minimum	-	-	-	-	-404.1045625	78.29
S_2 minimum	-	-	-	-	-404.0692959	100.42
CI	-401.81354^a -401.83752^b	59.43^a 84.65^b	-403.03863^a	63.5^a	-404.1117864	73.76
OX	-401.94409^a -401.97495^b	-22.49^a -1.59^b	-403.13555^a	2.68^a	-404.2167052	7.92

^{a}[4,4] active space, ^{b}[6,6] active space crossing at the CASSCF level. The path through which S_0/S_1CI comes is required to be understood. At the MRSF-TDDFT level, we were able to optimize the minimum energy S_2 geometry which is situated around 42 kcal / mol below the vertically excited S_2 state (Table 2). We have also optimized the S_1 minimum at this level. Finally, we have re-optimized the S_0/S_1 CI at this spin-flip level which almost resembles the CASSCF CI geometry. Interestingly, the S_2 minimum geometry and the CI geometries have similar CNO-kinked structures. All figures optimized at this spin-flip level are shown in Figure 4.

Table 3: *Atomic charges at different geometries of 3-Me-DMPO at the Merz-Kollman scheme*

GS	CI	OX
1 C -0.4023	1 C -0.3355	1 C -0.3142
2 C 0.5656	2 C 0.1197	2 C 0.7256
3 N 0.3575	3 N -0.2169	3 N -0.4645
4 C -0.3281	4 C 0.0174	4 C 0.2079
5 C 0.3819	5 C -0.1959	5 C 0.2298
6 C -0.5337	6 C -0.4746	6 C -0.4532
7 C -0.4763	7 C -0.4670	7 C -0.5108
8 O -0.6114	8 O -0.2648	8 O -0.2784
19 C -0.3837	19 C -0.4769	19 C -0.4198

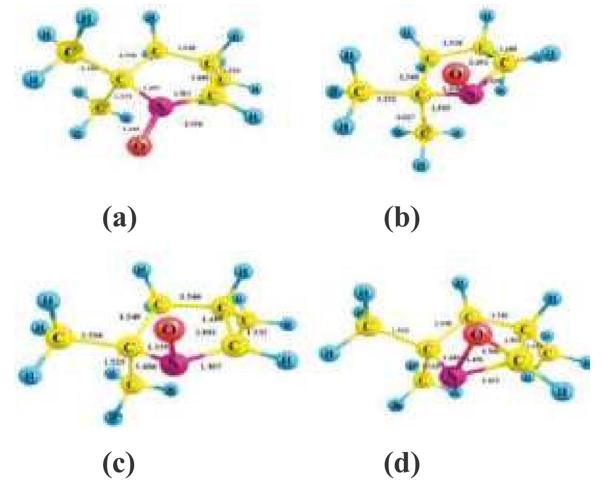
(a) **(b)**

(c) **(d)**

Figure 4: *Optimized geometries of 3-Me-DMPO (a) ground state GS (b) S_2 minimum(c) CI (d) Oxaziridine OX at the MRSF TDDFT level.*

To understand the reaction path, we have employed the linear interpolation in internal coordinate (LIIC) plots between two geometries (Figure 5). The plots between the vertically excited S_1/S_2 geometries and the S_2 minimum geometry reveals that near the latter, the S_2-S_1 energy gap becomes very low and indicates an avoided crossing geometry. To reach this S_2/S_1 avoided crossing geometry, the vertically excited S_2 state must overcome a small barrier. The LIIC plots between the S_2/S_1 avoided crossing geometry and S_0/S_1 CI clearly reveals a barrier-less path. Finally, these plots also reveal that the predicted path between the latter CI geometry and OX geometry is correct. On the other hand, a significant barrier has been noticed between the S_1 minimum and the CI which indicates a low probability of this path.

Thermal Reaction pathways

CASSCF and CASPT2 results

A transition state situated around 43 kcal/mol above the oxaziridine (OX) structure at the CASSCF level (Figure 6) has been optimized which has shown the possibility of lactam formation through a [1,2]-H shift. The value of this energy barrier at the CASPT2 level is around 34 kcal/mol. Though it is possible that there is a prior step in which the C-O bond first becomes co-planar with the 5-membered ring and the second step is the [1,2]-H shift. The single imaginary frequency of 1612*i* cm^{-1} leads to the N−H bond formation while the C-H bond breaks and this leads to the pyrrolidone formation from oxaziridine.

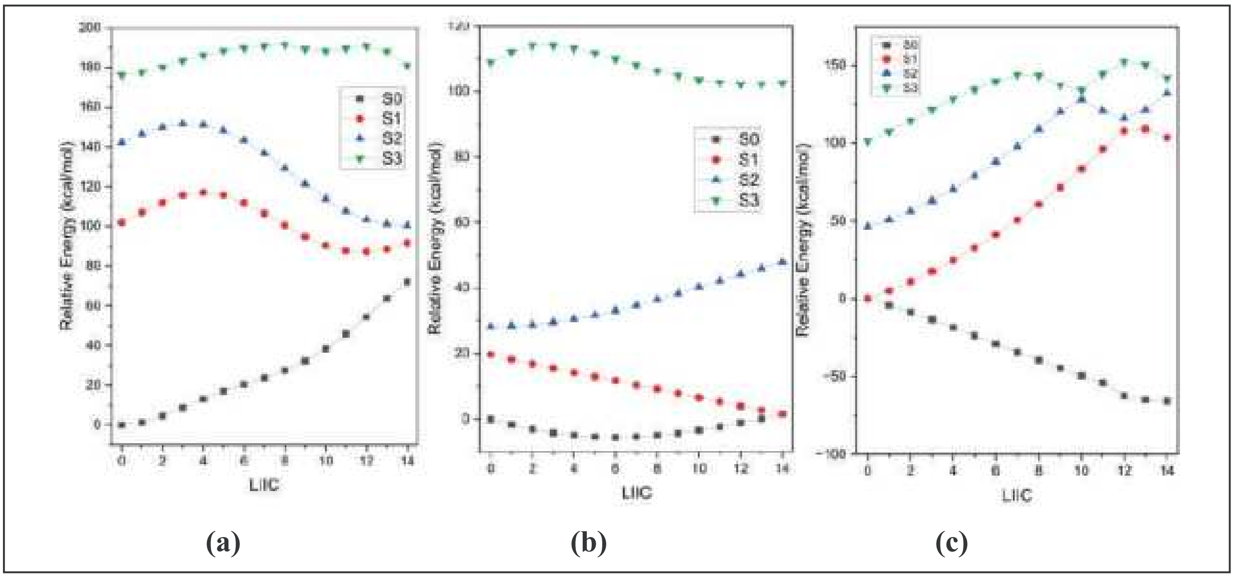

Figure 5: *LIIC plots between (a) vertically excited geometry and S_2 minimum (S_2/S_1 avoided crossing) (b) S_2 minimum (S_2/S_1 avoided crossing) and S_0/S_1 conical intersection (c) S_0/S_1 conical intersection and OX.*

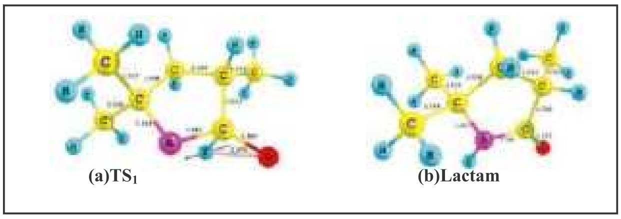

Figure 6: *Optimized geometry of (a) transition state and (b) lactam at CASSCF level.*

DFT results

Starting with the same CAS-optimized TS structure at the B3LYP/6-311G** level, we have found a transition state geometry (Figure 7) which has a substantially high imaginary frequency of 1905*i* cm^{-1}. However, in this case, the transition vectors have indicated an intramolecular proton transfer from the OH group to the adjacent nitrogen, a process well-known as the lactam-lactim tautomerization. The calculated barrier height is around 53 kcal/mol.

Interestingly, our attempt to locate a transition state starting from an oxaziridine-type geometry with a stretched C-O bond has led to a [1,2]-H shift which forms the lactam. The single imaginary frequency of 515*i* cm^{-1} has clearly indicated this cyclic amide formation. We have confirmed the reactant (oxaziridine) and the

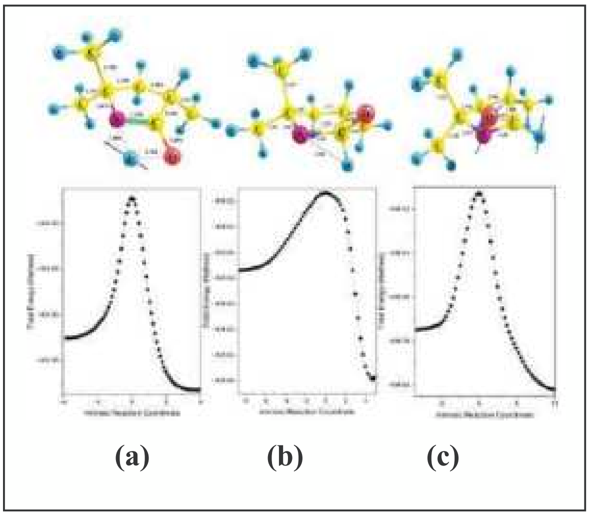

Figure 7: *TS geometries and IRC plots (a) lactam-lactim (b)OX-Lactam (c) OX-parent nitrone (3-Me-DMPO) conversions.*

product (Lactam) through the IRC analysis on both sides of the transition state (Figure 7). The energy barrier at the B3LYP/6-311G** level is around 42 kcal/mol.

A third transition state on the ground state surface has been identified at the DFT level of calculations. This has almost the same energy value as the previous one and makes a barrier of 42 kcal/mol with respect to the oxaziridine. However, it goes towards the parent nitrone compound as evidenced by the transition vectors and the IRC analysis.

4. Conclusion

The oxaziridine and lactam conversion pathways of 3-methyl-substituted DMPO have been explored using different quantum mechanical tools. The results indicate that a low-lying S_0/S_1 conical intersection with a twisted CNO moiety is responsible for the photoproduct (oxaziridine) formation. This characteristic of the photochemical path is similar to that of the DMPO and 2-Me-DMPO systems reported by us, previously. An initial electron cloud transfer from the oxygen towards the nitrogen takes place and relaxation from the Franck-Condon excited state geometry of S_2 state goes toward the mentioned CNO-kinked S_0/S_1conical intersection. The latter subsequently forms the oxaziridine photo-product. The lactam formation from oxaziridine faces an energy barrier due to a transition state which finally leads to the cyclic amide through a single step [1,2]-H shift process. This result establishes the fact that for these types of pyrroline 1-oxides with unsubstituted-2-position, this type of hydrogen shift is responsible for the lactam formation as similar result was observed for DMPO, as well. Additionally, in this work, we were able to track some additional thermal reaction pathways originating from oxaziridine with high energy barriers. Overall, the study has established the mechanism of the nitrone →oxaziridine→lactam pathway of 3-Me-DMPO system through a comprehensive analysis of its low-lying electronic states.

References

1. F AVillamena, A Das, K M Nash, Potential implication of the chemical properties and bioactivity of nitrone spin traps for therapeutics. *Future Med. Chem.***2012**, 4(9), 1171–1207.
2. G Barriga-González, C Olea-Azar, M C Zuñiga-López, C Folch-Cano, B Aguilera-Venegas, W Porcal, M González, H Cerecetto, Spin Trapping: An Essential Tool for the Study of Diseases Caused by Oxidative Stress. *Current Topics in Medicinal Chemistry***2015**, 15, 484-495.
3. A Gimat, V sneryk, A L Dupont, S Paris, F Averseng, J Fournier, P Massiani, V Rouchon, Investigating the DMPO formate Spin Trapping Method for the Study of Paper Iron Gall Ink Corrosion. *New J. Chem.***2016**, 40, 9098−9110.
4. Y Zhang, D Lu, G Xu, Synthesis and Radical-addition Stereochemistry of Two Trimethyl-I – pyrroline 1 -Oxides as Studied by EPR Spectroscopy. *J. CHEM. SOC. PERKIN TRANS.***1991**, 2, 1855-1860
5. R Bonnett, V M Clark, A S Todd, Experiments Towards the Synthesis of Corrins. Part III. Formation of a Bicyclic Oxaziran from a Δ1-pyroline and From the Corresponding Nitrone. *J. Chem. Soc.***1959,** 0, 2102−2104.
6. L S Kaminsky, M Lamchen, The Photosynthesis of a 2-methyl- 1-pyrroline 1-oxide. *Chem. Commun. (London)***1965**, 0, 130−131.
7. L S Kaminsky, M Lamchen, Nitrones. Part III. Photolysis of Cyclic Nitrones. *J. Chem. Soc. C***1966**, 0, 2295−2299.
8. L S Kaminsky, M Lamchen, Nitrones. Part VI. The Pyrolysis of Oxaziridines Derived by Photolysis of Cyclic Nitrones. *J. Chem. Soc. C***1967**, 0, 2128−2130.
9. S Sen, Y Oruganti, A Chattopadhyay, An Investigation on the Unexplored Photochemistry of 5,5-Dimethyl-1-Pyrroline 1-Oxide (DMPO). *J. Phys. Chem A***2019,** 123, 163.
10. S Sen, A Chattopadhyay, A Computational Study on the Photochemistry of 2,4,4-Trimethyl-1-pyrroline 1-Oxide and Investigation on the Reaction Paths of Its Photoproduct Oxaziridine *ChemistrySelect* , **2019,** 4, 12203.
11. A Migani, M Olivucci, In Conical Intersections: Electronic Structure, Dynamics & Spectroscopy

Advanced Series in Physical Chemistry; Domcke, W., Yarkony, D. R., Koppel, H., Eds.; World Scientific Publishing Co. (P). Ltd.: Singapore, **2004.**

12. A L Sobolewski, W Domcke, In Conical Intersections: Theory Computation and Experiment Advanced Series in Physical Chemistry; Domcke, W., Yarkony, D. R., Koppel, H., Eds.; World Scientific Publishing Co. (P). Ltd.: Singapore, **2011.**
13. S Sen, D S Sisodiya, A Chattopadhyay, The mechanism of photoconversion of cyclic dinitrone to oxaziridine and dioxaziridine: A computational investigation of an experimentally reported photochemical reaction. *J. Phys. Org. Chem.* **2022,** 35, 4, e4310.
14. S Sen, D S Sisodiya, R Nikam, A Chattopadhyay, Revealing the Unexplored Mechanism of Photochemical Oxaziridine Conversion Process of 2H-imidazole 1-oxides. *ChemistrySelect* **2022,** 7, e202202371.
15. M J Frisch, G W Trucks, H B Schlegel, G E Scuseria, M A Robb, J R Cheeseman, G Scalmani, V Barone, B Mennucci, G. A. Petersson et al., Gaussian 09, revision B.01; Gaussian, Inc., Wallingford, CT, **2010.**
16. M W Schmidt, K KBaldridge,J A Boatz,S T Elbert, M S Gordon, J J Jensen, S Koseki, N Matsunaga,K A Nguyen, S Su, et al. General Atomic and Molecular Electronic Structure System. *J. Comput. Chem.***1993,** 14, 1347−1363.
17. H J Werner, P J Knowles, G Knizia, F R Manby, M Schütz, P Celani, T Korona, R Lindh, A Mitrushenkov, G Rauhut, et al. MOLPRO, version 2012.1; A package of ab initio programs: Cardiff, U.K., **2012.**
18. R H AEade, M A Robb, Direct Minimization in MC SCF Theory. The Quasi-Newton Method. *Chem. Phys. Lett.***1981,** 83,362−368.
19. H B Schlegel, M A Robb, MC SCF Gradient Optimization of the H2CO→H2 + CO Transition Structure. *Chem. Phys. Lett.***1982,** 93, 43−46.
20. F Bernardi, A Bottoni, J J W McDouall, M A Robb, H B Schlegel, MCSCF Gradient Calculation of Transition Structures in Organic Reactions. *Faraday Symp. Chem. Soc.* **1984**, 19, 137−147.
21. M J Frisch, I N Ragazos, M A Robb, H B Schlegel, An Evaluation of Three Direct MC-SCF Procedures. *Chem. Phys. Lett.***1992,** 189, 524−528.
22. N Yamamoto,TVreven, M A Robb, M J Frisch, H B Schlegel, A Direct Derivative MC-SCF Procedure. *Chem. Phys. Lett.***1996,** 250, 373−378.
23. L Seunghoon , M Filatov, S Lee, C H Choi, *J. Chem. Phys.***2018,** 149, 104101.
24. L Seunghoon , E E Kim, H Nakata, S Lee, C H Choi, *J. Chem. Phys.***2019,** 150, 184111.
25. Y S Baek, S Lee, M Filatov, C H Choi, *J. Phys. Chem. A***2021,** 125, 1994−2006.
26. D Casanova, A I Krylov, *Phys.Chem.Chem.Phys.***2020,** 22, 4326.
27. C R Kemnitz, G B Ellison, W L Karney, W T Borden, CASSCF and CASPT2 Ab Initio Electronic Structure Calculations Find Singlet Methylnitreneis an Energy Minimum. *J. Am. Chem. Soc.* **2000,** 122, 1098−1101.
28. M X Song, Z X Zhao, F Q Bai, Y J Liu, H X Zhang, C C Sun, CASSCF/CASPT2 Calculation of the Low-Lying Electronic States of the CH3Se Neutral Radical and Its Cation. *J. Phys. Chem. A***2010,** 114, 7173−7178.
29. T Shiozaki, C Woywod, H J Werner, Pyrazine Excited States Revisited using the Extended Multi-State Complete Active Space Second-order Perturbation Method. *Phys. Chem. Chem. Phys.***2013,** 15, 262−269.
30. F Weinhold, Calculation of Upper and Lower Bounds to Oscillator Strengths. *J. Chem. Phys.***1971,** 54, 1874−1180.
31. C W Bauschlicher, S R Langhoff, Computation of Electronic Transition Moments: The Length versus The Velocity Representation. *Theor. Chim. Act.***1991,** 79, 93−103.
32. B Brooks,H F Schaefer,The Graphical Unitary Group Approach to the Electron Correlation Problem. Methods and Preliminary Applications. *J. Chem. Phys.***1979,** 70, 5092−5106.
33. B Brooks, W Laidig, P Saxe, N Handy, H F Schaefer, The Loop-Driven Graphical Unitary Group Approach: A Powerful Method for the Variational Description of Electron Correlation. *Phys. Scr.* **1980,** 21, 312−322.
34. A Chattopadhyay, Spectroscopic Properties of the Low-lying Electronic States of RbHen (n = 1, 2) and their Comparison with Lighter Alkali Metal-helium Systems. *J. Phys. B: At., Mol. Opt. Phys.***2012,** 45, 035101.
35. A Chattopadhyay, Comparative Study of Spectroscopic Properties of the Low-lying Electronic States of 2, 4-Pentadien-1-iminiumCation and Its N-Substituted Analogues. *J. Chem. Sci.***2012,** 124, 985−994.
36. X Li, M J Frisch, Energy-Represented Direct Inversion in the Iterative Subspace within a Hybrid Geometry Optimization Method. *J. Chem. Theory Comput.***2006,** 2, 835−839.
37. U C Singh, P A Kollman, An Approach to Computing Electrostatic Charges for Molecules. *J. Comput. Chem.***1984,** 5, 129− 145.
38. B H Besler, K M Merz, P A Kollman, Atomic Charges Derived from Semiempirical Methods. *J. Comput. Chem.***1990,** 11, 431−439.

About the authors

Dr. Sindhuja Sen *received her Ph.D. degree from BITS-Pilani in the year 2021. She worked under the supervision of Prof. Anjan Chattopadhyay at the department of chemistry, BITS-Pilani, K.K.Birla Goa Campus. Her Ph.D. work was primarily on the computational investigations on cyclic nitrone photochemistry. She did her Bachelor's in Physics from Utkal University, Odishaand Master's degree in Physics from FM University, Odisha.*

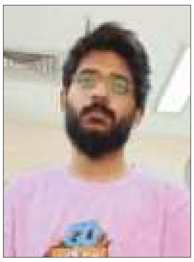

Mr. Dilawar Singh Sisodiya *is currently working as a Ph.D. scholar at BITS-Pilani, K.K.Birla Goa Campus in the department of Chemistry under the supervision of Prof. Anjan Chattopadhyay. Previously, he has worked as a JRF and SRF in a BRNS-sponsored project in the same computational lab. His work is primarily related to the computational investigations on the crown ethers. He did his Bachelor's and Master's degrees in Chemistry from MSU of Baroda.*

Prof. Anjan Chattopadhyay *is working as a Professor at BITS-Pilani, K. K. Birla Goa Campus in the department of Chemistry. He joined BITS-Pilani Goa campus in the year 2005. His Ph.D. is from Jadavpur University, Kolkata and he received his Bachelor's and Master's degrees from Calcutta University. He was the recipient of Prof. Sadhan Basu Memorial award from Calcutta University. He also received Cunningham Memorial award, Sir Upendra Nath Bramachary Memorial award and Sandip Shome Memorial award from Presidency College, Kolkata. His area of research expertise is theoretical & computational chemistry. His major area of research interest lies in exploring the reaction mechanisms of organic and inorganic systems. His research group is actively involved in studies related to computational organic photochemistry. As a visiting researcher, he was associated with the Theoretical Chemistry Group of Prof. Dr. Horst Köppel, Institute of Physical Chemistry, University of Heidelberg, Germany and had research collaborations with his group on photodynamics of polyenes.*

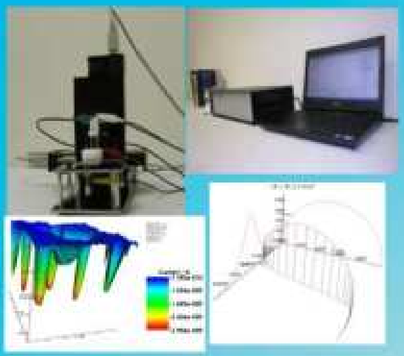


RUBOLAB
RUBOLAB


NIRQuest
OCEAN HDX
OCEAN SR
HR4Pro
Maya 2000Pro

meso-functionalized Porphyrins as efficient catalysts for Photo-oxidation Reactions

Anu Janaagal[a], Vijayalakshmi Pandey[b] and Iti Gupta[a,*]
[a]*Indian Institute of Technology Gandhinagar, Palaj Campus, Gandhinagar, Gujarat-382355, India.*
[b]*St. Xavier's College (Autonomous), Ahmedabad – 380009, India*
**Email: iti@iitgn.ac.in*

Abstract

meso-functionalized porphyrins having two different aryl groups have been synthesized. The aryl groups used were *N*-butylcarbazole, pentaflourophenyl, and *p*-cyanophenyl at their *meso*-positions. Pd(II) complexes of these *meso*-substituted porphyrins were synthesized and used as photocatalysts for the oxidation of aromatic aldehydes. Pd(II)porphyrins showed good phosphorescence, and when exposed to light, they produced singlet oxygen. The singlet oxygen generation efficiency of these porphyrins was measured and found significant. The use of Pd(II)porphyrins under visible light and sunlight as photocatalysts in the presence of oxygento oxidize aromatic aldehydes with high efficiency is demonstrated.

1. Introduction

Various living things include porphyrin as metal complexes, which are necessary for life. [1]. The metalloporphyrins are present in hemoglobin, chlorophyll, and cytochrome 450, demonstrating different functions like oxygen transport, photosynthesis, and electron transport[2]. The prosthetic groups, which include iron, magnesium, and cobalt, determine their roles, which range from oxygen transport to electron transfer. Artificial porphyrins and their derivatives have been synthesized and found in extensive practice in various fields, including biomedicine, materials science, catalysis, and supramolecular chemistry [3-6]. One method to enhance the porphyrin's photophysical properties and use them in different applications is to insert various metals into the molecule's center. Metalloporphyrins are best suited for oxidation reactions such as hydroxylation, epoxidation, carbonylation, sulfoxidation, etc., of organic substrates [7]. Porphyrin complexes of ruthenium, iron, and manganese are efficient catalysts for C-H oxidation and epoxidation of alkenes with

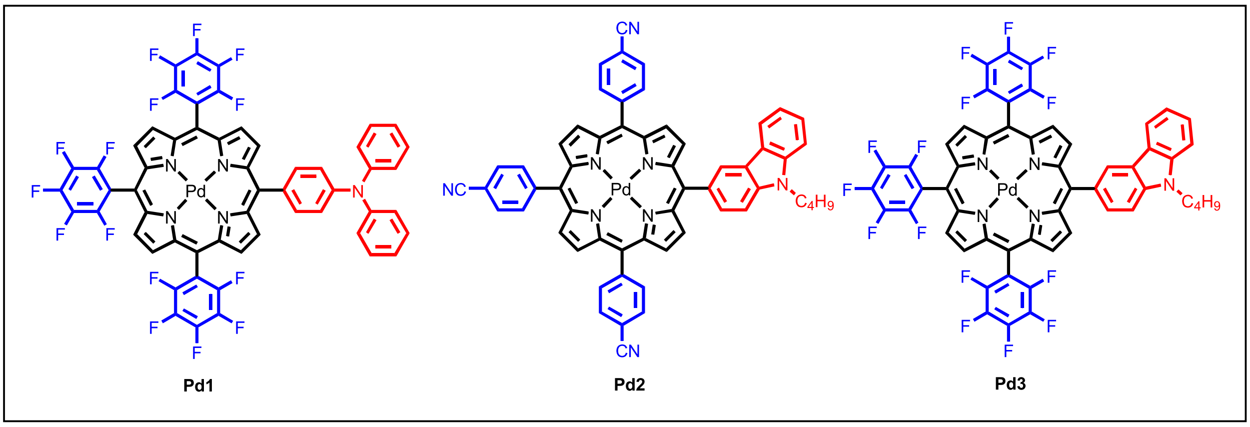

Chart 1: *Structure of meso-functionalized porphyrins (**Pd1-Pd3**).*

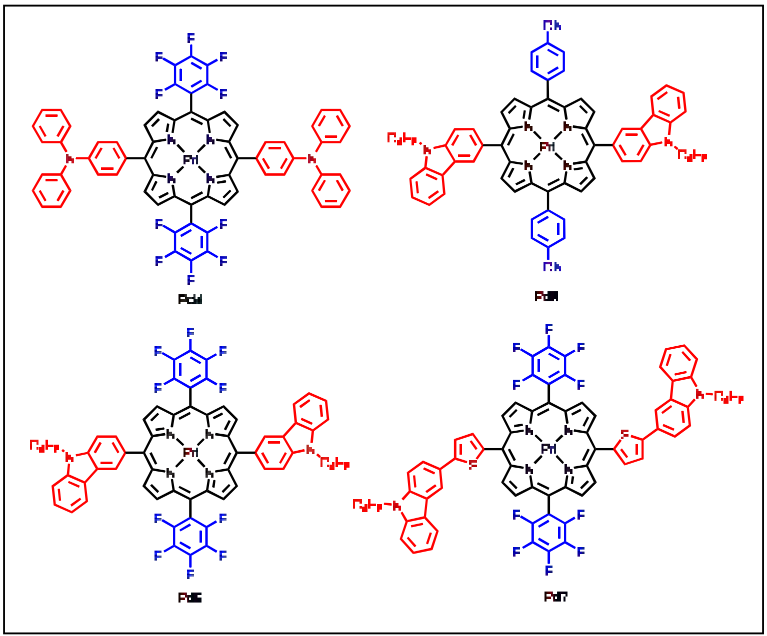

Chart 2:*Structure of meso-functionalized porphyrins* ***(Pd4-Pd7)****.*

remarkable selectivity and good product yields [8]. Similarly for the large-scale, biologically inspired oxidation of cyclohexane to cyclohexanone, cobalt(II) porphyrin is employed [9].

Because of the spin rule, molecular oxygen cannot compete with organic molecules; hence oxidation using molecular oxygen remains a problem. Due to the high absorption coefficient, robust photostability, and triplet excited states, porphyrin derivatives are notable photosensitizers in this regard. In the presence of free-base porphyrins or metalloporphyrins, which are effective photosensitizers for the generation of singlet oxygen and selective oxidations with oxygen can be achieved. Heavy metals containing metalloporphyrins can produce singlet oxygen with the Type II mechanism. The photo-oxidation of aromatic and aliphatic aldehydes with various *meso*-aryl-modified Pt(II) porphyrins was reported by N. Safari and coworkers [10]. For these photocatalytic reactions, the TON (turnover number) ranged from 210 to 970 [10]. *Meso*-aryl groups at the *meso*-position and the central metal ion used, can significantly affect the catalytic activity of porphyrin macrocycles [11]. These groups can also have a good effect on catalytic photo-oxidation. Careful design of such systems can enhance electronic communication and donor-acceptor (D-A) interactions. Because of their strong absorption and commendable quantum yields, energy donors in dyads such as BODIPYs, Aza-BODIPYs, and corroles; carbazoles have been used. [12-16]. The covalently connected thiophene rings are proficient moiety to establish electronic contact between the donor and acceptor [17]. Since porphyrins do not absorb in the 200-400 nm, where the absorption band of carbazole emerges. The careful excitation of the carbazole as donor group can be accomplished in D-A systems. As reported in previous work, these donor-acceptors have proven to be promising photocatalysts [17].

Here in we discuss the *meso*-functionalized carbazole appended A_2B_2 and A_3B porphyrins synthesized in our lab [17-20]. The discussion includes their DFT, efficiency for catalytic activity along with singlet oxygen generation.

2. Results and Discussion

In the previous work, we have systematically provided the synthetic methodology for producing porphyrins without metals and with Pd(II) at metal center [17-22]. The A_3B type (three *meso*-aryl groups are same and one is different) and A_2B_2 (two *meso*-aryl groups are different) type porphyrins are shown in charts 1 and 2, respectively.

Photophysical studies

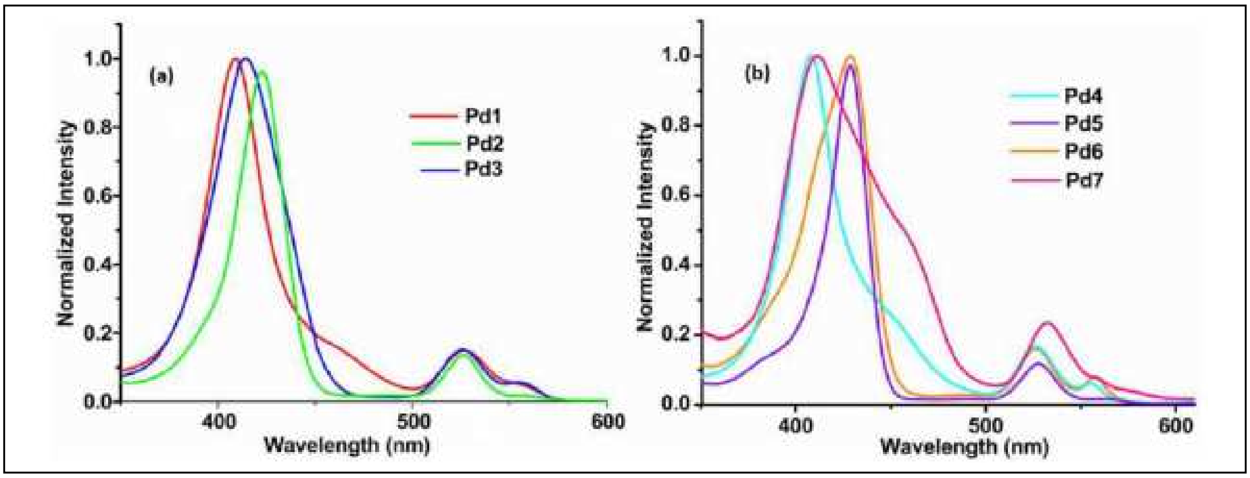

Figure 1: *Normalized absorption spectra for **Pd1- Pd7**in toluene.*

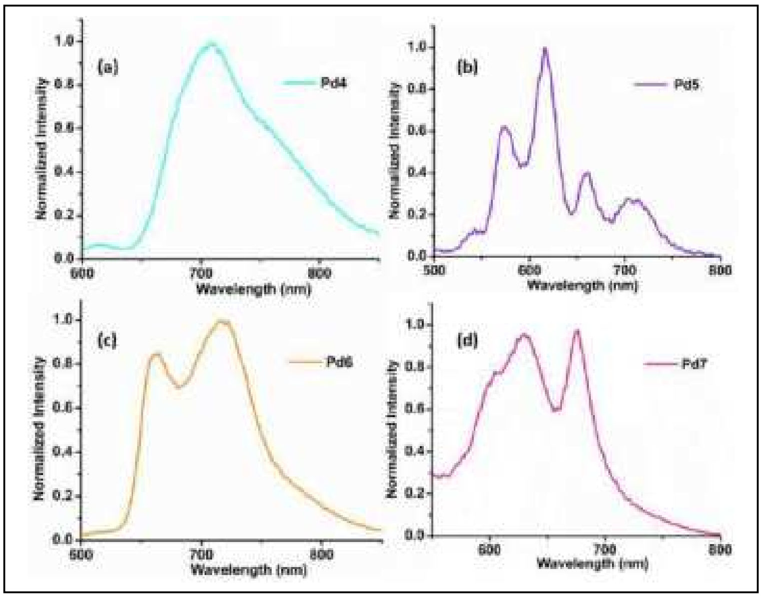

Figure 2: *Normalized emission spectra of **Pd4-Pd7**.*

All the palladium porphyrins showed similar characteristics to the reported palladium porphyrins during the UV-Vis absorption analysis (Figs.1a and 1b) [23]. These palladium porphyrins **Pd1–Pd7** displayed classic absorption peaks in between 408–428 nm. As shown in Table 1, Pd(II) porphyrins displayed a Soret band tailed by two Q-bands between 525–557 nm with significant red shifts. Interestingly, all of the porphyrins exhibited a little widening of the Soret band, pointing to a possible communication concerning the carbazole as *meso*-donor groups and the porphyrin core. However, the broadening in **Pd7** was comparatively more in the (thiophene linked *N*-butylcarbazole). The wider Soret band of **Pd7** with the addition of thiophene indicated boosted electronic interactions between the donor and acceptor units; the reason can be vibronic coupling, as noted in the literature. For the $S_0 \rightarrow S_2$transitions, the epsilon values were between 409,000 to 114,000 $M^{-1}cm^{-1}$ and for the first Q band the values were close to 5,000 $M^{-1}cm^{-1}$. The existence of *N*-butylcarbazole and thiophene linked *N*-butylcarbazole may be responsible for bathochromic shifts of the Q bands in porphyrins **Pd1**–**Pd7**, these moieties are known to improve electronic communication in such D-A systems.

There are potential uses of the phosphorescent palladium (II) porphyrins in biology and materials. At ambient temperature, toluene was used to record the phosphorescence spectra of the metalloporphyrins **Pd1-Pd7**. Figure 2 displays the reasonable emission spectra of the selected porphyrins **Pd4-Pd7**. The porphyrins **Pd4–Pd7** have emission configurations

Table 1: *Photophysical data recorded in toluene for porphyrins **Pd1-Pd7**.*

Porphyrin	λ_{abs}(nm)	λ_{ex}(nm)	λ_{em}(nm)
Pd1	410, 528, 559	413	559, 611, 680
Pd2	423, 527, 556	425	571, 615, 654
Pd3	413, 526, 559	413	561, 613, 665
Pd4	408, 527, 557	408	707
Pd5	429, 526, 564	425	574, 616, 657
Pd6	428, 526, 557	428	664, 717
Pd7	41, 533, 559	413	621, 666

comparable to that of the parent porphyrin PdTPP, with a typical emission pattern in the 559–717 nm range. However, emission spectra for **Pd5** showed multiple peaks indicating a combined effect of fluorescence, as well as phosphorescence, But in the case of **Pd4** one single phosphorescent peak was observed in deoxygenated toluene indicating phosphorescence is dominant as shown in Fig.2. This can be due to the Pd(II) porphyrins' quick singlet-triplet intersystem crossing; there was very little fluorescence visible in these spectra. All the porphyrins (**Pd1**-**Pd7**) displayed an effective phosphorescence as a consequence of spin-orbit coupling caused by palladium that encourages radiative falling-off from the triplet state (T_1). For reference, selected photophysical data have been provided in Table 1.

DFT Studies

Computational studies were conducted to comprehend the geometrical parameters and electronic cloud in various HOMO and LUMO states of **Pd1-Pd7** molecules. B3LYP/6-311+(d) calculation was employed to augment palladium complexes with pseudo potential [24]. TD-DFT studies were done to find out additional details about the light-absorbing properties, and gain computational insight to support significant transitions [25]. A detailed observation of each molecule with its derivatives has been provided in our previous work [17-20]. However, to understand the change in electronic clouds with different moieties, their HOMO-LUMO energy level has been compared, and computational data of selected porphyrins have been shown in Table 2**.** The optimized structures and FMO along with the HOMO and LUMO states for the selected porphyrins have been presented in Figs.**3-6**.

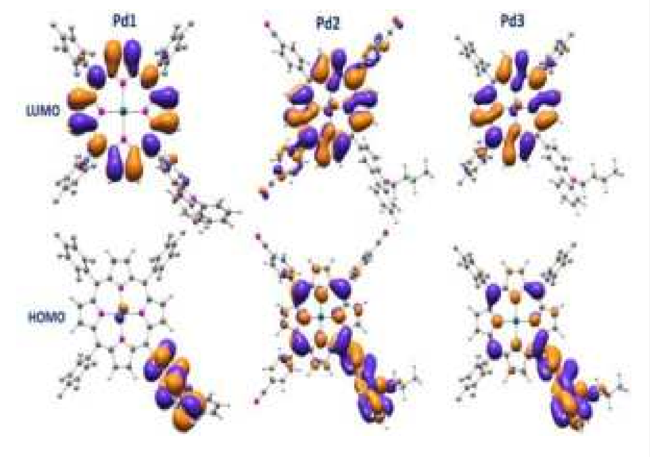

Figure 3: *The frontier MOs (FMOs) of **Pd1**, **Pd2** and **Pd3**.*

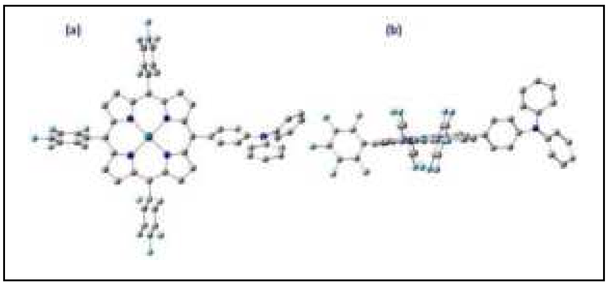

Figure 4: *Optimized structure of porphyrin **Pd1**(a) front view; (b) planar view.*

The studies done for the *meso*-substituted A_2B_2 and A_3B type porphyrins suggested that carbazole and triphenyl appended porphyrins have shown prominent $S_0 \rightarrow S_1$ transitions. The observation also indicated a shift of the electronic cloud from HOMO-3→LUMO+1 in

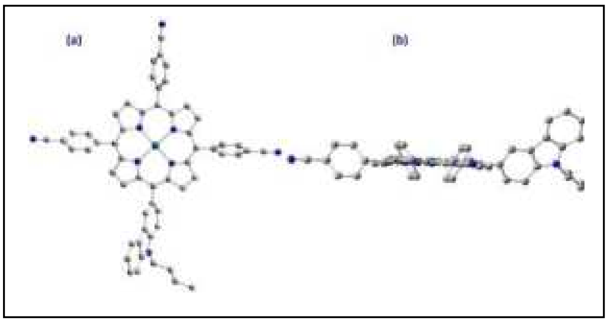

Figure 5: *Optimized structure of porphyrin **Pd2** (a) front view; (b) planar view.*

Pd6 and **Pd7**. However, in **Pd1** the major transition occurs from HOMO-2➔LUMO+1 and for **Pd4** the transitions occur from HOMO-1➔LUMO. The major transition observed for **Pd2** was from HOMO-4➔LUMO+2. The minor discrepancy between theoretical and experimental absorption maxima was also detected for **Pd1-Pd7** suggested that the basis set chosen for these molecules was appropriate. The dihedral angle were also calculated using computational studies. The dihedral angle of the *meso*-triphenylamine group with the porphyrin plane [C47-C45-C20-C18] in **Pd1** porphyrin was estimated to be 66.9°. In **Pd3**, the torsion angles observed were [C46-C45-C20-C21] 66.7° and [C13-C34-C28-C29] 72.2° between the porphyrin plane and *meso*-substituents (*N*-butylcarbazole groups). Effective electronic communication can be concluded from the results obtained.

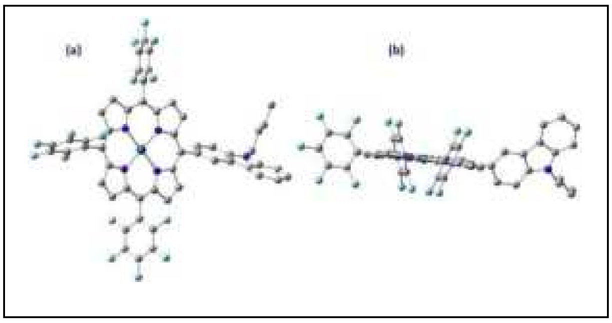

Figure 6:*Optimized structure of porphyrin **Pd3** (a) front view; (b) planar view.*

***Table 2:** Excited state energies and observed theoretical absorption values for Pd(II)porphyrins.*

Porphyrin	Contribution	λ (nm)	Exp. λ (nm) in Toluene
Pd1	HOMO-3➔LUMO HOMO-3➔LUMO+1 HOMO-2➔LUMO HOMO-2➔LUMO+1 HOMO-1➔LUMO HOMO-1➔LUMO+1 HOMO➔LUMO+1	391.38	410
Pd2	HOMO-4➔LUMO+1 HOMO-4➔LUMO+2 HOMO-2➔LUMO+1 HOMO-1➔LUMO HOMO-1➔LUMO+1 HOMO➔LUMO+1	420	429
Pd3	HOMO-6➔LUMO HOMO-5➔LUMO+1 HOMO-4➔LUMO HOMO-4➔LUMO+1 HOMO-3➔LUMO HOMO-3➔LUMO+1 HOMO-2➔LUMO HOMO-1➔LUMO+1	396	415
Pd4	HOMO→LUMO HOMO-1→LUMO HOMO→LUMO+1 HOMO-1→LUMO+1 HOMO-3→LUMO HOMO-3→LUMO+1	568	408
Pd6	HOMO→LUMO HOMO→LUMO+1 HOMO-2→LUMO HOMO-3→LUMO HOMO-3→LUMO+1	528	428
Pd7	HOMO-5➔LUMO+1 HOMO-4➔LUMO HOMO-4➔LUMO+1 HOMO-3➔LUMO+1 HOMO-2➔LUMO	417	411

Singlet oxygen generation and catalysis

In light of the heavy atom effect, metalloporphyrins encompassing 4d along with 5d series metals corresponding platinum and palladium in their core display noticeable inter-system crossing (ISC) [26]. These metalloporphyrins can generate $^1O_2$ by the type II pathway. So, porphyrins with heavy metals at core have been used as catalysts for the photo activated oxidation reactions of organic substrates, because of their capacity to produce singlet oxygen.

Palladium porphyrins (**Pd1-Pd7**) were studied for singlet oxygen generation in acetonitrile saturated with oxygen, to find out the singlet

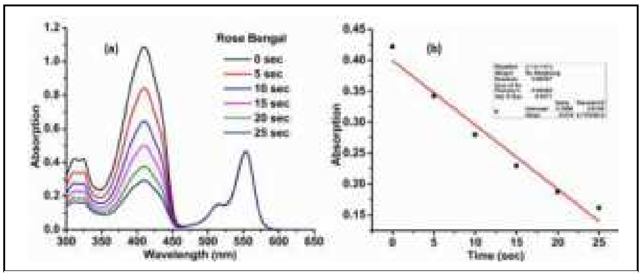

Figure 7: *Absorbance changes: Rose Bengal (RB); light exposure(visible light 15 Jcm^{-2}); rate of decrease of absorbance at 324 nm.*

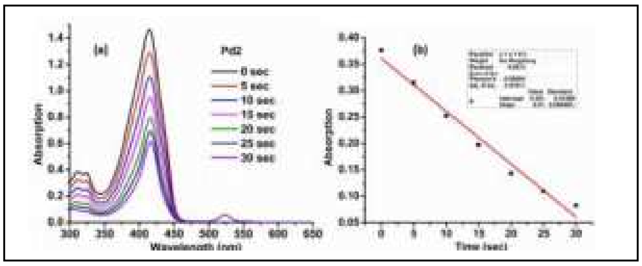

Figure 8: *Absorbance changes of* ***Pd2****; light exposure (visible light = 15 Jcm^{-2}); rate of decrease of absorbance at 324 nm.*

oxygen quantum yields [27-30]. In this solution DPBF was utilized as an oxygen scavenger, and absorption parameters were made to track singlet oxygen formation by Pd(II) porphyrins. **RB** was used as standard substance. The oxygen molecules were stimulated to the singlet state by the energy transfer from photosensitizers **(Pd1-Pd7)** to the triplet ground state, which then reacted with DPBF. Over a period of time**,** a decline in the DPBF absorption band was observed. A visible light source was used to photo-radiate synthesized porphyrins, the **Pd7** showed 68% singlet oxygen quantum yield in acetonitrile. The other porphyrins (**Pd1**, **Pd2**, **Pd3**, and **Pd5**) generated singlet oxygen between 30% to 57%, indicating that these porphyrins can function as efficient photo-oxidation catalysts.

The oxidation of alcohols and aldehydes have been tested with Pt(II) porphyrins with positive results; palladium can be seen as a promising substitute for such reactions, due to its lower cost compared to other metalloporphyrins. White light source was used at room temperature and palladium porphyrins (**Pd1–Pd7**) were employed to carry out the oxidation of aromatic aldehydes in aerated medium. Different electron-rich and electron-deficient aromatic aldehydes were selected for photo-oxidation. As compared to the substrates with electron-donating groups, it was found that substrates with electron-withdrawing groups performed better. The data is based on the reactions carried out and the reaction yields were obtained after purification.Up to 88% of the product yield was obtained using **Pd5** for photooxidation. In the case of tolualdehye and 3-fluorobenzaldehyde, good yields of 62% and 80% were achieved. Using **Pd7** as a photocatalyst, up to 99% of the product yield was obtained under the 24 watts white light source, with turnover number of 16,500. The photooxidation of aryl aldehydes was also achieved under sunlight, and the maximum product yield obtained was 97% with a high turnover (16,100). Compared to **Pd5**, the **Pd7** having pentafluorophenyl and thiophene appended carbazole at *meso* positions, worked better as photocatalysts in visible light and showed promising results with sunlight. According to observations from numerous conducted and reported experiments, **Pd1-Pd7** are promising photocatalysts for reactions carried out in white light and solar light.

3. Conclusion

The *meso*-functionalized A_2B_2 and A_3B type Pd(II)porphyrins were discussed. The porphyrins with palladium as central atom showed substantial phosphorescence and fluorescence peaks. The same porphyrins produced good singlet oxygen generation because of the heavy metal effect. This singlet oxygen was then used to oxidize aromatic aldehydes into carboxylic acids. Pd(II) porphyrins showed considerable catalysis for photo-assisted oxidation processes, as evidenced by the conversion of several aldehydes containing electron donating and withdrawing groups to their corresponding acids in significant yields.

Table 3: *Photo induced oxidation reactions under white light and sunlight by* ***Pd5*** *and* ***Pd7****.*

		(% Yield of acid)		
		Visible light		Sunlight
Aldehyde	Acid	Pd5	Pd7	Pd7
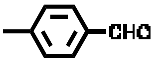	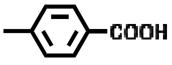	62	97	97
		38	99	60
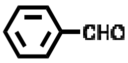	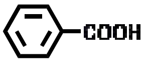	68	97	96
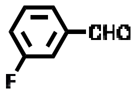	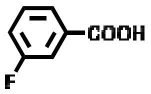	60	75	72

References

1. Poalesse R. The Porphyrin Handbook, vol. 2. In: Kadish KM, Smith KM, Guilard R, Academic Press, New York, 2000.
2. Erben C, Will S, Kadish KM. The Porphyrin Handbook, vol 2. In: Kadish KM, Smith KM, Guilard R, editors. Academic Press, New York, 2000.
3. Ethirajan M, Chen Y, Joshi P, Pandey RK. The role of porphyrin chemistry in tumor imaging and photodynamic therapy. Chemical Society Reviews. 2011;40(1):340-62.
4. Das S, Gupta I. Synthetic aspects of carbazole containing porphyrins and porphyrinoids. Journal of Porphyrins and Phthalocyanines. 2019;3:459-501.
5. Beletskaya I, Tyurin VS, Tsivadze AY, Guilard R, Stern C. Supramolecular chemistry of metalloporphyrins. Chemical Reviews. 2009;109(5):1659-713.
6. Higashino T, Imahori H. Porphyrins as excellent dyes for dye-sensitized solar cells: recent developments and insights. Dalton Transactions. 2015;44(2):448-63.
7. Barona-Castaño JC, Carmona-Vargas CC, Brocksom TJ, De Oliveira KT. Porphyrins as catalysts in scalable organic reactions. Molecules. 2016;21(3):310.
8. Costas M. Selective C–H oxidation catalyzed by metalloporphyrins. Coordination Chemistry Reviews. 2011;255(23-24):2912-32.
9. Guo CC, Liu XQ, Liu Q, Liu Y, Chu MF, Lin WY. First industrial-scale biomimetic oxidation of hydrocarbon with air over metalloporphyrins as cytochrome P-450 monooxygenase model and its mechanistic studies. Journal of Porphyrins and Phthalocyanines. 2009;13(12):1250-4.
10. Hajimohammadi M, Safari N, Mofakham H, Shaabani A. A new and efficient aerobic oxidation of aldehydes to carboxylic acids with singlet oxygen in the presence of porphyrin sensitizers and visible light. Tetrahedron Letters. 2010;51(31):4061-5.
11. Hajimohammadi M, Safari N. Photooxygenation of alkenes by molecular oxygen in the presence of porphyrins and chlorin sensitizers under visible light irradiation. Journal of Porphyrins and Phthalocyanines. 2010;14(07):639-45.
12. Gupta I, Kesavan PE. Carbazole Substituted BODIPYs. Frontiers in chemistry. 2019 ;7:841.
13. Kesavan PE, Behera RN, Mori S, Gupta I. Carbazole substituted BODIPYs: synthesis, computational, electrochemical and DSSC studies. Journal of Fluorescence. 2017;27(6):2131-44.
14. Balsukuri N, Gupta I. Singlet-singlet energy transfer in carbazole-porphyrin dyads and triads. Dyes and Pigments. 2017;144:223-33.
15. Balsukuri N, Das S, Gupta I. Carbazole–corrole and carbazole–prophyrin dyads: synthesis, fluorescence and electrochemical studies. New Journal of Chemistry. 2015;39(1):482-91.
16. Kesavan PE, Gupta I. Carbazole substituted boron dipyrromethenes. Dalton Transactions. 2014;43(32):12405-13.
17. Pandey V, Janaagal A, Jain A, Mori S, Gupta I. A_2B_2 type porphyrins with *meso*-donor groups: Synthesis, X-ray structures, DFT studies and photocatalytic application using sunlight. Dyes and Pigments. 2022;209:110861.

18. Das S, Bhat HR, Balsukuri N, Jha PC, Hisamune Y, Ishida M, Furuta H, Mori S, Gupta I. Donor–acceptor type A 2 B 2 porphyrins: synthesis, energy transfer, computational and electrochemical studies. Inorganic Chemistry Frontiers. 2017;4(4):618-38.
19. Pandey V, Jain D, Pareek N, Gupta I. Pd (II) porphyrins: Synthesis, singlet oxygen generation and photoassisted oxidation of aldehydes to carboxilic acids. InorganicaChimicaActa. 2020;502:119339.
20. Janaagal A, Pandey V, Sabharwal S, Gupta I. *meso*-Carbazole substituted palladium porphyrins: Efficient catalysts for visible light induced oxidation of aldehydes. Journal of Porphyrins and Phthalocyanines. 2021;25(05n06):571-81.
21. Lindsey JS. Synthetic routes to *meso*-patterned porphyrins. Accounts of chemical research. 2010;43(2):300-11.
22. Kesavan PE, Pandey V, Ishida M, Furuta H, Mori S, Gupta I. Synthesis, photophysical properties and computational studies of beta□substituted porphyrin dyads. Chemistry–An Asian Journal. 2020;15(13):2015-28.
23. Darwent JR, Douglas P, Harriman A, Porter G, Richoux MC. Metal phthalocyanines and porphyrins as photosensitizers for reduction of water to hydrogen. Coord. Chem. Rev.;(Netherlands). 1982;44(1).
24. 24 Wadt WR, Hay PJ. Ab initio effective core potentials for molecular calculations. Potentials for main group elements Na to Bi. The Journal of chemical physics. 1985 Jan 1;82(1):284-98.
25. Lee C, Yang W, Parr RG. Development of the Colle-Salvetti correlation-energy formula into a functional of the electron density. Physical review B. 1988;37(2):785.
26. Pandey V, Raza MK, Joshi P, Gupta I. Synthesis of Water-Soluble Thioglycosylated trans-A2B2 Type Porphyrins: Cellular Uptake Studies and Photodynamic Efficiency. The Journal of Organic Chemistry. 2020;85(10):6309-22.
27. Pushpanandan P, Maurya YK, Omagari T, Hirosawa R, Ishida M, Mori S, Yasutake Y, Fukatsu S, Mack J, Nyokong T, Furuta H. Singly and Doubly N-Confused Calix [4] phyrin Organoplatinum (II) Complexes as Near-IR Triplet Sensitizers. Inorganic chemistry. 2017;56(20):12572-80.
28. Manav N, Singh R, Janaagal A, Yadav AK, Pandey V, Gupta I. Synthesis, computational and optical studies of tetraphenylethene-linked Pd (II) dipyrrinato complexes. New Journal of Chemistry. 2022;46(40):19310-21.
29. Manav N, Kesavan PE, Ishida M, Mori S, Yasutake Y, Fukatsu S, Furuta H, Gupta I. Phosphorescent rhenium-dipyrrinates: efficient photosensitizers for singlet oxygen generation. Dalton Transactions. 2019;48(7):2467-78.
30. Manav N, Lone MY, Raza MK, Chavda J, Mori S, Gupta I. Luminescent iridium (III) dipyrrinato complexes: synthesis, X-ray structures, and DFT and photocytotoxicity studies of glycosylated derivatives. Dalton Transactions. 2022;51(10):3849-63.

About the authors

Dr. Iti Gupta *is currently working as an Associate Professor at IIT Gandhinagar. She obtained Ph.D. in Chemistry from IIT Bombay, India. She received JSPS-fellowship from Japan and did postdoctoral research at Kyushu University, Fukuoka where she worked on expanded porphyrins. Later she joined BITS-Pilani KK Birla Goa campus as faculty in Chemistry (2007-2009). She Joined IIT Gandhinagar as Assistant Professor in July 2009. Her recent research interest involves synthesis and computational studies of various "Synthetic Pigments" like porphyrins, corroles, BODIPYs, and metal-dipyrrinates. The Porphyrin and BODIPY derivatives are promising candidates for bioimaging, chemosensing, ROS generation, and photodynamic therapy (PDT). She has authored/co-authored more than 54 research papers in refereed international /national journals (H-index 22). She is a member of the Society of Porphyrins & Phthalocyanines (France, 2012-till date); also a life member of the Indian Chemical Society of India (2021 onwards). She is an Associate Editor in Photocatalysis and Photochemistry (specialty section of Frontiers in Chemistry).*

Dr. Vijayalakshmi Pandey *is an Assistant Professor at St. Xavier's College Ahmedabad. She received her Ph.D. degree from IIT Gandhinagar in 2021. She worked under the supervision of Dr. Iti Gupta. Her Ph.D. work was based on synthesis and characterization of* A_2B_2 *type porphyrins for photodynamic theory, photooxidation reactions, and the energy transfer process. She did her Master's degree from the School of Chemical Sciences, Devi Ahilya University, Indore, Madhya Pradesh.*

Ms. Anu Janaagal *is a Ph.D. scholar in the Chemistry Discipline at IIT Gandhinagar. She obtained her Master's degree in Chemistry from IIT Ropar in 2018. She is currently pursuing her Ph.D. research on synthesis different meso-substituted porphyrins and their photocatalytic applications.*

Synthesis, and characterization of blue-emitting C-dots for sensing hyaluronic acid (HA) and hyaluronidase (HAase).

Shivanand H Nannuri[a], Abhijeet Pandey[b], Srinivas Mutalik[b] and Sajan D. George[a]*
[a]Centre for Applied Nanosciences, Department of Atomic and Molecular Physics, Manipal Academy of Higher Education, Manipal 576104, Karnataka State, India
[b]Department of Pharmaceutics, Manipal College of Pharmaceutical Sciences, Manipal Academy of Higher Education, Manipal 576104, Karnataka State, India
**Email: sajan.george@manipal.edu*

Abstract

Carbon dots (C-dots) is an emerging class of nanodots that are highly biocompatible and water dispersible. In general, these particles are highly fluorescing and can be synthesized from naturally occurring materials via microwave or solvothermal techniques. In this work, we present the results of the synthesis and characterization of the C-dots using citric acid as a carbon source and ethylenediamine as a nitrogen source. A microwave synthesis route has been adopted to prepare water-dispersible carbon dots at 180°C for 10 minutes. The as-prepared C-dots are characterized using UV–Vis absorption spectroscopy, photoluminescence, XRD, Fourier transform infrared spectroscopy, XPS, and ζ-potential measurements. Further, a label-free assay for monitoring hyaluronic acid (HA) and hyaluronidase (HAase) levels is designed by utilizing C-dot fluorescence as a probe. The addition of HA is quantified in terms of fluorescence quenching of C-dots that occurs as a result of electrostatic adsorption of HA onto the C-dots' surface. In contrast, HA was decomposed from the C-dots surfaces by the further addition of HAase, and fluorescence recovery is observed which is used to quantify HAase. The results of the present study illustrate that the C-dots can be employed as an OFF-ON optical probe with great sensitivity and selectivity for the detection of HA and HAase.

1. Introduction

The ultra-small carbon nanodots (C-dots), the latest form of carbon nanomaterial, are now emerging as a favorable material for many applications in various fields including photonics and bio-sensing [1, 2]. Specifically, their good biocompatibility has led to their successful use in the imaging of living cells and in drug delivery as the small sizes (usually having a diameter less than 10 nm) of particles facilitate easy diffusion into the cells. The facile synthesis of C-dots approaches often relies on naturally occurring materials via various synthesis approaches including microwave or solvothermal techniques [1]. Most of the reported carbon dots comprise carbon atoms with considerable fractions of hydrogen, oxygen, and a trace amount of nitrogen and surface functional groups (e.g., carbonyl, carboxyl, hydroxyl, and amine groups) [3-5]. The low-cost synthesis, biocompatibility, tunable emission properties, chemical inertness, high photostability, good intracellular solubility, and environmentally sensitive emission characteristics of C-dots, make them a promising material for fabricating fluorescence-based optical sensors, particularly for bio applications [6-8].

Being a major constituent of the extracellular matrix, hyaluronic acid (HA) controls cell adhesion, migration, and proliferation, also different functions of tumors are reported to be closely linked with HA and it is mainly made up of repeating d-glucuronic acid and N-acetyl-d-glucosamine [9]. On the other hand, the hyaluronidase (HAase) enzyme specifically degrades the hyaluronic acid by splitting the internal β-N-acetyl-D-glucosamine linkages. In addition, the literature suggests that HAase is considered as one of the cancer markers due to the over-secretion of HAase in cancer patients in different types of cancer including bladder, colon, and prostate. Thus, it is important to detect HA and HAase selectively with improved sensitivity [10].

In this work, we present the results of the synthesis and characterization of the nitrogen-doped C-dots using citric acid as a carbon source and ethylenediamine as a nitrogen source. A microwave synthesis route has been adopted to prepare water-dispersible C-dots at 180°C for 10 minutes. The as-prepared C-dots are characterized using UV–Vis, photoluminescence, XRD, Fourier transform infrared spectroscopy, XPS, TEM, ζ-potential techniques, from which their structural information, as well as other properties, are interpreted. In addition, the excitations wavelength-dependent, as well as pH-dependent emission properties of the samples are investigated. Further, selective sensing for HA and HAase using these particles was also demonstrated.

2. Materials &Methods

2.1 Materials

Citric acid monohydrate (CA) and Ethylenediamine (EDA), $HgCl_2$, $NaAsO_2$, $Pb(NO_3)_2$, $CdCl_2$, $MnCl_2.4H_2O$, $CrCl_3.6H_2O$, $Mg(NO_3)_2.6H_2O$, $FeCl_3$, and $CoSO_4.7H_2O$ were purchased from Merck India. All reagents were analytical and were used without further purification. All solutions were prepared with deionized water from a Millipore MilliQ

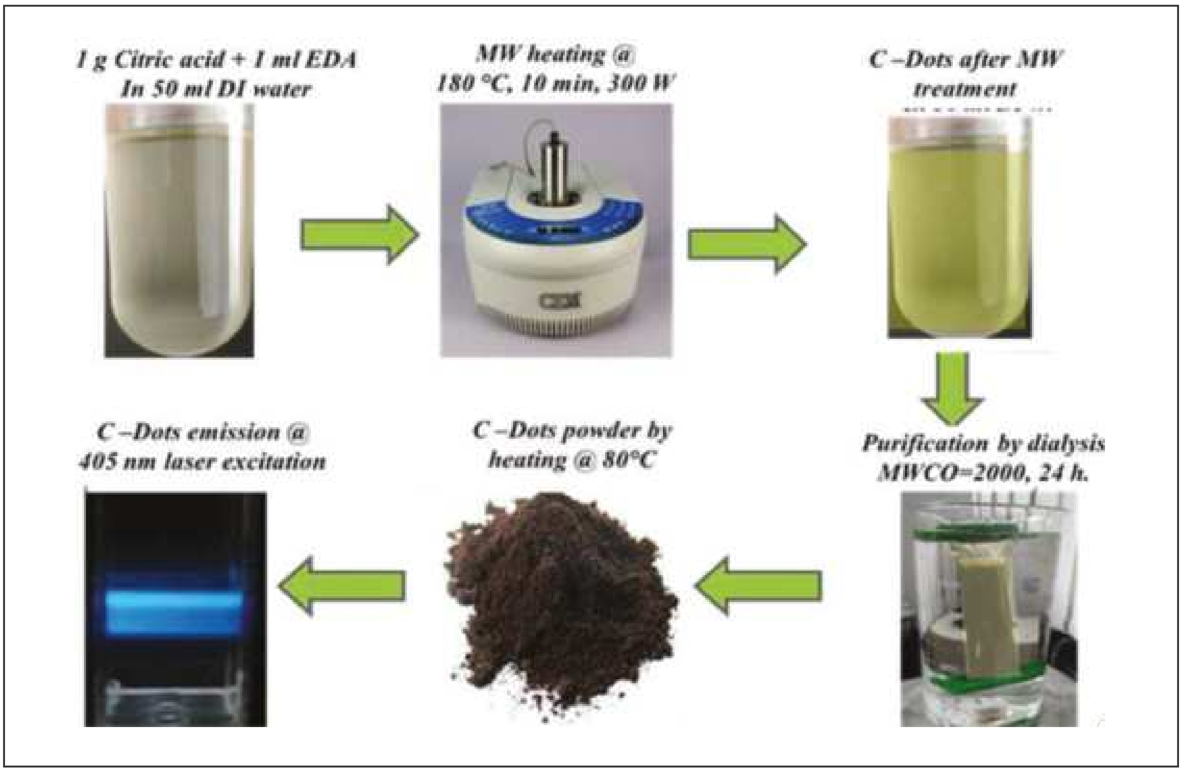

Figure1: *Schematic of the synthesis steps of C-dots by microwave method*

system with a resistivity of 18.2 MΩ·cm.

2.2 Synthesis of blue-emitting C-dots via microwave-assisted and hydrothermal methods:

The blue-emitting C-dots were prepared based on the literature with some modifications [11]. In this work, nitrogen-doped carbon dots were prepared via microwave-assisted synthesis using the CEM Discover SP Microwave synthesizer method as shown schematically in Figure1. In a typical procedure citric acid (1 g) and 1 ml of EDA were dissolved in 50 ml DI water. The solution was then transferred into a microwave vial and heated at a temperature of 180 °C for 10 min at 300 W power. After the reaction was over, the reactor was allowed to cool to room temperature naturally. The carbon dots solution was dialyzed with a dialysis bag (MWCO≈2000 Da) for 24 hours. Finally, black powder C-Dots were obtained by drying at 80°C.

3. Results & Discussion

3.1 Characterization of C-dots:

The XRD pattern of C-dots given in Figure. 2 (a) illustrate broad diffraction peaks centered at 2θ =23.5° and 41.1°, which can be attributed to the disordered carbon atoms with a high degree of (002) and (100) planes of the hexagonal graphite structure. The d-spacing is calculated by using Bragg's equation ($d= n\lambda/2 \sin\theta$) and the values are found to be approximately 3.78 Å and 2.19 Å for the (002) and (100) peaks, respectively [12]. The surface functional groups of the C-dots are detected by FTIR studies. The recorded FTIR spectra are shown in Figure 2 (b) illustrating the characteristic bands of O–H around 3366 cm^{-1}, and the stretching vibration bond of N−H around 3073 cm^{-1}. Moreover, the two peaks observed around 1653 and 1558 cm^{-1}correspond to the C = O bond and N−H bond [11].The ζ-potential value for the C-dots in the aqueous solution is measured using Horiba instruments (SZ-100). The obtained values are +27.4 mV indicating the electrostatic stabilization of the C-dots in an

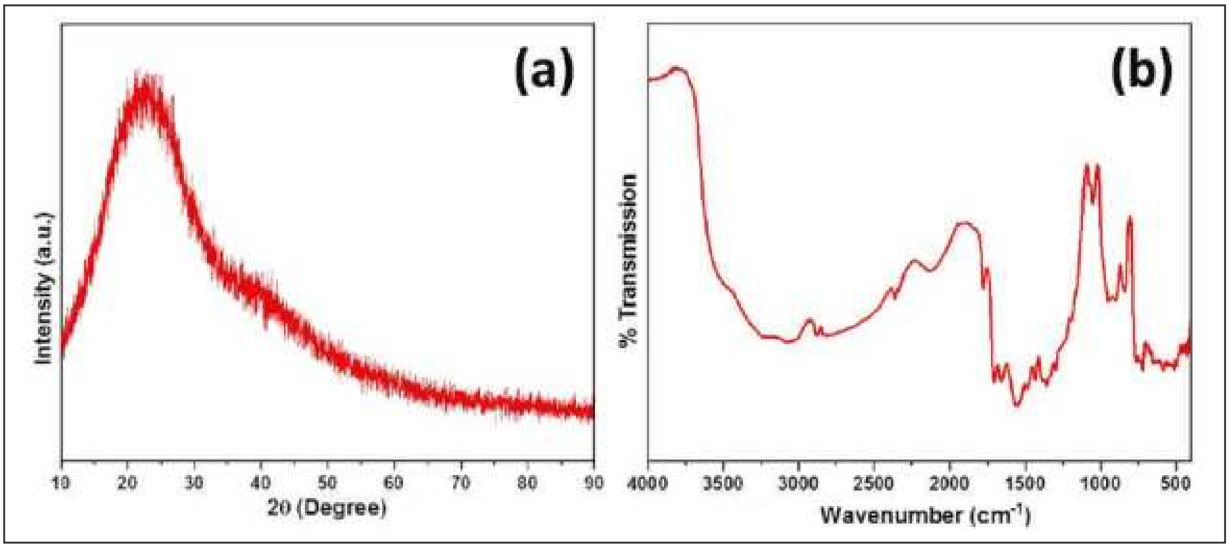

Figure 2:*(a) The XRD profile of the blue-emitting C-dots. (b) FT-IR spectrum blue-emitting C-dots.*

aqueous solution [13].

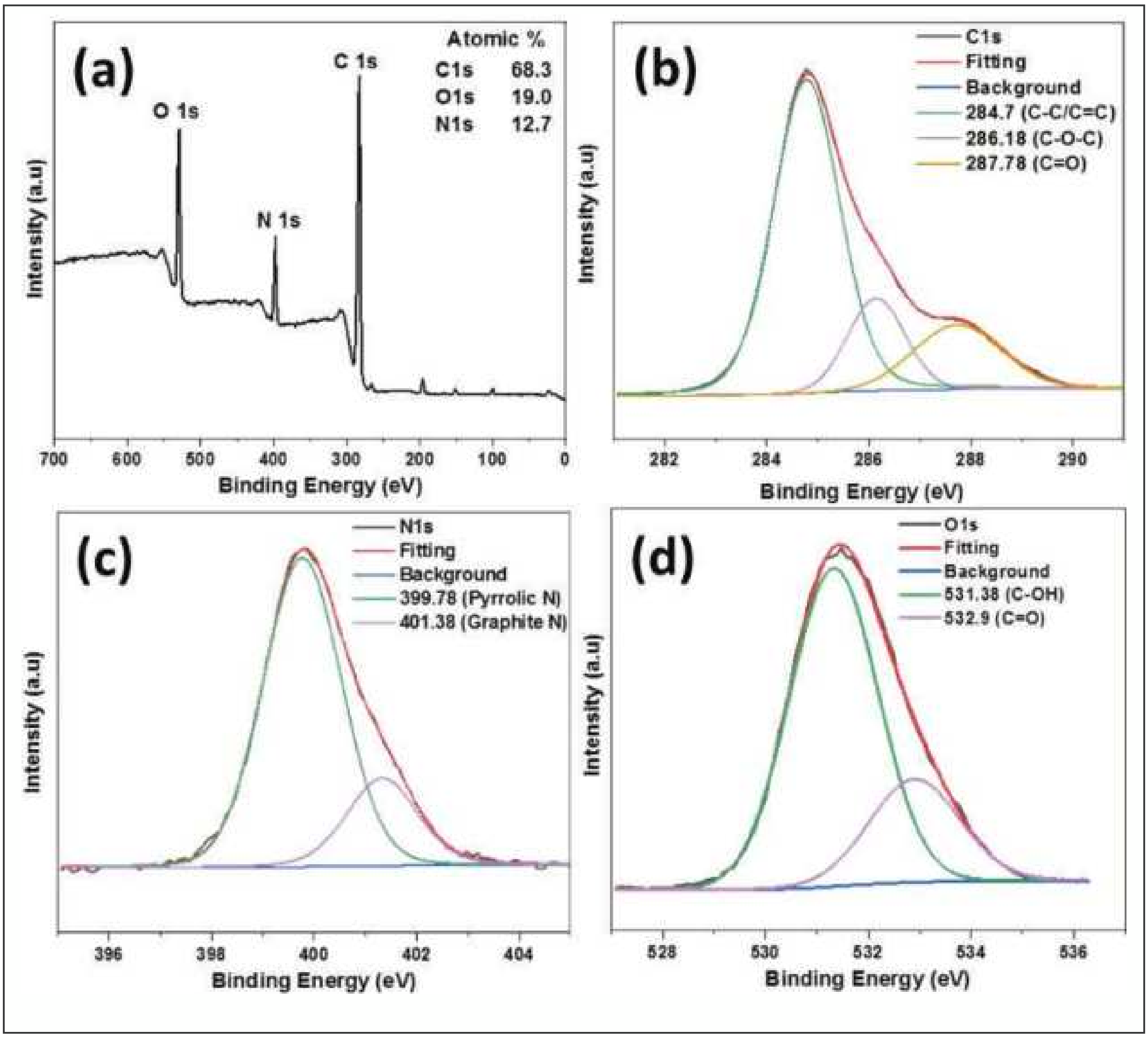

Figure 3: *XPS spectra of survey scan of C-Dots and deconvolution spectrum of C1s, N1s, and O1s*

The surface composition and elemental analysis of the C-dots prepared via the MW approach are investigated using XPS studies. As shown in Figure 3 (a), the survey spectra show three predominant peaks corresponding to the carbon (C1s) at 284 eV, nitrogen (N1s) at 400 eV, and oxygen (O1s) at 531 eV, respectively. The deconvolution of the C1s spectrum (Figure 3 (b))of the C-dots indicated the presence of three types of carbon bonds 284.7 eV (C-C/C=C), 286.15 eV (C-O-C), and 287.78 eV (C=O). The deconvolution spectrum (Figure 3(c)) of the N1s peaks could attribute to the 399.78 eV (Pyrrolic N) and 401.38 eV (Graphite N) and the deconvolution spectrum (Figure 3(d)) of the O1s peaks could attribute to the 531.38 eV (C-OH), 532.62 eV (C=O) [11, 14]. The results obtained from the XPS data for the samples prepared via the MW method indicate that the mass percentages of the carbon, nitrogen and oxygen of the C-dots are 68.3%, 12.7%, and 19%, respectively.

3.2. Photoluminescence characterizations of C-dots:

The UV-Vis absorption spectra and emission spectra of blue-emitting C-dots prepared via the MW method is measured using the spectrofluorometer and the results are shown in Figures 4 (a) and (b), respectively. Figures 4 (b)illustrate the excitation and emission spectrum of the prepared C-dots via the MW route. The C-dots showed absorption at 210 nm and ~ 237 nm which can be attributed to the π → π* transition of the C=C and aromatic C−C bonds, respectively. The absorption peak at around 348 nm stems from the n→π* for C = C and C−N bonds [15]. The inset of Figure 4 (a) shows the C-dots dispersed in water under illumination with visible light of wavelength 405 nm (left) and under UV light (right). The excitation spectrum shows a maximum peak around 400 nm while monitoring the blue emission spectra at 450 nm. In addition, it is found that the blue-emitting C-dots exhibit excitation-dependent emission as shown in Figure 4 (b). A change of excitation wavelength from 350 nm to 450 nm in steps of 10 nm shows the broad emission peak and red-shifted emission from 450 to 550 nm. The red-shift in emission wavelength can be attributed to the presence of different energy trapping on the surface of C-dots [16].The absolute quantum yield of the C-dots prepared via microwave as well as hydrothermal methods are measured using Horiba Fluorolog with an integrating sphere system, and it is found that the C-dots prepared via MW techniques have anabsolute quantum yield of about 41.9%.

3.3. Investigation of fluorescence stability (Concentration, Time-dependent emission of C-dots):

The prepared C-dots are further investigated in detail to understand the influence of concentration, photobleaching, and pH on the emission properties. The effect of C-dot concentration in the range of 0.002 to 1 mg/mL on the optical emission property is investigated. From the concentration-dependent emission shown in Figure 5 (a), it is clear the PL intensity increases with C-dot concentration and reaches a maximum value of 0.5 mg/mL of C-dots and a further increase in the

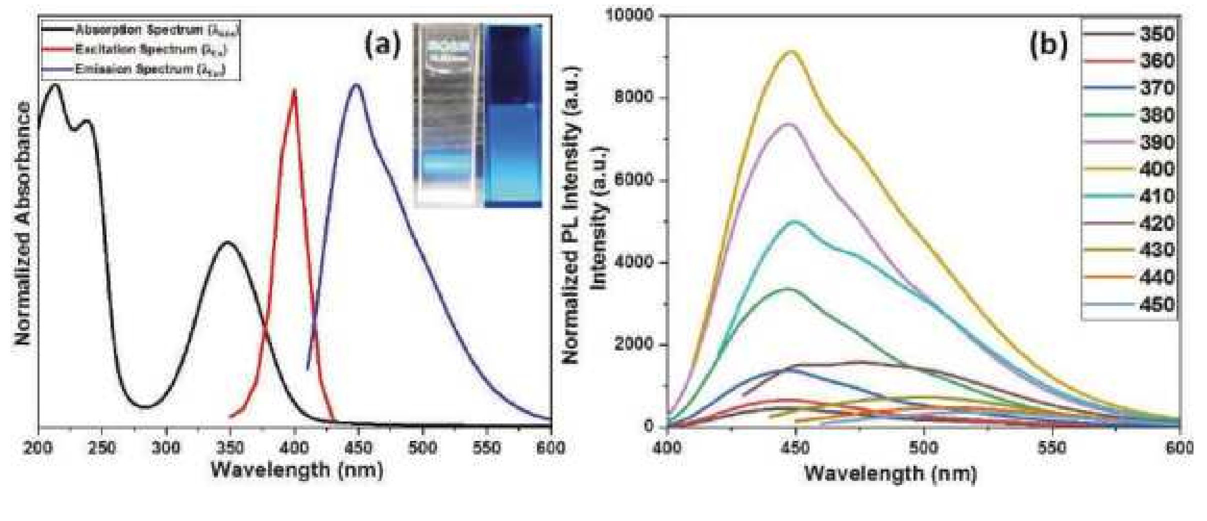

Figure 4: *(a) optical properties of blue-emitting C-dots synthesized by microwave. Inset: picturesof C-dots under daylight (left) and 405 nm (right)). (b) The emission spectra of blue-emitting C-dots under different excitations.*

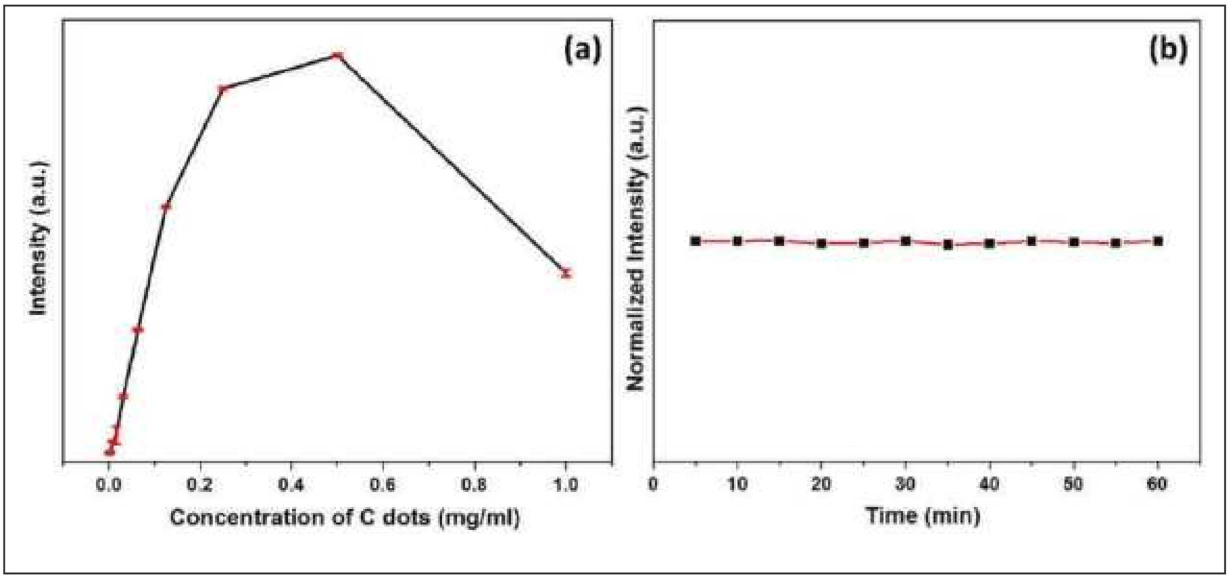

Figure 5: *(a) Dependence of FL intensity on the concentration of C-dots. (b) Resistance to photobleaching performance of C-dots.*

concentration of C-dots results in quenching of the PL intensity. The decrease in emission at higher concentrations can be attributed to self-absorption and collisional quenching, as reported in a previous study [17]. Further, the time-dependent emission spectra under continuous irradiation of a 405 nm laser beam with 8 mW laser power are recorded to investigate the effect of photobleaching for the C-dots and the results are shown in Figure 5 (b). The fluorescence intensity is found to be changed negligibly and thus demonstrates good resistance to photobleaching.

3.4. pH-dependent emission studies:

More interestingly, the PL emission of the C-dots is found to be very sensitive to the pH of the surrounding medium. The fluorescence intensity of C-dots (Figure 6 (a) and (b)) reaches the maximum value at pH = 5 but decreases gradually from pH = 5 to pH = 12. Meanwhile, a red-shift in the emission peak from 460 to 490 nm is observed under acidic pH values from 3 to 5, as shown in Figure 6 (a). The phenomenon can be attributed to the protonation and deprotonation of surface functional groups present on the C-dots. The photographs of C-dot emission in the pH range of 3–12 are shown in Figure 6 (c) in daylight and under 405 nm excitation [18, 19].

3.5. Selectivity and Quantitative Measurements for HA and HAase:

Detection of HA and HAase was performed at room temperature. For HA detection, in a 2 ml vial, 200 µL of C-dots (1 mg/ml) and 100 µL of PBS are taken and then 100 µL of HA solution of different concentrations (0.05, 0.5, 5, 50, 500, 5000, 50000 nM) are added to it separately by following the approach adopted in the literature [20]. The mixture is then diluted to 2 mL of final volume by adding 1.6 ml of DI water. The final mixture solution was subjected to fluorescence measurements. Similarly, for the detection of HAase, in a 2 ml vial, 200 µL of C-dots (1 mg/ml) and 100 µL of PBS and 100 µL of 50 µM HA solution, and 100 µL of HAase solution of different concentrations (50, 100, 1000, 6000 IU). The mixture is then diluted to 2 mL of final volume by adding 1.5 ml of DI water. The final solution was used for the fluorescence measurements. To examine the

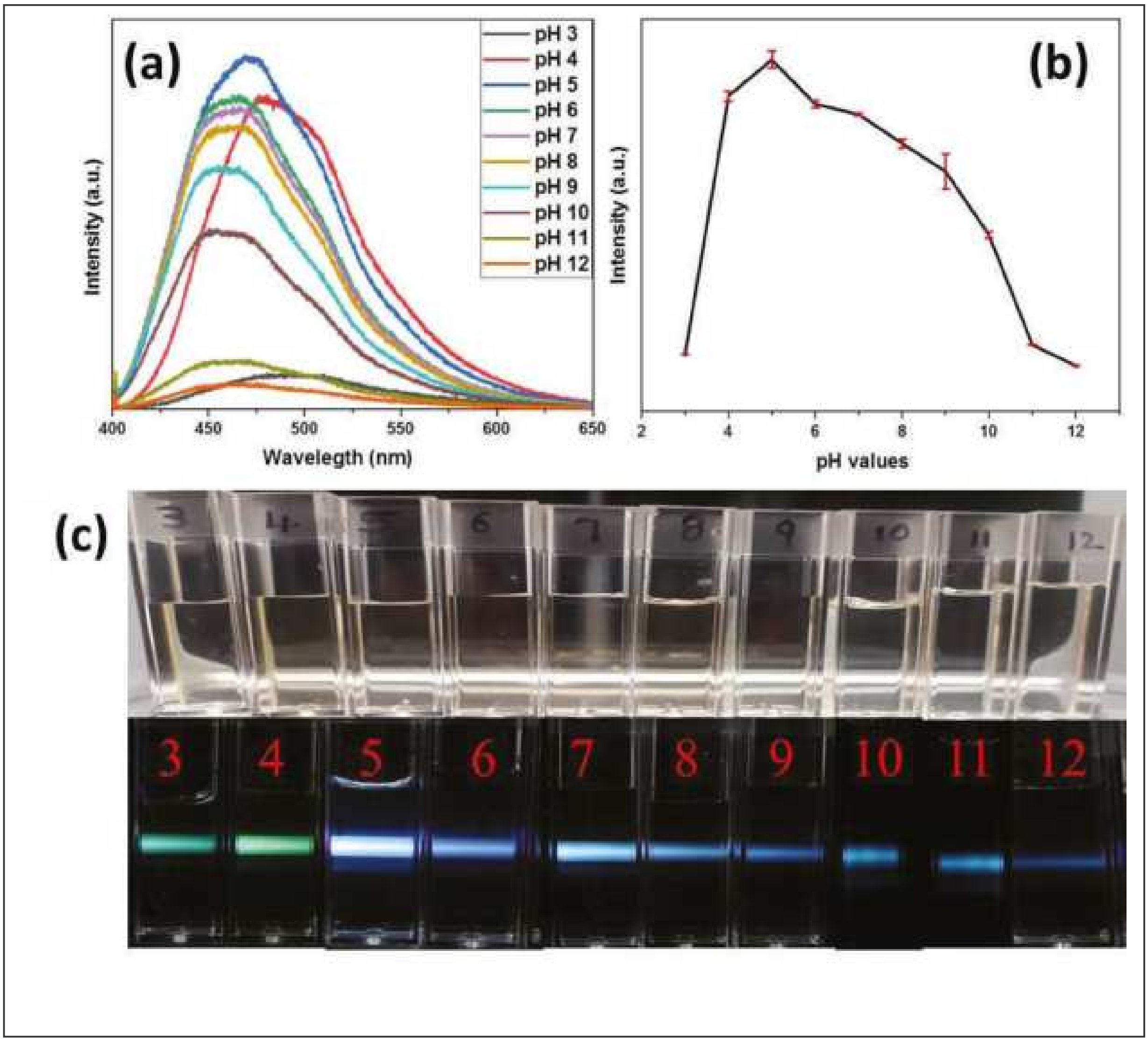

Figure 6:*(a) pH-dependent emission of C-dots, (b) Dependence of PL emission intensity on different pH (pH 3–12), and (c) Photographs of C-dots emission at various pH solutions with 405 nm excitation*

selectivity and specificity of this proposed HA sensing (as shown in Figure 7 (a)), nine different ions including Hg^{2+}, As^{3+}, Pb^{2+}, Cd^{2+}, Mn^{2+}, Cr^{2+}, Mg^{2+}, $Fe^{3+,}$ and $Co^{2+}$are used as target analytes and compared with fluorescence signal in the case of HA. The concentration of HA and other metal ions used here is 50µM, under optimal conditions. All the emission spectra are recorded at 405 nm laser excitation. It is observed that by increasing the HA concentration from 50 pM to 50 µM, the fluorescence emission is quenching gradually, as shown in Figure 7 (b).Reports suggest that, due to the opposite nature of surface charges, the electrostatic attractions of C-dots towards HA, form ground-state complexes resulting in emission quenching via the transfer of excited-state electrons of C-dots to HA via a possible photoinduced electron transfer (PET) mechanism [20]. Figure 7 (c) shows the excellent linear relationship between the quenching efficiency (I_0/I) and the logarithm of HA concentrations with a correlation coefficient R^2=0.99325. Here, I is the integrated intensity at various HA concentrations, I_o is the integrated intensity at 50 µM HA. The limit of

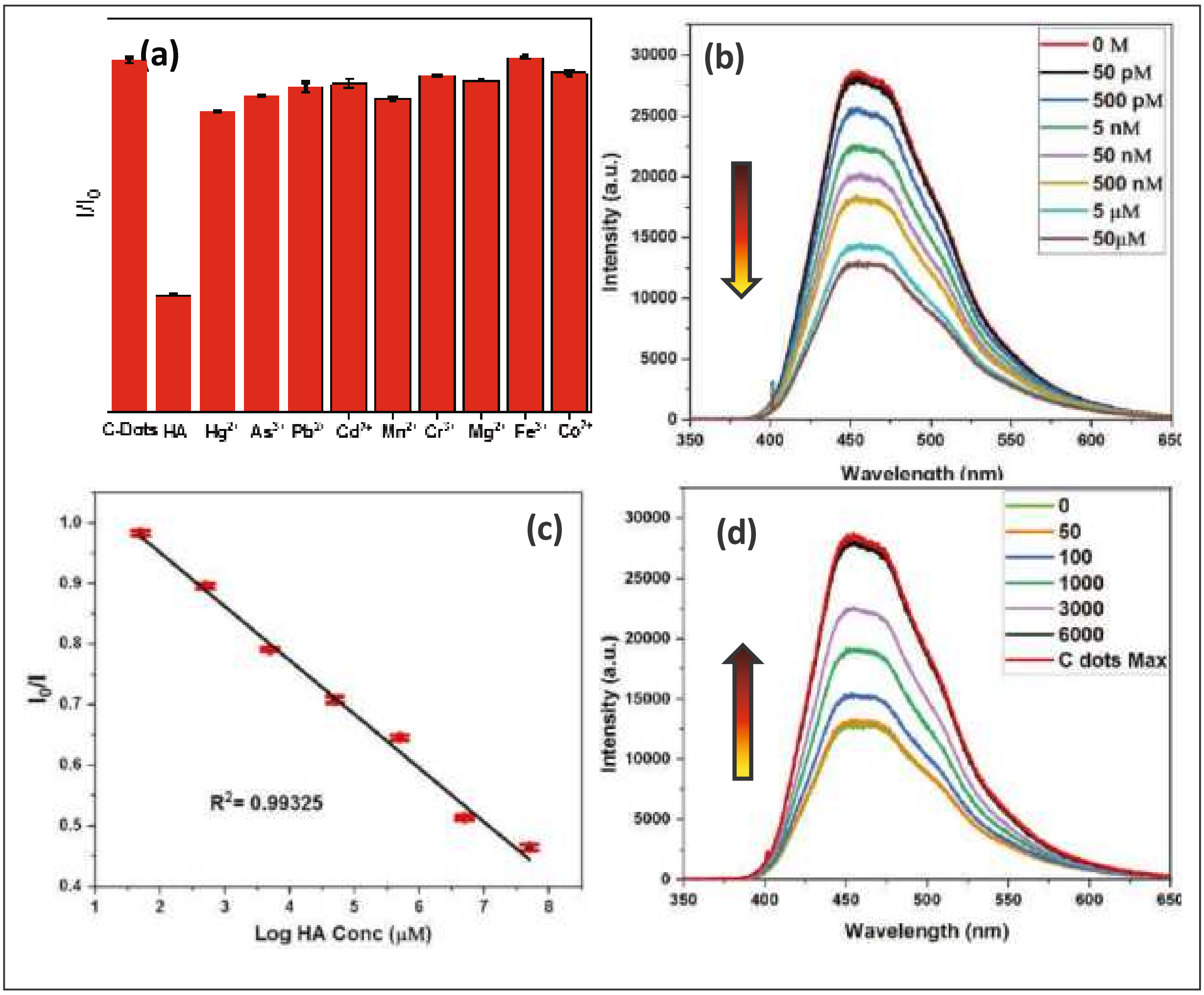

Figure 7:*(a) Effect of various ions on C-dots emission. (b) Emission of C-Dots at different amounts of HA. (c) The plot of the emission integrated intensity versus the logarithmic concentrations of HA. (d) Emission of C-dots at different amount of HAase.*

detection (LOD) for HA sensing is estimated to be 4.26 pM based on the standard deviation of the response and slope rule (LOD= 3.3*σ/s) where σ is the standard deviation calibration curve and s is the slope. Further, by introducing the HAase to the HA and C-dots complex the enzymatic digestion between HA and HAase occurred, thus a gradual emission recovery was found in the range of 50 IU to 6000 IU HAase concentration, as shown in Figure 7 (d), While the complete fluorescence recovery is observed when the HAase concentration reached at 6000 IU [20].

4. Conclusions:

The present work demonstrated the synthesis, characterization, and sensing applications of carbon dots. The C-dots were successfully synthesized by using citric acid as a carbon source and EDA as nitrogen doping sources via microwave-assisted synthesis and characterized by using various techniques including UV-Vis absorption, XRD, FTIR, XPS, and photoluminescence technique. C-dots synthesized via the MW method exhibited blue emission at 405 nm excitation. Further, MW-synthesized C-dots exhibited an absolute quantum efficiency of 41.9%.Further, the prepared C-dots were employed for the concentration, photobleaching, and pH-dependent emission studies, and selective sensing for HA and HAase. The addition of various concentrations of HA in the range of 50 pM to 50 μM resulted in a linear quenching in the C-dots emission (with R^2 value of 0.993) and the sensor provided a LOD of 4.26 pM. On the other hand, with the introduction of different concentrations of HAase in the range of 50 IU to 6000 IU, the C-dot emission recovery was observed. Thus, the MW-based C-dots showed better selectivity and sensitivity and exhibited OFF-ON sensing mode for HA and HAase respectively.

Acknowledgments:

SDG acknowledge Department of Science and Technology for the support through DST-FIST program (SR/FST/PSI-174/2012). SHN acknowledges the support of Manipal Academy of Higher Education through Dr. TMA Pai Ph.D scholarship.

References:

1. S. H. Nannuri, S. Singh, S. Chidangil, S. D. George, Fluorescence-based detection of mercury ions using carbon dots: Role of synthesis route. Journal: Materials Technology: Advanced Performance Materials, 2022, 37:14, 2893-2906. (https://doi.org/10.1080/10667857.2022.2085441)
2. Ng, H. M.; Lim, G.; Leo, C. Comparison between hydrothermal and microwave-assisted synthesis of carbon dots from biowaste and chemical for heavy metal detection: A review. Microchemical Journal 2021, 165, 106116.
3. Batool, M.; Junaid, H. M.; Tabassum, S.; Kanwal, F.; Abid, K.; Fatima, Z.; Shah, A. T. Metal ion detection by carbon dots—a review. Critical Reviews in Analytical Chemistry 2020, 1-12.
4. Molaei, M. J. Principles, mechanisms, and application of carbon quantum dots in sensors: A review. Analytical Methods 2020, 12, 1266-1287.
5. Miao, S.; Liang, K.; Zhu, J.; Yang, B.; Zhao, D.; Kong, B. Hetero-atom-doped carbon dots: Doping strategies, properties and applications. Nano Today 2020, 33, 100879.
6. Ji, C.; Zhou, Y.; Leblanc, R. M.; Peng, Z. Recent developments of carbon dots in biosensing: A review. ACS sensors 2020, 5, 2724-2741.
7. He, X.; Li, H.; Liu, Y.; Huang, H.; Kang, Z.; Lee, S.-T. Water soluble carbon nanoparticles: Hydrothermal synthesis and excellent photoluminescence properties. Colloids and Surfaces B: Biointerfaces 2011, 87, 326-332.
8. Cailotto, S.; Amadio, E.; Facchin, M.; Selva, M.; Pontoglio, E.; Rizzolio, F.; Riello, P.; Toffoli, G.; Benedetti, A.; Perosa, A. Carbon dots from sugars and ascorbic acid: Role of the precursors on morphology, properties, toxicity, and drug uptake. ACS medicinal chemistry letters 2018, 9, 832-837.
9. P.T. Bot, I.E. Hoefer, J.J. Piek, G. Pasterkamp, Hyaluronic acid: targetingimmune modulatory components of the extracellular matrix inatherosclerosis, Curr. Med. Chem. 15 (2008) 786–791.
10. Yoo, D.; Park, Y.; Cheon, B.; Park, M.-H. Carbon dots as an effective fluorescent sensing platform for metal ion detection. Nanoscale research letters 2019, 14, 1-13.
11. Xiao, Q.; Liang, Y.; Zhu, F.; Lu, S.; Huang, S. Microwave-assisted one-pot synthesis of highly luminescent n-doped carbon dots for cellular imaging and multi-ion probing. MicrochimicaActa 2017, 184, 2429-2438
12. Edison, T. N. J. I.; Atchudan, R.; Sethuraman, M. G.; Shim, J.-J.; Lee, Y. R. Microwave assisted green synthesis of fluorescent n-doped carbon dots: Cytotoxicity and bio-imaging applications. Journal of Photochemistry and Photobiology B: Biology 2016, 161, 154-161.
13. Stachowska, J. D.; Murphy, A.; Mellor, C.; Fernandes, D.; Gibbons, E. N.; Krysmann, M. J.; Kelarakis, A.; Burgaz, E.; Moore, J.; Yeates, S. G. A rich gallery of carbon dots based photoluminescent suspensions and powders derived by citric acid/urea. Scientific reports 2021, 11, 1-14.
14. Niu, J.; Gao, H.; Wang, L.; Xin, S.; Zhang, G.; Wang, Q.; Guo, L.; Liu, W.; Gao, X.; Wang, Y. Facile synthesis and optical properties of nitrogen-doped carbon dots. New Journal of Chemistry 2014, 38, 1522-1527.
15. Lan, M.; Guo, L.; Zhao, S.; Zhang, Z.; Jia, Q.; Yan, L.; Xia, J.; Zhang, H.; Wang, P.; Zhang, W. Carbon dots as multifunctional phototheranostic agents for

photoacoustic/fluorescence imaging and photothermal/photodynamic synergistic cancer therapy. Advanced Therapeutics 2018, 1, 1800077.

16. Mohan, R.; Drbohlavova, J.; Hubalek, J. Dual band emission in carbon dots. Chemical Physics Letters 2018, 692, 196-201.
17. Song, Y.; Zhu, S.; Xiang, S.; Zhao, X.; Zhang, J.; Zhang, H.; Fu, Y.; Yang, B. Investigation into the fluorescence quenching behaviors and applications of carbon dots. Nanoscale 2014, 6, 4676-4682.
18. Zhang, C.; Cui, Y.; Song, L.; Liu, X.; Hu, Z. Microwave assisted one-pot synthesis of graphene quantum dots as highly sensitive fluorescent probes for detection of iron ions and ph value. Talanta 2016, 150, 54-60.
19. Ehtesabi, H.; Hallaji, Z.; Nobar, S. N.; Bagheri, Z. Carbon dots with ph-responsive fluorescence: A review on synthesis and cell biological applications. MicrochimicaActa 2020, 187, 1-18.
20. Yang, K.; Liu, M.; Wang, Y.; Wang, S.; Miao, H.; Yang, L.; Yang, X. Carbon dots derived from fungus for sensing hyaluronic acid and hyaluronidase. Sensors and Actuators B: Chemical 2017, 251, 503-508.

About the Authors

Dr. Shivanand H Nannuri *received his M. Sc. In Nanoscience and Technology from Department of Atomic and Molecular Physics at Manipal Academy of Higher Education in 2014, and pursued his doctoral studies under the guidance of Professor Sajan Daniel George. His doctoral research involved Synthesis, Characterization and Sensing Applications of Carbon Dots and Up-conversion Nanoparticles.*

Dr. Abhijeet Pandey *completed his post-graduation in Pharmaceutics from North Maharashtra University, Jalgaon, Maharashtra. He obtained PhD from Maharaja Sayajirao University of Baroda, Vadodara, Gujarat and Bhabha Atomic Research Centre, Mumbai, Maharashtra, India. Later, he joined as Postdoctoral Research Fellow at Manipal College of Pharmaceutical Sciences, Manipal, Karnataka, India and also he is Guest Scientist (EMBO Fellow) at Medical University of Graz, Austria. His research interests include synthesis of surface modified nanoparticles (polymeric and inorganic) for targeted cancer therapy, stimuli responsive drug release, novel injectable formulation and intranasal drug delivery for brain targeting.*

Dr. Srinivas Mutalik *received his Ph.D. in Pharmaceutical Sciences from Manipal Academy of Higher Education, Manipal, India. Presently, he is a Professor and head of Department of Pharmaceutics, MAHE, Manipal. After completing his PhD he joined as a Postdoctoral Research Fellow at The University of Queensland, Brisbane, Australia. His research expertise is development and evaluation of drug/ bioactive loaded nanocarriers.*

Dr. Sajan Daniel George *received his Ph.D. in photonics from Cochin University of Science and Technology (India). Presently, he is a Professor and Head of the Department of Atomic and Molecular Physics at Manipal Academy of Higher Education. He worked as a scientific colleague at Katholikek University of Leuven (Belgium), Leibniz University of Hannover (Germany), Technical University of Darmstadt (Germany). He is a receipt of Dr. T. M. A. Pai Endowment Chair of Manipal Academy of Higher Education and currently coordinator of Centre for Applied Nanosciences. He is a Fellow of Royal Society of Chemistry and Indian Chemical Society His research interests include micro/optofluidics, photo- thermal methods, nano-biophotonics, biomedical applications of laser, fluorophore-nanoparticle interactions.*

Synthesis and drug delivery applications of albumin and gelatin based protein nanoparticles

Ram P. Das[a,b], B.G. Singh[a,b] and A. Kunwar[a,b]*
[a]*Radiation & Photochemistry Division, Bhabha Atomic Research Centre, Trombay, Mumbai-400085, INDIA*
[b]*Homi Bhabha National Institute, Anushaktinagar, Mumbai –400094, INDIA*
**Email: kamit@barc.gov.in*

Abstract

Present article demonstrates a green method of thermal denaturation involving Pluronic and a modified chemical cross-linking method involving dithiothreitol (DTT) for the synthesis of nanoparticles from naturally occurring protein sources such as albumin and gelatin. Curcumin, a well-established anti-inflammatory drug was entrapped within protein nanoparticles to study the effects of particle size and particle hydrophobicity on the cellular delivery of entrapped drug. The results established that the particle size of ~125 nm and hydrophilic lipophilic balance of ~22 is optimal to achieve maximum intracellular concentration of the entrapped drugs. Finally, attempts were also made to prepare the nano formulations of anti-cancer drugs like doxorubicin and irinotecan and to evaluate them using mice models.

1. Introduction

Drug delivery system (DDS) promises to solve a number of issues associated with conventional therapeutic agents, including their poor bioavailability, lack of targeting capability, nonspecific distribution, systemic toxicity and low therapeutic index [1,2]. Naturally occurring bio-molecules such as proteins are an attractive alternative to synthetic polymers which are commonly used in fabrication of DDS because of their biocompatibility and biodegradability [3]. Moreover, due to the presence of reactive groups (thiol, amino and carboxylic acid groups) in their primary structure, protein-based nanoparticles can be surface functionalised with the target specific ligands [4]. Common methods available for the preparation of protein nanoparticles are desolvation, emulsification, high pressure homogenization, etc [5]. Major disadvantages with these methods are use of organic solvent and removal of organic oil from the nanoparticle solution. Further, the most common stabilizing agent used in previous studies is glutaraldehyde which can cause toxicity [6]. Therefore, there is a need to develop greener methods that can overcome toxicity associated with excipients. Accordingly, our group has worked on the development of physical and chemical methods of preparing nano-carrier from protein sources [7-9]. Among protein sources, albumin-based nanoparticles offer several advantages like biocompatibility, biodegradability and most importantly passive targeting at tumor sites via complementary pathways such as enhanced permeation retention (EPR) effect, and receptor (gp60 and SPARC)-mediated transcytosis [10]. Similarly, gelatin is one of the most widely used proteinaceous polymers in pharmaceutical formulations for drug delivery applications. Gelatin is a protein hydrolysate obtained from acid/base hydrolysis of collagen [11]. It is also considered as GRAS (generally regard as safe) to prepare clinical grade drug delivery systems. Therefore, human serum albumin (HSA) and gelatin were chosen as the starting materials in our studies. Further, curcumin a major chemical constituent of turmeric has been reported for various pharmacological activities [12]. However, its clinical translation as a therapeutic drug has been limited due to poor aqueous solubility, faster cellular metabolism and low bioavailability [13]. Recently a lot of work has been reported on the use of DDS for improving the biological stability and availability of curcumin. Most of these studies have been done using inorganic nanoparticles and liposomes and results have suggested the role of particle size in controlling the release and cellular uptake of entrapped drug. Accordingly, it was aimed to study effects of particle size and particle hydrophobicity on the cellular delivery of curcumin through albumin and gelatin based nanoparticles. The results pertaining to these studies are briefly summarized in the following sections. For detailed description, readers are encouraged to go through our prior publications [7-9,14-16].

2. Methods

All chemicals with maximum available purity were employed in the study. The characterization of protein nanoparticles was performed employing dynamic light scattering (DLS), zeta potential measurement, scanning electron microscopy (SEM & Cryo-SEM), transmission electron microscopy (TEM), grazing incidence attenuated total reflection Fourier transform infrared spectroscopy (GATR-FTIR). The binding and interaction of drug molecules with protein nanoparticles was studied by UV-visible, fluorescence and circular dichroism (CD) spectrophotometric techniques. The cellular uptake and *in vitro* cytotoxicity studies were performed in cellular model (A549) of lung cancer maintained at Bhabha Atomic Research Center. Fluorescence imaging was performed using laser scanning confocal microscope.

3. Results & Discussion

3.1 Particle size-uptake correlation of curcumin loaded albumin nanoparticles

The synthesis of stable HSA nanoparticles of tunable size is a challenging task for its successful therapeutic application. In order to address this, thermal denaturation method was employed for the preparation of HSA nanoparticles of different sizes. In brief, the mixture containing 1% w/v HSA and 5 mM sodium deoxycholate (NaDC) in phosphate buffer saline (PBS) was heated at 67 °C and 70 °C for two hours followed by cooling at room temperature. The characterization of particle size and morphology confirmed the formation of nanoparticle of hydrodynamic size of 30.0 ± 2.2 (HSAT1) and 60.0 ± 5.9 (HSAT2) nm, respectively at denaturation temperatures of 67 °C and 70 °C. To overcome the limitation of size tunability of above-mentioned physical method, chemical cross-linking method was also tested. In brief, 1% HSA solution was treated with different concentration of dithiothreitol (DTT, 1 – 10 mM) and NaDC (5 - 30 mM) at 37 °C for 1 hr. After this, 1 ml ethanol was added drop wise to the solution with constant stirring and then incubated at room temperature for approximately 2 hrs. The results indicated that particle size of HSA nanoparticles increased with increase in DTT and/or NaDC concentration. Addition of NaDC increased the negative surface charge and improved the stability of HSA nanoparticles. The reaction condition was optimized by varying DTT concentration from 0.85 to 3.25 mM and keeping NaDC concentration fixed at 5 mM to obtain HSA nanoparticles of sizes 25 ± 2 nm (HSAnp1), 64 ± 6 (HSAnp2) nm, 125 ± 10 (HSAnp3) nm and 234 ± 40 (HSAnp4) nm respectively (Fig. 1A & 1B). The surface charge of the HSA nanoparticle was characterized by zeta (ζ) potential measurements and the values for HSAnp1, HSAnp2, HSAnp3, HSAnp4, HSAT1 and HSAT2 were obtained as -12.36 ± 0.73, -12.1 ± 0.59, -11.96 ± .67, -10.88 ± 0.6, -13.67 ± 0.74 and -11.42 ± 0.52 mV respectively. After optimization of the process to acquire HSA nanoparticles of desired size, the effect of particle size on the loading of curcumin was studied and compared with the native protein. For this, curcumin was encapsulated into HSA nanoparticle by adsorption method. In brief, the aqueous suspension containing the HSA nanoparticles was mixed with the desired concentration of ethanolic curcumin solution. The solution was allowed to equilibrate for 15 minutes and unbound curcumin was removed by dialysis using PBS as dialyzing solvent for 12 hrs. The resulting solution contained curcumin loaded HSA nanoparticles and was used for further studies. Amount of curcumin loaded in the carrier was estimated by employing UV-Visible (UV-vis) absorption technique as reported previously [17]. Drug loading efficiency was calculated from the ratio of amount of curcumin entrapped to the amount of protein taken. The loading efficiency of chemically prepared nanoparticles followed the order HSA native < HSAnp1 < HSAnp2 < HSAnp3 < HSAnp4 suggesting that loading efficiency increased with increasing particle size. Similar trend was observed for thermally synthesized HSA nanoparticles (HSAT1< HSAT2). However, in comparison to HSAnp1 and HSAnp2 respectively, the loading efficiency of HSAT1 and HSAT2 for curcumin was lower Further, the interaction of curcumin with HSA nanoparticles was investigated by UV–vis and fluorescence spectroscopy. HSA in native and nanoparticle forms exhibit absorption in the range of 200 nm to 350 nm with its absorption maximum at 280 nm, while curcumin absorbs in the range of 200 nm to 500 nm with maximum at 420 nm (Fig. 1C). In order to determine the binding constant, the absorbance of curcumin-HAS solution at 420 nm was recorded by mixing varying concentration of curcumin (from 1 - 10 μM) with fixed concentration of HAS (native/nanoparticles). The double reciprocal plot of the differential absorbance of HSA-curcumin solution at 420 nm was plotted as a function of curcumin concentration according to Benesi-Hildebrand equation (1).

$$\frac{1}{\Delta A_{420\,\mathrm{nm}}} = \frac{1}{K\Delta\varepsilon_{420\,\mathrm{nm}}[\mathrm{HSA}][\mathrm{CUR}]} + \frac{1}{\Delta\varepsilon_{420\,\mathrm{nm}}[\mathrm{HSA}]} \qquad (1)$$

Where K is the equilibrium constant, $\Delta A_{420\ \mathrm{nm}}$ and $\Delta\varepsilon_{420\ \mathrm{nm}}$ are the respective differential absorbance and extinction coefficient values of the HSA-curcumin complex at 420 nm, and [HSA] and [CUR] are the concentration terms. The ratio of the slope and intercept obtained from the linear fit of above plots gave the K values which was in the order of 7 ± 0.3 x 10^4 M^{-1}, 1.1 ± 0.6 x 10^5 M^{-1}, 1.4 ± 0.8 x 10^5 M^{-1}, 2.1 ± 1.1 x 10^5 M^{-1}, 6.1 ± 0.2 x 10^4 M^{-1} and 9.9 ± 0.7 x 10^4 M^{-1} respectively for HSAnp1, HSAnp2, HSAnp3, HSAnp4, HSAT1 and HSAT2. Comparing these values, it is evident that the K value of curcumin with HSA increased with increase in particle size. Notably chemically prepared HSA nanoparticles exhibited higher binding constant for curcumin at a particular particle size. The binding of curcumin with HSA nanoparticle may be attributed to the existence of hydrophobic pocket. This was confirmed by monitoring the binding of HSA nanoparticles with fluorescence dye like ANS and prodan, which are used as a reporter to probe hydrophobicity of a system [18]. Notably, the fluorescence intensity of ANS and prodan is very low in aqueous solution. It increased significantly in presence of HSA nanoparticles. The increase in

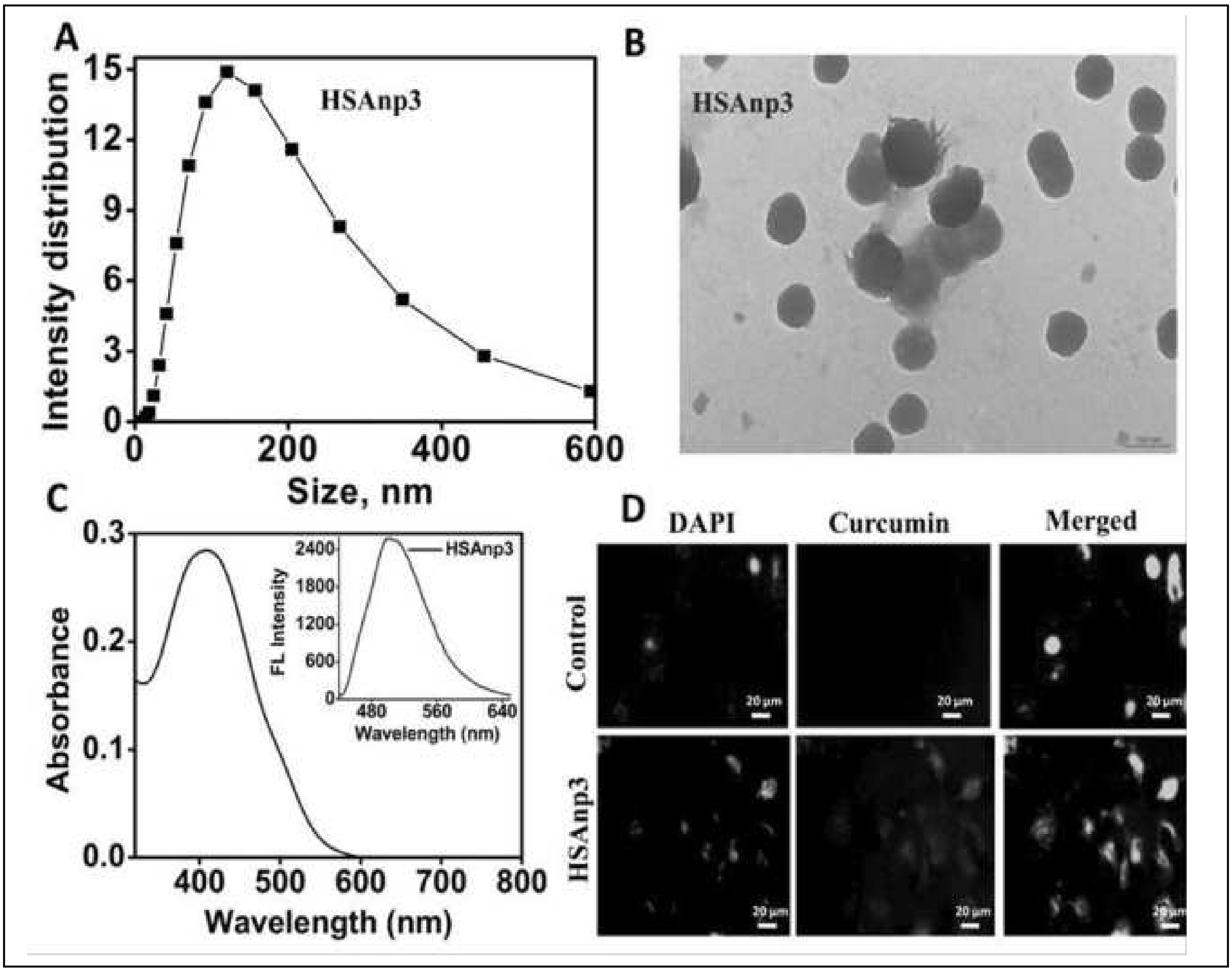

Figure 1: *(A) Intensity correlation function of the albumin nanoparticles by DLS. (B) Image corresponds to TEM of HSAnp3 nanoparticles. (C) Plot corresponds to absorption and fluorescence (inset) intensity of curcumin (10 µM) loaded albumin nanoparticles (HSAnp3). (D) Figure shows fluorescence of curcumin inside A549 cells treated with 12.5 µM of curcumin through HSA nanoparticles (HSAnp3) for 10 hrs. DAPI fluorescence indicates the position of nucleus within cells.*

the fluorescence intensity at a fixed concentration of the hydrophobic marker was in the order HSAnp4 > HSAnp3 > HSAnp2 > HSAnp1 > HSA native form. These results suggested that increase in the average size of HSA nanoparticles, increased hydrophobic pockets that was responsible for the enhanced binding of a hydrophobic molecule like curcumin. Similar analysis also confirmed the presence of higher hydrophobic pockets in chemically cross-linked nanoparticles HSAnp1 and HSAnp2 as compared to thermally prepared nanoparticles HSAT1 and HSAT2 respectively justifying the difference in their K values. The release profile of curcumin from HSA nanoparticles was investigated under reservoir-sink condition (reservoir: pH 7.4 containing 0.1 % Tween 80, sink: pH 7.4) at 37 °C. At earlier time point i.e., till 40 hrs, the cumulative release of curcumin from HSA nanoparticles irrespective of its size was slower than native form. Also, between the nanoparticles, the release of curcumin was found to decrease with increase in particle size. For example, the percentage (%) of curcumin released from HSA native, HSAnp1, HSAnp2, HSAnp3, HSAnp4, HSAT1 and HSAT2 at 40 hrs was 9.6 ± 0.4, 8.3 ± 0.4, 7.5 ± 0.4, 6.0 ± 0.3, 4.4 ± 0.2, 7.1 ± 0.4 and 6.9 ± 0.3 respectively. However, at a longer time point (96 hrs), the respective cumulative drug released from native HAS, HSAnp1, HSAnp2, HSAnp3, HSAnp4, HSAT1 and HSAT2, estimated was 49.9 ±0.4 %, 52.5 ± 4.0 %, 57.6 ± 5.3 %, 70.0 ± 6.0 %, 65.0 ± 5.0 %, 54.8 ± 4.0 % and 58.4 ±4.1 %, respectively. Finally, the internalization or uptake of curcumin loaded HSA nanoparticles was evaluated in A549 cells (Fig. 1D). For this, A549 cells were treated with 12.5 µM of curcumin entrapped in HSA nanoparticles (HSAnp1, HSAnp2, HSAnp3, HSAnp4, HSAT1 and HSAT2) for 10 hrs and the amount of curcumin in the cell lysate was estimated by absorbance and fluorescence measurement. The uptake levels of curcumin through HSA native, HSAnp1, HSAnp2, HSAnp3, HSAnp4, HSAT1 and HSAT2 after a common treatment period of 10 hrs was estimated as 433 ± 25 ng/mg protein, 604 ± 34 ng/mg protein, 703 ± 41 ng/mg protein, 876 ± 51 ng/mg protein, 751 ± 42 ng/mg protein, 453 ± 29 ng/mg protein and 588 ± 25 ng/mg protein respectively in comparison to 419 ± 31 ng/mg protein of DMSO curcumin. Thus, cellular uptakes increased with increase in particle size until ~ 125 nm, and a further increase in the carrier size decreased the cellular uptake. Moreover, the comparative study indicated that HSA nanoparticles prepared by thermal denaturation method exhibited lesser loading and cellular delivery of entrapped drug (curcumin) than those prepared by chemical crosslinking methods at a given size. Curcumin is known to be cytotoxic to cancerous cells and therefore higher cellular uptake is expected to increase its cytotoxicity. At an early time point of 48 hrs, the toxicity of curcumin carried by different HSA nano-carriers exhibited the particle size effect with HSAnp3 (~125 nm) showing the maximum toxicity. In conclusion above studies together demonstrated the potential of HSA nanoparticles to increase the bioavailability of a hydrophobic drug like curcumin and also the optimal size for maximum cellular uptake.

3.2 Particle hydrophobicity-uptake correlation of curcumin loaded gelatin nanoparticles

The next objective was to study the effect of particle hydrophobicity on the cellular uptake/deliver of the entrapped drug. In order to address this use, first the methodology of preparing gelatin based nanoparticle of varying hydrophilic and lipophic balance (HLB) was optimised and subsequently these nanoparticles were evaluated for cellular delivery of curcumin. In brief, physical method involving heating of the aqueous solution of gelatin at 60 °C followed by gradual cooling at room temperature yielded gelatin nanoparticles. Having observed this, initially the concentration of gelatin was optimized to obtain nanoparticles of desired size and viscosity. The average hydrodynamic size of the gelatin nanoparticle as estimated by DLS exhibited a concentration dependent increase from 339± 11 nm at 0.5% to 774± 27 nm at 3% of gelatin. Most importantly the solution of gelatin nanoparticles at concentration ≥1% exhibited bigger particle size and resulted in phase separation in the form of gel. Taken together, above results indicated that 0.5% (w/v) is the ideal concentration of gelatin to prepare relatively stable nanoparticles in solution phase. Further, to vary surface hydrophobicity, gelatin at a fixed concentration of 0.5% (w/v) was mixed with 5-40% (w/w with respect to gelatin) of Pluronic blend of varying hydrophobic lipophilic balance (HLB) of 8, 15, 18 and 22 and processed by thermal method to yield gelatin-Pluronic nanoparticles. The Pluronic blend of varying HLB was prepared by mixing two pure Pluronic P123 and

F127 of HLB of 22 and 8 respectively in different weight ratio as presented by equation (2).

$$HLB_{blend} = \frac{w_1 HLB_1 + w_2 HLB_2}{w_1 + w_2} \qquad (2)$$

Where, HLB_{blend} is the HLB value of the blend, w_1 and w_2 are the respective weights of F127 and P123 and HLB_1 and HLB_2 are the HLB values of F127 and P123, respectively. The thermal heating of gelatin (above its phase transition temperature ~37° C) in presence of pluronic allows the hydrophobic domain of the pluronic to interact with random coil (hydrophobic moiety) structure of gelatin leading to its contraction and formation of stable nanoparticle. The results clearly indicated that both concentration as well as HLB value of Pluronic blend dictated the size of gelatin nanoparticles. For example, the size of nanoparticles decreased with the increasing concentration (5 to 40%) of Pluronic blend irrespective of its HLB. Similarly, the size of nanoparticles decreased with the decreasing HLB values irrespective of the concentration of Pluronic blend. Considering that the size of nanoparticles required for enhanced cellular uptake is in range of 100-200 nm (as per the result of previous section), 20% of Pluronic blend was found to be optimum to obtain gelatin nanoparticles of desired size range. Notably, at a fixed concentration of 0.5% (w/v) gelatin and 20% (w/w with respect to gelatin) of Pluronic blend, the variation in HLB from 22 to 8 did not cause much change in morphology (~ spherical) and surface charge (~ -6.5 mV) while reducing the size of nano-composite to 165 ± 097 nm, 161 ± 093 nm, 157 ± 086 nm, 145 ± 089 nm and 134 ± 074 nm respectively at HLB 22, HLB 18, HLB 15, HLB 12 and HLB 8 (Fig. 2A & 2B). Further, the mixing of the pluronic polymer with gelatin is expected to cause change in the surface hydrophilicity/hydrophobicity of the nano-composites. In order to understand this, surface hydrophobicity was determined by contact angle measurements using water as solvent. The water contact angle of the gelatin nanoparticle without pluronic coating was 40. 9 ± 0.4°. The coating of pluronic led to increase in the contact angle of gelatin nanoparticles from 49. 8 ± 0.8° at HLB 22 (pure F127) to 80.3 ± 9.8° at HLB 8 (pure P123). The increase in the contact angle of HLB 8 coated gelatin nanoparticle is attributed to the hydrophobic characteristics of P123 polymer. Together it suggested that the surface hydrophobicity of gelatin-pluronic nanoparticles increased with decreasing HLB value of pluronic. Subsequently, curcumin was entrapped within gelatin-Pluronic nanoparticle of varying HLB by adsorption method as described in previous section. It was observed that the loading efficiency of curcumin into gelatin-pluronic nanoparticles was dependent on the HLB value of pluronic blend. The loading efficiency of curcumin increased with decrease in the HLB value in the order of HLB 8 > HLB 12 > HLB 15 > HLB 18 > HLB 22. The entrapment efficiency also followed the same order with the values of 88.7 ± 5.7 % and 98.9 ± 8.9 % at HLB 22 and HLB 8 respectively. The plain gelatin nanoparticles without pluronic coating showed the lowest loading as well as entrapment of curcumin. With decreasing HLB value, the hydrophobicity of the gelatin nanoparticle increased which facilitated curcumin to bind with gelatin nanoparticle more efficiently through hydrophobic interaction. This was further confirmed by estimating the binding constant between curcumin and the gelatin-pluronic nanoparticles using the Benesi-Hildebrand equation (equation 3) and assuming the 1:1 stoichiometry between curcumin and nanoparticles.

$$\frac{1}{\Delta A_{420\,nm}} = \frac{1}{K\Delta\varepsilon_{420\,nm}[\text{gelatin}-\text{pluronic}][\text{CUR}]} + \frac{1}{\Delta\varepsilon_{420\,nm}[\text{gelatin}-\text{pluronic}]} \qquad (3)$$

In above equation, K is the equilibrium constant, ΔA_{420nm} and $\Delta\varepsilon_{420nm}$ are the respective differential absorbance and extinction coefficient values of curcumin bounded to the nanoparticle at 420 nm, and [gelatin-pluronic] and [CUR] are the concentration terms. For this analysis, the concentration of the nanocarrier was fixed at 0.5% (w/v) and of curcumin varied from 1-10 µM. The K values obtained from the ratio of the slope and intercept for plain gelatin nanoparticles and gelatin-pluronic nanoparticles of HLB 22, HLB 18, HLB 15, HLB 12 and HLB 8 were $4.6 \pm 0.1 \times 10^5$ M^{-1}, $4.9 \pm 0.6 \times 10^5$ M^{-1}, $5.0 \pm 0.5 \times 10^5$ M^{-1}, $5.5 \pm 0.8 \times 10^5$ M^{-1}, $9.3 \pm 0.7 \times 10^5$ M^{-1} and $11.5 \pm 0.9 \times 10^5$ M^{-1} respectively. Comparing these values, it can be inferred that the K value of curcumin with the gelatin nanoparticles increased with decrease in the HLB value. To account above observations, fluorescence spectrum of curcumin bound to gelatin-pluronic nanoparticle was also measured by exciting at 420 nm (Fig. 2C). The result indicated that the emission wavelength of curcumin loaded into gelatin-pluronic nanoparticle was blue shifted as compared to those in plain gelatin nanoparticles (without pluronic). Curcumin bound to plain gelatin nanoparticles showed emission maximum at 539 nm whereas emission maximum with HLB 22, HLB 18, HLB 15, HLB 12 and HLB 8 were observed at 529, 523, 518, 516 and 513 nm respectively. This blue shift in the emission spectra as well as increase in emission intensities confirmed that curcumin experienced more hydrophobic environment in pluronic coated gelatin nanoparticles. As per previous reports, the emission maxima of curcumin can be correlated to the polarity of its microenvironment [19]. Thus, by comparing the emission maxima of curcumin bound to gelatin-pluronic nanoparticle of different HLB values with those in organic solvents, the polarity experienced by curcumin within plain gelatin nanoparticles and gelatin-pluronic nanoparticles of HLB 22, HLB 18, HLB 15, HLB 12 and HLB 8 were found to be equivalent to that of water, ethanol, acetonitrile, Tx-100, serum albumin and acetone respectively. Further, the existence of higher hydrophobic pocket in pluronic coated gelatin nanoparticle was confirmed by monitoring their binding with fluorescence dyes like ANS and prodan which were used as a hydrophobicity marker in a system. Fluorescence intensity of ANS and prodan significantly increased in the presence of gelatin nanoparticle and the increase in the fluorescence intensity followed the order HLB 8 > HLB 12 > HLB 15 > HLB 18 > HLB 22 > plain gelatin nanoparticle. These results suggested that the increase in the number of hydrophobic pockets within gelatin-pluronic nanoparticle with decreasing HLB value of pluronic accounted for higher loading as well as entrapment efficiencies of curcumin. The release profile of curcumin from different pluronic stabilized gelatin nanoparticles was investigated under reservoir-sink condition (reservoir: pH 7 containing 0.1 % Tween 80, sink: pH 7.4) at 37 °C. Release of curcumin from pluronic coated gelatin nanoparticle followed biphasic pattern marked by initial slow release up to 30 hrs and then faster release till the end of experiment (80 hrs). Additionally, the release of curcumin from pluronic coated gelatin nanoparticle showed HLB dependency with decreasing HLB value in the gelatin nanoparticles facilitated slower drug release at earlier time points (less than 30 hrs) and higher drug release at later time points. The effect of HLB on the cellular uptake of gelatin-pluronic nanoparticles was monitored by following the delivery of curcumin through these nanocarriers into A549 cells. According to results, the amount of curcumin uptake estimated through plain gelatin nanoparticles and pluronic coated gelatin nanoparticles of HLB 22, HLB 18, HLB 15, HLB 12 and HLB 8 after a common treatment period of 6 hrs was 108 ± 9 ng/mg protein, 336 ± 18 ng/mg protein, 287 ± 15 ng/mg protein, 229 ± 13 ng/mg protein, 188 ± 8 ng/mg protein and 172 ± 11 ng/mg protein respectively (Fig. 2D). Thus, the cellular delivery of curcumin through gelatin-pluronic nanoparticles decreased with decreasing HLB value. The cytotoxic effect at the end of 48 hrs of treatment of bare nanoparticles and their corresponding curcumin loaded nanoparticles in A549 cells showed that the treatment of bare gelatin-pluronic nanoparticles per se caused cytotoxicity in a HLB dependent manner. The gelatin-pluronic nanoparticles of HLB 22 and HLB 8 exhibited the lowest (~2%) and highest (15%) cytotoxicity respectively. Further, in comparison to bare nanoparticles, curcumin loaded gelatin-pluronic nanoparticles showed higher cytotoxicity. This is expected considering that curcumin is a well-established anticancer agent and has been shown to reduce the viability of A549 cells [20]. Notably after deducting the cytotoxicity of curcumin loaded gelatin-pluronic nanoparticles with those of corresponding bare nanoparticles, it was found

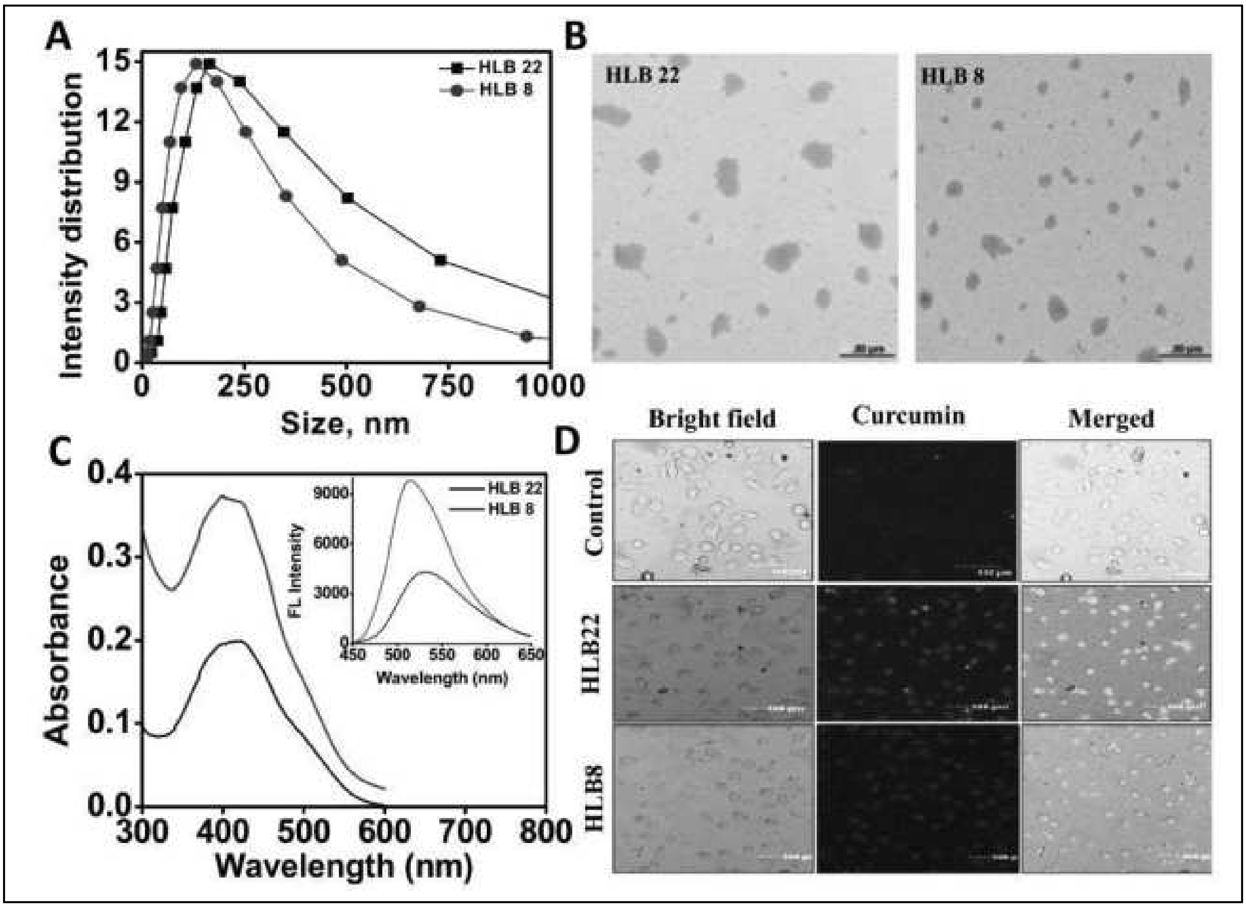

Figure 2: *Intensity correlation function of the gelatin nanoparticles (A) by DLS. TEM images (B) corresponds to the respective gelatin-pluronic nanoparticles of HLB 8 and 22. Plot (C) corresponds to absorption and fluorescence (inset) intensity of CUR (10 µM) loaded gelatin-pluronic nanoparticles. Plot D corresponds to laser scanning confocal microscopy images of A549 cells captured at 10× magnification using 488 nm laser following treatment with 12.5 µM of curcumin through different carriers (HLB 8 and HLB 22).*

that the ability of curcumin to kill A549 cells was reduced with decreasing HLB of nanocarriers which could be attributed to the reduced uptake of curcumin as observed previously. The lower cellular uptake of nanoparticles with decreasing HLB was due to their hydrophobic interaction with cell membrane hampering/slowing their penetration within cells. Thus, HLB of Pluronic was found to be an important parameter to be considered for designing gelatin-based nanocarriers and the nanoparticles having HLB of 22 were found to be biocompatible for maximum cellular uptake. Based on these results, the utility of gelatin-F127 (HLB 22) nanoparticles for drug delivery application was investigated using doxorubicin hydrochloride (Dox) as a model anticancer drug [15]. Dox is a broad-spectrum anticancer drug used in the treatment of several types of cancer [21]. The therapeutical application of Dox is limited due to its maximum uptake in a non-target organ, heart leading to cardiotoxicity. Gelatin-F127 nanoparticles showed high encapsulation efficiency of Dox (85%), a sustained acidic pH responsive release profile, and substantial cellular internalization. Additionally, Dox loaded nanocarriers (G-Dox) exhibited prolonged residence in blood as evidenced by their longer circulation time as compared to plain Dox. Moreover, G-Dox exhibited a higher availability of the drug in plasma as compared to nonspecific organs such as the heart, liver and kidneys, highlighting its significance in reducing drug associated side effects. Finally, the enhanced toxicity of G-Dox to a WEHI-164 (fibrosarcoma) tumor model as compared to that of plain Dox under an identical dosage of 6 mg per kg body weight (IP) confirmed its potential for chemotherapy application. In another similar study, the ability of the gelatin based nanocarriers for target specific delivery was also tested [16]. For this, folic acid was conjugated with gelatin followed by nanoprecipitation in presence of polysorbate 80 to form folate attached gelatin nanoparticles (GNP-F) of ~200 nm size. These nanoparticles were loaded with irinotecan (IRI), another broad-spectrum anticancer with the loading efficiency of 11.2 ± 0.73%. The IRI loaded gelatin-folate (IRI-GNP-F) formulation exhibited faster release of IRI at acidic pH (~5) than at physiological pH (~7). Further IRI-GNP-F demonstrated significantly higher cytotoxicity in folate receptor (FR)-positive HeLa cells than the unconjugated IRI-GNP nanoparticles confirming active targeting. Subsequently, the antitumor activity of above formulations in FR-positive fibrosarcoma (syngeneic) tumor-bearing mice followed the order of IRI-GNP-F > IRI-GNP > free IRI. The pharmacokinetic study indicated that encapsulation of IRI within folate conjugated of GNP remarkably improved its circulation half-life ($t_{1/2}$). Thus, above studies together supported the utilization of gelatin based nanoparticles for both passive and active targeting [15,16].

4. Conclusions

In conclusion, our studies report the synthesis and characterisation of novel protein nanoparticles from biocompatible proteins such as albumin and gelatin with tunable particle size of 20-250 nm of spherical morphology. The drug delivery applications of albumin and gelatin nanoparticles were optimised using curcumin as a payload. The results established that the particle size of ~125 nm and HLB of ~22 is optimal to achieve maximum intracellular delivery of payload through albumin and gelatin based nanocarriers respectively. Lastly, the synthetic methodology was extended to design the passive and actively targeted formulations of well-established anticancer drugs such as Dox and IRI which showed improved circulation half-life as well as efficacy as compared to plain drugs in mice models.

5. Acknowledgements

The research work presented in the manuscript is a part of doctoral thesis to be submitted by Mr. R.P. Das to Homi Bhabha National Institute. We acknowledge all the co-authors and collaborators of our published papers cited in the references. We thank Dr. Awadhesh Kumar, Head, RPCD and Dr. A. K. Tyagi, Director, Chemistry group, BARC, India, for their encouragement and support.

References

1. Sun, T.; Zhang, Y. S.; Pang, B.; Hyun, D. C.; Yang, M.; Xia, Y. *Angew. Chem. Int. Ed.,* **2014**, *53*, 12320-12364.
2. K.S. Soppimath, T.M. Aminabhavi, A.R. Kulkarni, W.E. Rudzinski, Biodegradable polymeric nanoparticles as drug delivery devices, J. Control Release 70 (2001) 1-20.
3. M. Jahanshahi, Z. Babaei, Protein nanoparticle: a unique system as drug delivery vehicles, Afr. J. Biotechnol. 7 (2008) 4926-4934.
4. H. Niknejad, R. Mahmoudzadeh, Comparison of different crosslinking methods for preparation of Docetaxel-loaded albumin nanoparticles, Iran J. Pharm. Res. 14 (2015) 385-394.
5. J.E. Ali, D. Siavoush, D. Soodabeh, A simple improved desolvation method for the rapid preparation of albumin nanoparticles, Int. J. Bio. Macromolecules 91 (2016) 703-709.
6. B. Manickam, R. Sreedharan, M. Elumalai, Genipin' – The Natural Water-Soluble Cross-linking Agent and Its Importance in the Modified Drug Delivery Systems: An Overview, Curr. Drug Deliv. 11 (2014) 139-145.
7. R.P. Das, B.G. Singh, A. Kunwar, M.V. Ramani, G.V. Subbaraju, P.A. Hassan, K.I. Priyadarsini, Tuning the binding, release and cytotoxicity of hydrophobic drug by Bovine Serum Albumin nanoparticles: Influence of particle size, Colloids Surf. B 158 (2017) 682-688.
8. R.P. Das, V.V. Gandhi, B.G. Singh, A. Kunwar, N.N. Kumar, K.I. Priyadarsini, Preparation of albumin nanoparticles: Optimum size for cellular uptake of entrapped drug (Curcumin), Colloids Surf. A, 567 (2019) 86-95.
9. R.P. Das, B.G. Singh, A. Kunwar, K.I. Priyadarsini, Interaction of a model hydrophobic drug dimethylcurcumin with albumin nanoparticles, Protein J. 38 (2019) 649-657.
10. A.M. Merlot, D.S. Kalinowski, D.R. Richardson, Unraveling the mysteries of serum albumin more than just a serum protein, Front. Physiol. 5 (2014) 299-305.
11. A.O. Elzoghby, Gelatin-based nanoparticles as drug and gene delivery systems: Reviewing three decades of research, J. Control Release 172 (2013) 1075-1091.
12. P. Anand, A.B. Kunnumakkara, R.A. Newman, B.B. Aggarwal, Bioavailability of curcumin: problems and promises, Mol. Pharm. 4 (2007) 807-818.
13. M. Teymouri, N. Barati, M. Pirro, A. Sahebkar, Biological and pharmacological evaluation of dimethoxycurcumin: a metabolically stable Curcumin analogue with a promising therapeutic potential, J. Cell Physiol. 233 (2016) 124-140.
14. R.P. Das, V.V. Gandhi, B.G. Singh, A. Kunwar, Balancing loading, cellular uptake and toxicity of gelatin-pluronic nanocomposite for drug delivery: Influence of HLB of pluronic, J. Biomed. Mater. Res. A 110 (2021), 1-12.
15. R.P. Das, B.G. Singh, A. Kunwar, Preparation of a size selective nanocomposite through temperature assisted co-assembly of gelatin and pluronic F127 for passive targeting of Doxorubicin, Biomater. Sci. 8 (2020), 4251.
16. R.P. Das, S. Chakravarti, S.S. Patel, P. Lakhamje, M. Gurjar, V. Gota, B.G. Singh, A. Kunwar, Tuning the pharmacokinetics and efficacy of irinotecan (IRI) loaded gelatin nanoparticles through folate conjugation, Int. J. Pharm. 586 (2020) 119522.
17. V.K. Rapalli, V. Kaul, S. Gorantla, T. Waghule, S.K. Dubey, M.M. Pandey, G. Singhvi, UV Spectrophotometric method for characterization of curcumin loaded nanostructured lipid nanocarriers in simulated conditions: Method development, in-vitro and ex-vivo applications in topical delivery, Spectrochim. Acta A Mol. Biomol. Spectrosc. 224 (2020) 117392.
18. C.A. Haskard, E.C.Y. Li-Chan, Hydrophobicity of bovine serum albumin andovalbumin determined using uncharged (PRODAN) and anionic (ANS) fluorescent probes, J. Agric. Food Chem. 46 (1998) 2671-2677.
19. S.M. Khopde, K.I. Priyadarsini, D.K. Palit, T. Mukherjee, Effect of solvent on the excited-state photophysical properties of curcumin, Photochem. Photobiol. 72 (2000) 625-631.
20. F. Liu, S. Gao, Y. Yang, X. Zhao, Y. Fan, W. Ma, D. Yang, A. Yang, Y. Yu, Antitumor activity of curcumin by modulation of apoptosis and autophagy in human lung cancer A549 cells through inhibiting PI3K/Akt/mTOR pathway. Oncol. Rep. 9 (2018) 1523-1531.
21. N. Zhao, M.C. Woodle and A.J. Mixson, Advances in delivery systems for doxorubicin, J. Nanomed. Nanotechnol. 9 (2018) 519-528.

About the authors

Mr. Ram Pada Das *obtained his M.Sc. degree from IIT Kanpur in Chemical Sciences in 2013 and joined Radiation & Photochemistry Division after graduating from the 58th batch of training school (Chemistry) in August 2015. His research interests focus on the implementation of vision programme (V8 & V4) on the development of cost effective novel anticancer formulations employing photo-physical and biochemical techniques.*
Email: rpdas@barc.gov.in

Dr. Beena G. Singh *received her PhD in Chemistry from University of Mumbai in 2007 and joined BARC as K. S. Krishnan Research Associate. Her current research interest focuses on investigating the role of redox processes in synthetic and natural compounds for the radioprotection and anti-cancer activity. She is the recipient of Carl Storm International Diversity Award from the organizers of Gordon Research Conference in Radiation Chemistry, 2012 and Scientific & Technical Excellence Award from Department of Atomic Energy, 2015.*
Email: beenam@barc.gov.in

Dr. Amit Kunwar *joined Radiation & Photochemistry Division, BARC in 2005 after graduating from BARC Training School (48th Batch, Bioscience discipline). After completing Ph.D. from Homi Bhabha National Institute in 2010, he received "Richard and Edith Strauss Postdoctoral Fellowship in Respiratory Medicine" to pursue postdoctoral research at Meakins Christie Laboratories, McGill University, Montreal, Canada, 2012-2014. He is the recipient of "Outstanding Doctoral Thesis Award" from Homi Bhabha National Institute, "Young Scientist Award" from DAE, "Young Scientist Award" for outstanding contribution in field of cancer research from "Indian Academy of Biomedical Sciences.*
Email: kamit@barc.gov.in

Laser Spectra Services India Pvt. Ltd,Bangalore

A Crucial Support System for the Scientific Community

Newport
Experience | Solutions

Spectra-Physics
A Newport Corporation Brand

ORIEL INSTRUMENTS
A Newport Corporation Brand

DPSS Lasers, CW Ti:Sapphire Lasers, Mode Locked Ti:Sapphire Lasers, Nanosecond OPO System, Pulsed Dye Lasers, UltrafastAmplifier System, He-Ne Laser, Diode Laser, Fiber Laser, Femto Second Fibre Laser, Ultrafast Oscillator System, Optical Parametric Amplifier System etc.. Solar Simulators, IQE-EQE System, IV-Test Stations, Band passFilters, Gratings, Light Sources, Optics, Vibration Isolation Tables,Optics & Opto-Mechanical Components

Raman Spectrometers: HORIBA Scientific

LabRAM HR Evolution-High spectral resolution analytical Raman microscope
XploRA Series (XploRA+, XploRA ONE & XploRA INV)-Simple Better Raman
MACRORAM Benchtop Raman Spectrometer

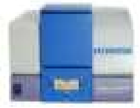

Fluorescence Lifetime, Spectroscopic Ellipsometers, Surface Plasmon Resonance Systems, Spectrometers & Detectors

Aqualog® - Compact, **DeltaFlex, DeltaPRO** -TCSPC Lifetime System(ns, ps & μs lifetime).

Nano second lasers from Amplitude (Continuum)

Amplitude

Laser-Spectra Services India Pvt. Ltd,
8, Second Floor, 80 ft Double Road, RMV 2nd Stage(HIG),Bangalore-560 094.
☎:+91-80-23576907 @ admin@laser-spectra.com **www.laser-spectra.com**

Quality Manufacturing Company

Product Portfolio

We are a reckoned manufacturer, supplier and marketeer of Optical Mounts and Special Purpose Machines. Our products are manufactured from quality raw material sourced from trusted vendors in association with us.

Address : 5 OSHIWARA LANE , S V ROAD SUBHASH ESTATE,
Jogeshwari West, Mumbai-400102, Maharashtra, India

Contact : Jaimin Shah (Manager) - +91 9324484838

Interaction of fluorescein and giant unilamellar vesicles: Exploring the photophysical heterogeneity by fluorescence lifetime imaging microscopy

Ashutosh Ghosh[a,b] and Pradipta Purkayastha[a]*

[a]*Department of Chemical Sciences, Indian Institute of Science Education and Research (IISER) Kolkata, Mohanpur 741246, WB, India.*
[b]*Salua Academy, Goalsalua, Ranaghat 741501, WB, India.*
**Corresponding author*
**Email: ppurkayastha@iiserkol.ac.in*

Abstract

Fluorescein (FL) exists in several prototropic forms depending on the pH of the medium. It is reported theoretically that the fluorescence intensity of FL depends upon the local pH, which, in turn, is sensitive to the local electrostatic potential in the vicinity of the probe-generated by the lipid head-group dipole orientation. Interaction of FL with lipid bilayer indicates that distribution of FL in giant unilamellar vesicles (GUVs) is very heterogeneous. This fundamental work focusses upon exploring the heterogeneity in the distribution of FL on interaction with GUVs formed by the zwitterionic lipids molecules of 1,2-Dipalmitoyl-rac-glycero-3-phosphocholine (DPPC).

1. Introduction

The spatial distribution of excited state lifetimes of fluorescent materials is determined by fluorescence lifetime imaging microscopy (FLIM), typically in the nanosecond regime considering the fluorescence lifetimes of most fluorophores.[1,2]A typical FLIM instrument uses an intensity-modulated or pulsed radiation for excitation and measures the time-resolved fluorescence emission. Fluorophore which are typically used in biomedical applications bear lifetimes ranging from 1 to 10 ns, which led to the development of most frequency-domain FLIM instruments operating between 10 and 100 MHz.[3] In time-domain measurements, time correlated single photon counting (TCSPC) technique is used where one monitors the arrival time of the first photon after each pulse at very high time resolution.[4] The microscope is generally equipped with a pulsed light source (a pulsed laser) to perform FLIM in the time-domain detection.

FLIM is uniquely advantageous compared to the conventional intensity-based fluorescence microscopy. While, intensity alone cannot discriminate fluorophore with spectral similarity, fluorescence intensity imaging can significantly provide information on their spatial distribution and can identify fluorophores with distinct spectral properties since it deals with the photon count.[2] Hence, FLIM is exceptionally advantageous in identifying changes in the molecular milieus and understand the fluorophore function and behaviour.[5] Because of its uniqueness, FLIM is largely independent of fluorophore concentration and hence can identify the reason for the change in fluorescence intensity, which could be due to changes in quantum yield, or the overall fluorophore concentration, or both.

FLIM measurements are much less affected by the inner filter effects.[6,7]

The usefulness of FLIM over conventional microscopy or ensemble level time-resolved measurements has tempted us to explore the photophysical heterogeneity induced by the molecular environment once a fluorophore interacts with bio-mimicking system, such as, the liposomes. For this study, we chose fluorescein (FL), which is an important xanthene dye with a large variety of applications. The high absorbance in the visible region of the spectrum and high fluorescence quantum yield has made it useful in conjugation to functional biomolecules. Hence, FL is widely used as fluorescence marker in biosciences.[8-10] In all the applications, it has been observed that the surrounding environment dictates the photophysical properties of FL and its derivatives. They typically exist in different structural forms in different media and hence give varied absorption spectra, fluorescence spectra, quantum yields and lifetimes, responding to the various pH,[11,12] strength of hydrogen bonding,[13] and polarity[14]of the environment.

Depending on the pH of the medium, FL exists in several prototropic forms (Scheme 1).[15] The carboxyl phenyl in FL is almost perpendicular to the xanthene ring,[16] and therefore is not conjugated to the xanthene group. Thus, the ionization and alkylization of the carboxyl is not expected to influence the absorption spectrum in the visible region. The ionic forms of FL are easily soluble in water whereas the neutral form is sparingly soluble. The easily aqueous soluble anionic FL does not bind to anionic surfactants but readily binds to the cationic ones.[17] Interaction of FL with lipid bilayer and hence the effect on its properties

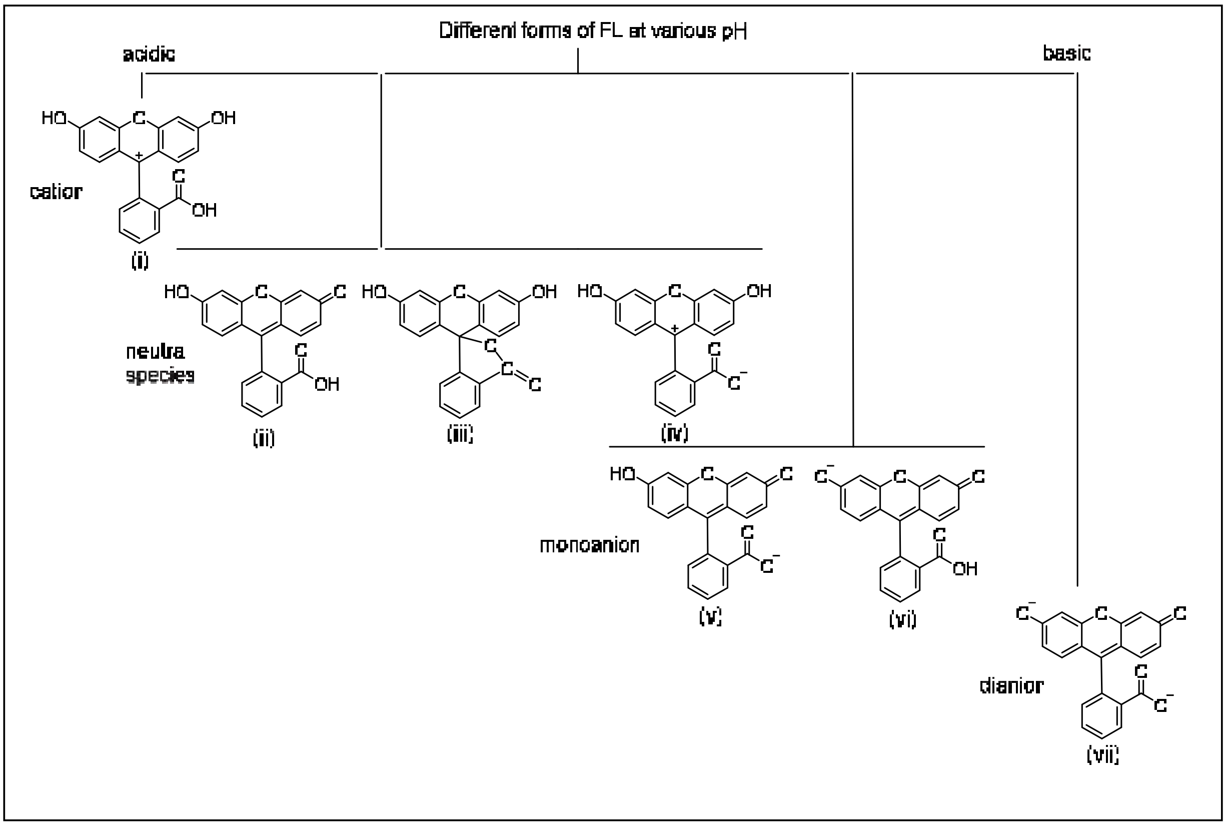

Scheme 1: *Different structural forms of FL.*

have also been studied. It was reported theoretically that the fluorescence intensity of FL depends upon the local pH, which, in turn, is sensitive to the local electrostatic potential in the vicinity of the probe generated by the lipid head-group dipole orientation.[18] This indicates that distribution of FL at the membrane and inside the aqueous pool of lipid vesicles may vary the characteristic properties of FL. Elaborate study in this aspect is important as FL bound lipid membranes are widely used in biological research.[19,20] Here, we have thus focussed our study on exploring the heterogeneity in the distribution of FL on interaction with giant unilamellar vesicles (GULVs) formed by the zwitterionic lipids molecules of 1,2-Dipalmitoyl-rac-glycero-3-phosphocholine (DPPC).

2. Experimental section

Materials

Fluorescein (FL) and 1,2-Dipalmitoyl-rac-glycero-3-phosphocholine (DPPC) were purchased from TCI Chemicals (India) Pvt. Ltd. A 1.21 mM stock solution of FL was prepared in methanol. High purity water was used throughout the experiment. The experiment was done in Tris buffer (pH 7.5).

Synthesis of giant unilamellar vesicles (GUVs)

The GUVs were prepared as reported elsewhere.[20] Briefly, a weighed amount (0.8 mg) of DPPC was dissolved in chloroform (0.1 M) and 20 μL of this solution was added to a mixture of 980 μL of chloroform and 100−200 μL of methanol. The aqueous phase (5 mL of Tris buffer) was then carefully added along the walls of the flask. The organic solvent was removed by a rotary evaporator under reduced pressure (60 mm Hg) at 40 °C and 40 rpm. Due to the different boiling points of chloroform (61 °C) and methanol (64 °C), we observed two major boiling events. After evaporation for about 2 min, an opalescent solution was obtained containing a high concentration of GUV. The diameter of the GUVs is calculated to be ~40 μm as obtained from FLIM.

Methods

The absorption and emission spectra were collected using a U-2900 spectrometer from Hitachi and a QM-40 spectrofluorimeter from

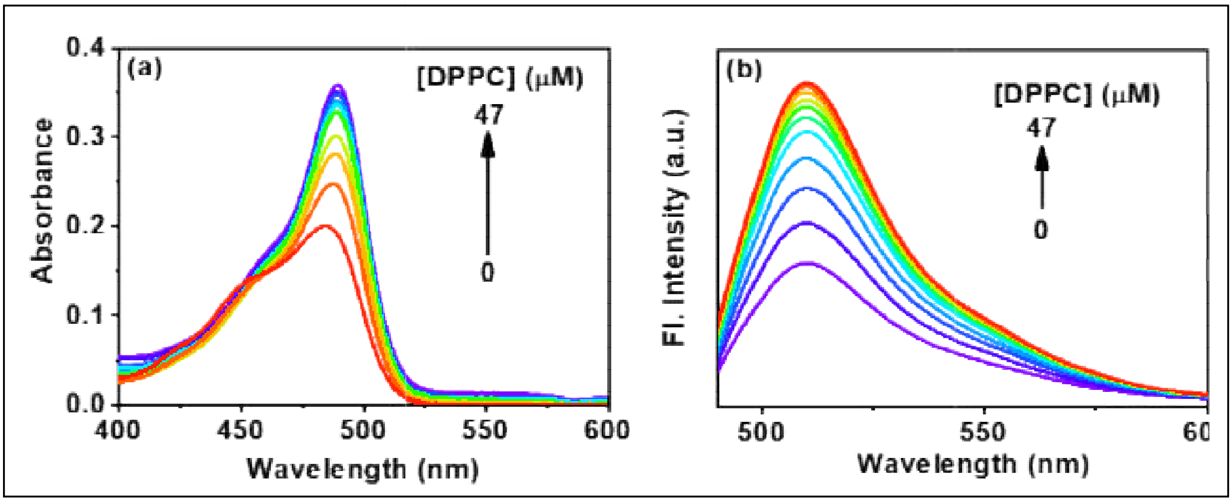

Figure 1: *(a) Absorption and (b) fluorescence spectra of FL with gradual addition of the DPPC GUVs. The inset shows deconvoluted emission spectrum of FL. Concentration of FL is 3.02 μM. The sample was excited at 484 nm.*

PTI, respectively. All the slit widths used for measurements with U-2900 and QM-40 spectrometers were 0.7 mm. The excitation wavelength was 484 nm. The time-resolved fluorescence measurements were performed by the time-correlated single-photon counting (TCSPC) technique in a spectrometer from Horiba Jobin Yvon using a 405 nm NanoLED-03 (temporal pulse width <70 ps) as the excitation source and a TBX-04 photomultiplier detector (IBH). From the measured decay traces, the lifetimes were analysed using IBH DAS-6 decay analysis software.

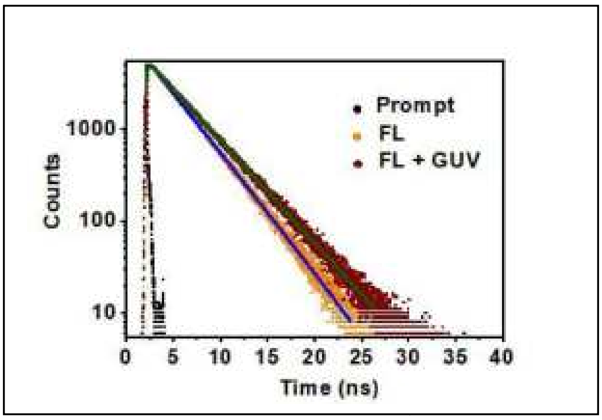

Figure 2: *Time resolved fluorescence profiles of FL in the absence and presence of GUVs constituted by 47 µM DPPC.*

The FLIM studies were carried out with a confocal laser scanning microscope (Axio Observer A1) from Zeiss coupled with a DCS-120 system from Becker & Hickl (BH) GmbH for fluorescence lifetime imaging and a picosecond diode laser (BDL-488-SMC, BH) with λ_{ex} = 488 nm. The scanning was controlled by a BH GVD-120 scan controller. The BH HPM-100-40 hybrid detector module in the DCS120 system was controlled by DCC-100 software. A long pass filter (HQ495LP) was placed to block the excitation light and a narrow band-pass filter of 525−550 nm (HQ525/50) was used to monitor the emission. The TCSPC FLIM system is controlled by the "SPCM" TCSPC operating software and by the software of the DCC-100 detector controller. The emitted light from a selected point of the sample was collected by the microscope lens, scanned by the galvanometer mirrors, separated from the excitation beam, split into two channels of different wavelengths, and focused into pinholes in a plane conjugate with the focal plane in the sample. Out-of-focus light was thus suppressed. The FLIM images were analysed in SPC Image software for decay measurement at a particular point of the sample.

3. Results and discussion

Steady state spectroscopic results for interaction of FL with DPPC

The absorption spectrum of FL in Tris buffer (pH 7.5) shows two bands at 450 and 485 nm (Figure 1a). The neutral forms of FL (ii, iii, iv) have lower wavelength absorption and the monoanionic forms (v, vi) absorb at higher wavelengths.[21] The neutral FL has a much lower absorption intensity than the other forms due to the formation of the lactonic modification (iii), which does not absorb in the

Table 1. *Lifetime decay data of FL in presence and absence of DPPC GUVs. Values in parentheses indicate the respective percentage contributions and the χ^2 values show the goodness of the fits. The lifetime values are within 2-5% error limit.*

System	τ_1 (ns)	τ_2 (ns)	χ^2
FL	0.15 (-2)	3.37 (102)	1.03
FL + 47 µM GULV	0.16 (-2)	3.93 (102)	1.00

visible region.[21] This indicates that FL exists partly in the zwitterionic form (iv), which is expected to have the same spectrum as the cation, and as the quinonoid form (ii) that exhibits monoanion absorption.[21] The absorbance of the monoanionic form increases with increase in concentration of the DPPC vesicles indicating solubilisation of the fluorophore. The neutral form, being sparingly soluble in water, will stay in the lipid bilayer and the monoanionic form will move into the aqueous core due to enhanced solubility. The fluorescence emission spectrum of FL also shows two bands: the more intense band appears at 510 nm and a very weak shoulder at 545 nm (Figure 1b). These bands are due to the monoanionic and the neutral forms, respectively. With gradual addition of DPPC in the form of GUVs, the band for the monoanionic form increases in intensity. This could be due to the conversion of the monoanionic form to the dianionic form in the excited state, which can be confirmed from the time resolved fluorescence decay measurements.

Time resolved fluorescence spectroscopy to consolidate the nature of interaction

The time dependent fluorescence profiles of FL in absence and presence of the GUV fit biexponentially indicating existence of two different species or events in solution (Figure 2). The fit data show a rise component along with the decay on monitoring at 510 nm wavelength (Table 1). The rise component indicates the occurrence of an excited state event in FL which is supposed to be the deprotonation of the monoanion to yield the dianion. The decay time slows down in presence of GUV indicating longer lifetime of the dianion in the excited state.

Fluorescence lifetime imaging microscopy (FLIM) studies to observe the heterogeneity of FL in the GULVs

The FLIM image of the FL incorporated DPPC GUV shows the inner water pool of the GULV where distribution of FL can clearly be seen (Figure 3). The colour code indicates distribution of FL in the aqueous pool and the decay time varies with the position of the dye. In has been observed that the green-coded and orange-coded FL molecules have single-exponential decay in 3.19 and 1.59 ns, respectively. The blue-coded FL molecules fit with a double exponential routine and the lifetimes are 1.01 and 3.24 ns. The fastest decaying components are mainly populating the interior of the water pool and hence presumably the signals are from the dianions. The green coded ones are towards the lipid-water interface and hence showing decay mainly from the monoanions. The blue-coded molecules mostly exist slightly below the interface and hence

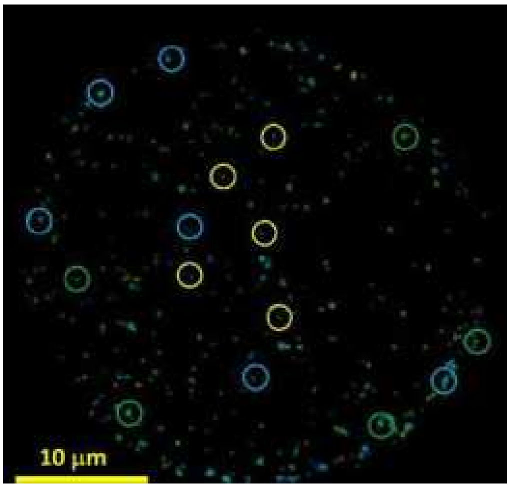

Figure 3: *FLIM image of an FL-incorporated DPPC GULV. Concentrations of FL and DPPC were 10 μM and 47 μM, respectively. The excitation wavelength is 488 nm. The yellow, blue and green circles are indicating the orange, blue and green signals in the image.*

exhibit the existence of monoanion and the dianions.

4. Conclusions

It has been shown that the different protropic forms of FL readily interact with GUVs formed from DPPC. The sparingly soluble neutral forms and the monoanionic forms generally absorb the radiation. The monoanionic form converts to the dianions in the excited state due to loss of one proton from the FL monoanion. The FLIM image of the GUV shows distribution of FL at the interface and in the aqueous interior of the GUV. They show heterogeneity in their molecular characteristics as indicated by the location specific excited state lifetimes of the distributed FL molecules. The studies provide a clear idea on the nature of existence of FL in biological cellular environment in the excited state.

Acknowledgements

The authors acknowledge KVPY and IISER Kolkata for the financial and infrastructural support.

References

1. van Munster, E. B.; Gadella, T. W. J. Fluorescence Lifetime Imaging Microscopy (FLIM). *Adv. Biochem. Engin. Biotechnol.***2005**, *95*, 143–175.
2. Datta, R.; Heaster, T. M.; Sharick, J. T.; Gillette, A. A.; Skala, M. C. Fluorescence Lifetime Imaging Microscopy: Fundamentals and Advances in Instrumentation, Analysis, and Applications. *J. Biomed. Opt.***2020**, *25*, 071203.
3. Squire, A.; Verveer, P. J.; Bastiaens, P. I. Multiple Frequency Fluorescence Lifetime Imaging Microscopy. *J. Microsc.***2000**, *197*, 136-149.
4. O'Connor, D. V.; Phillips, D. In: Time-Correlated Single Photon Counting, 1984, Academic Press: New York.
5. Becker, W. In: The BH TCSPC Handbook, 8th Ed., Becker et Hickl, Berlin: Germany, 2019.
6. Glasgow, B. J. Fluorescence lifetime imaging microscopy reveals quenching of fluorescein within corneal epithelium. *Exp. Eye Res.***2016**, *147*, 12–19.
7. Lakowicz, J. R. In: Principles of Fluorescence Spectroscopy, 3rd Ed., Springer Science & Business Media, Boston: Massachusetts, 2013.
8. Stanton, S. G.; Kantor, A. B.; Petrossian, A.; Owicki, J. C. Location and dynamics of a membrane-bound fluorescent hapten. A spectroscopic study. *Biochim. Biophys. Acta***1984**, *766*, 228-236.
9. Graber, M. L.; Dilillo, D. C.; Friedman, B. L.; PastorizaMunoz, E. Characteristics of fluoroprobes for measuring intracellular pH.*Anal. Biochem.***1986**, *156*, 202.
10. Klonis, N.; Clayton, A. H. A.; Voss Jr., E. W.; Sawyer, W. H. Spectral properties of fluorescein in solvent- water mixtures: applications as a probe of hydrogen bonding environments in biological systems. *Photochem. Photobiol.***1998**, *67*, 500-510.
11. Diehl, H.; Markuszewski, R. The fluorescence of fluorescein as a function of pH.*Talanta***1989**, *36*, 416-418.
12. Martin, E.; Pardo, A.; Guijarro, M. S.; Fernandez-Alonso, J. I. Photophysic

properties of fluorescein in alcohol medium for different pH.*J. Mol. Struct.***1986**, *142*, 197-200.

13. Zeng, H.-H.; Wang, K.-M.; Yang, X.-H.; Yu, R.-Q. Fibre-optic sensor for the determination of carboxylic acids based on fluorescence enhancement of lipophilized fluorescein isologues. *Anal. Chim. Acta***1994**, *287*, 267.
14. Song, A.; Wu, T.; Chen, S.; Zhang, M.; Shen, T. Syntheses and photophysical properties of amphiphilic dyads of fluorescein and carbazole linked with a flexible or semi-rigid bridge. *Dyes Pigm.***1998**, *39*, 371-382.
15. Panchompoo, J.; Aldous, L.; Baker, M.; Wallace, M. I.; Compton, R. G. One-step synthesis of fluorescein modified nano-carbon for Pd(ii) detection via fluorescence quenching. *Analyst***2012**, *137*, 2054-2062.
16. Osborn, S.; Rogens, D. The crystal and molecular structure of the 1: 1 complex of acetone with the lactoid form of fluorescein. *Acta Crystallogr. Sect. B***1975**, *31*, 359-364.
17. Song, A.; Zhang, J.; Zhang, M.; Shen, T.; Tang, J. Spectral properties and structure of fluorescein and its alkyl derivatives in micelles. *Coll. Surf. A***2000**, *167*, 253-262.
18. Kubica, K.; Langner, M.; Gabrielska, J. The dependence of Fluorescein-PE fluorescence intensity on lipid bilayer state. Evaluating the interaction between the probe and lipid molecules. *Cell. Mol. Biol. Lett.***2003**, *8*, 943-954.
19. Ahlers, M.; Grainger, D. W.; Herron, J. N.; Lim, K.; Ringsdorf, H.; Salesse, C. Quenching of fluorescein-conjugated lipids by antibodies. Quantitative recognition and binding of lipid-bound haptens in biomembrane models, formation of two-dimensional protein domains and molecular dynamics simulations. *Biophys. J.***1992**, *63*, 823-838.
20. Ghosh, P.; Das, T.; Maity, A.; Purkayastha, P. Light induced dynamics of a charge transfer probe in lipid vesicles. *Soft Matter***2012**, *8*, 10178-10182.
21. Martin, M. M.; Lindqvist, L. The pH dependence of fluorescein fluorescence. *J. Lumin.***1975**, *10*, 381-390

About the authors

Ashutosh Ghosh *earned his Ph.D. degree from the Indian Institute of Science Education and Research (IISER) Kolkata in 2020. He worked under the supervision of Prof. Pradipta Purkayastha of the Department of Chemical Sciences. He is presently working as a teacher in Salua Academy, Ranaghat, West Bengal, India.*

Pradipta Purkayastha *is a professor in the Department of Chemical Sciences at the Indian Institute of Science Education and Research (IISER) Kolkata, India. He earned his Ph.D. from Jadavpur University in 2002 and did his post-doctoral research at the University of Pennsylvania, USA. He is a fellow of the Royal Society of Chemistry and the West Bengal Academy of Science and Technology. His area of research includes studies of the ultrafast dynamics of small molecules in biocompatible and heterogeneous environments and development of fluorescent nanomaterials for energy applications.*

Super-resolved Microscopy using Defocused Orientation and Position Imaging: Dye Binding to Amyloid Fibrils

Aranyak Sarkar[a,b], Sonali Gupta[b], Vinu Namboodiri[a] and Manoj Kumbhakar[a,b]*
[a]*Radiation & Photochemistry Division, Bhabha Atomic Research Center, Mumbai 400085, INDIA*
[b]*Homi Bhabha National Institute, Training School Complex, Anushaktinagar, Mumbai 400094, INDIA*
**Email: manojk@barc.gov.in*

Abstract

In and around past one decade, single molecule microscopy has emerged as an elegant technique in the field of bio-imaging. Single molecule detection can remove the complexity associated with ensemble measurements techniques as it carries more information about the molecule than the average measurement. Single molecule localization microscopy achieves super-resolution by isolating individual emitters by fitting the focused image with appropriate point spread function (PSF). By slightly defocusing the image, the recorded radiation emission pattern depends both on the localization as well as the orientation of the dipole emitter. The present paper discusses this method for accurate determination of position as well as orientation of individual emitters using defocused orientation and position imaging (DOPI). We have used a home build setup for single molecule detection, to see orientation of oscillating dipoles, i.e. dye molecules, when bound to hen egg white lysozyme (HEWL) fibril.

1. Introduction

Proteins are complex macromolecules which are essential components of biological functioning of all living organism. Amyloidosis is the diseases caused by formation of water insoluble amyloid by denaturation of the native proteins & aggregation. This amyloid fibril shares some common morphological feature but the native protein does not conserve its native structural motif. Hen egg white lysozyme (HEWL) being very close to human lysozyme is a most studied protein and also shows formation of amyloid fibril in vitro. This HEWL amyloid fibril formation study gives the idea about the mechanism of amyloid fibril formation which may well be related with diseases causing amyloid fibril. Although, different proteins result in formation of different amyloid fibrils but despite of different amino acid sequencing they share very similar morphological structure, mainly the cross β-sheet running perpendicular to fibril axis and having hydrogen bonds between N-H and carbonyl group of amino-acid parallel to the long fibril axis. A large number of studies employing a range of techniques have helped to understand the physico-chemical and structural arrangements of fibril formation. There are great efforts to even develop better fluorogenic probes for sensing amyloid fibrils for research as well as diagnostic applications. Several sensitive and specific amyloid-binding dyes have been extensively used to study the aggregation of proteins into amyloid fibrils in vitro and here, we are interested in exploring their binding to fibril structures for sensing action.

In this project we attempted to explore the dye binding sites on fibrils and the orientation of dye dipole when bound to HEWL fibrils using single molecule localization microscopy (SMLM) and orientation imaging with home build single molecule imaging setups. SMLM[1-3] describes a family of powerful imaging techniques that dramatically improve spatial resolution over standard, diffraction-limited microscopy techniques and can potentially image biological structures at the molecular scale. In SMLM, individual fluorescent molecules are computationally localized from diffraction-limited image sequences and the localizations are used to generate a super-resolution image or a time course of super-resolution images. SMLM uses varieties of techniques for accurately determining the position of fluorophores. Most of these techniques involve deconvolution of the images to identify individual emitters and fitting the deconvoluted image with appropriate point spread function.[3] Techniques such as fluorescence imaging with one nanometer accuracy (FIONA) have shown to be useful for determining the position with nanometer accuracy.[4]

But, most of the biological and chemical processes involve translational as well as rotational motion of molecules. In order to gain a deeper understanding about function of molecules and its immediate environment, it is desirable to have an understanding about both the position and orientation of single molecules. By moving the sample towards or away from the focus of a microscope, the recorded dipolar emission patterns, i.e. angular distribution of intensity projection, become dependent on both the position as well as the orientation of the emitter.[5-7] By using the fact that emission patterns for dipoles oriented in different orientations are different and by using appropriate pattern matching methods for fitting the resultant defocused emission patterns, information can be deduced about the position and orientation of the emitters. This method, known as defocused orientation and position imaging (DOPI),[8] is applied to determine the position and orientation of Rhodamine B (RhB) dye dissolved in poly vinyl alcohol as reference and then applied with a hydrophobic dye in presence of fibril structures. To demonstrate, we use a form of SMLM termed transient amyloid binding (TAB)[9, 10] of fluorescent molecules transiently bound to amyloid fibrils. We detect the fluorescence photons of Nile Red (NR), whose quantum yield increases significantly when exposed to a nonpolar environment, i.e. when bound to fibrils at the single-molecule level. Nile red is an uncharged, heterocyclic dye which is soluble in organic solvents but has poor solubility in water.

2. Materials and Methods

The standard sample used is 1 pM RhB in 0.1% poly vinyl alcohol (PVA) spin coated on a glass substrate. The sample is excited with a 532 nm DPSS laser of circular polarization, using an inverted microscope with an objective of magnification 60X and 1.46 NA. The fluorescence emission at 550 nm is collected using the same objective and passed through a dichroic mirror to reject the excitation light and imaged on to a CCD camera (ANDOR, Newton) with pixel size 16 µm × 16 µm. The magnification of the imaging optics is chosen to be 200. The size of the pixel with this magnification corresponds to approximately 80 nm. The images are collected with 0.1 to 1 sec exposure times.

HEWL is known to form amyloid fibril under denaturing conditions such as in organic solvent, detergents in low pH at high temperature (37-90ºC). Fibrils were prepared following reported procedure,[11] as described briefly. A stock solution of HEWL containing 5mg/ml was prepared in Milli-Q water and then pH of this solution is adjusted to 1.0 using HCl. The solution is then incubated at 90^0C for 9 hours with continuous agitation by a stirrer at 300 rpm. After heating, solution is cooled down to room temperature and then stored at 4°C for further use. The prepared fibrils were appropriately diluted with water (pH ~7) and imaged using ~50 nM NR dye solution on cover slip using highly inclined excitation condition.

3. Dipole Orientation Imaging

The topic of special interest here is to experimentally determine the spatial orientation of the molecule's emission dipole. This information about orientation is important as single molecule orientation can itself be a probe for studying photophysics and the arrangement of the embedding environment/structure. Among different techniques for determining single-molecule orientations by fluorescence imaging, is the detection of angular distribution of a single-molecule's fluorescence emission pattern by deteriorating the image of the molecule by defined image defocusing. The intensity distribution of the blurred image contains information about the molecule's emission-dipole orientation. We used this concept to image surface-bound dyes on fibril using a conventional CCD-imaging epi-fluorescence microscope under laser wide-field illumination. This method is easy to implement and allows for fast screening of single-molecule dipole orientations. For analysis of large number of molecule orientations, a necessary pattern recognition algorithm has been used to localize single-molecule patterns within an image and determine their three-dimensional orientation even under noisy low-signal conditions.

The near-field coupling of an emitting electric dipole (fluorescing molecule) and a planar multilayered substrate is well reported in literature. In short, the emitting molecule is considered as an ideal oscillating electric dipole. To study the interaction of such a dipole with a planar structure, the emitted electromagnetic field of this dipole is mathematically represented by a superposition of plane waves. For each plane wave, the interaction with the planar substrate is calculated by using standard Fresnel theory, which in the end gives the desired full electromagnetic field of the emitter in the presence of the planar substrate. Finally, by integrating the Poynting vector of a given surface, one can then calculate the total energy flux of the emitted field through the given surface for detection onto CCDs.

3.1 Brief Theory of Defocused Imaging

A fluorescing molecule can be considered as a dipole emitter. The radiation pattern emanating from the molecular emission can be theoretically modeled using classical electrodynamics.[12, 13] **Figure 1** shows dipole

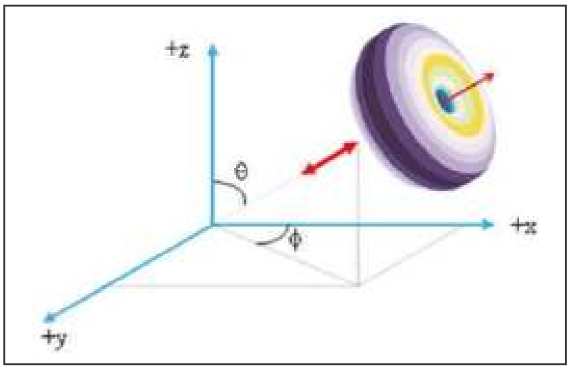

Figure 1: *Spherical coordinate system where optical axis is the z-axis,* θ *is the angle of the dipole relative to the optical axis* $(0 \leq \theta \leq 90°)$ *and* ϕ *is the azimuthal angle* $(0 \leq \phi \leq 360°)$. *This dipole on excitation emits electromagnetic field which is a 3D doughnut shape around the dipole, as a result of dipole oscillations. When this angular emission field was projected on a 2D detection plane (like CCD-imaging in epi-fluorescence microscope) gives specific intensity pattern for the dipole orientation, i.e. a particular valueof* θ *and* ϕ.

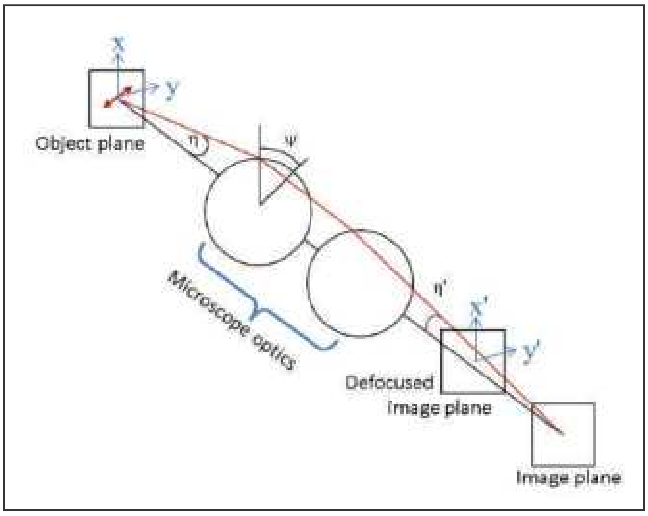

Figure 2: *Schematic for geometry of defocused imaging. The CCD camera is placed directly at the image plane of the optics while defocusing is done by either moving the objective towards the solution or by suitably placing the detector in defocused image plane in any wide-filed epi-fluorescence setup.*

(red double headed arrow) orientation in 3D space showing polar (θ) and azimuthal angles (ϕ). The radiation emitted by dipoles shows an angular distribution proportional to $\sin^2\theta$, where θ is the angle between the direction of observation and axis of the dipole.

The imaging geometry considered here is shown in **Figure 2**. The polar and azimuthal angles in the object frame are defined to be $\eta \,\&\, \psi$ and that in the laboratory frame are defined to be $\theta \,\&\, \phi$.

The angular distribution of the electric field emitted into the glass (considering only the far field emission) are given by[12, 14]

$$E(\eta,\psi) = \boldsymbol{e}_p\left[\cos(\theta)\,E_p^{\perp}(\eta) + \sin(\theta)E_p^{||}(\eta)\cos(\psi)\right] + \boldsymbol{e}_s\left[\sin(\theta)E_s^{||}(\eta)\sin(\psi)\right]$$

With

$$E_p^{\perp}(\eta) = \sin\eta\left[e^{-inz\cos\eta} + F_p(\eta)e^{inz\cos\eta}\right]$$

$$E_p^{||}(\eta) = \cos\eta\left[e^{-inz\cos\eta} \mp F_{p,s}(\eta)e^{inz\cos\eta}\right]$$

(- for p waves and + for s waves)

θ is the angle between the dipole axis and the optical axis. $\boldsymbol{e}_s$ and $\boldsymbol{e}_p$ are the unit vectors denoting the in-plane and out of plane polarization components of the electric field, $F_{s,p}(\eta)$ are the Fresnel reflection coefficients at the air/glass interface for the s and p waves and $\boldsymbol{n}$ is the refractive index of glass. After imaging the radiation pattern onto the CCD chip, the electric (E_j) and magnetic fields (B_j) on the chip can be determined by integration over the variable ψ.

$$\begin{Bmatrix}E_j\\B_j\end{Bmatrix} = \int_0^{\eta'_{max}} d\eta' \sin\eta' \sqrt{\frac{\cos\eta'}{n\cos\eta}} \begin{Bmatrix}e_j\\b_j\end{Bmatrix} e^{ik\delta z\cos\eta}$$

The angles η and η' are connected through the magnification M of the imaging optics as $M\sin\eta' = n\sin\eta$. δz is the amount of defocusing. The light intensity on the CCD chip can be determined from the z-component of the Poynting vector.

$$S = \frac{c}{8\pi}\boldsymbol{e_z}\cdot(\boldsymbol{E}\times\boldsymbol{B}^*)$$

This intensity pattern (S) is used to fit the recorded images using a least square fitting algorithm[14] to extract the orientation information.

3.2 Projection of Emission Intensity on 2D Detector

Figure 3 shows a dipole oriented at an angle θ with respect to the z axis which is the optical axis and at an azimuthal angle ϕ. Defocusing is done along the optical axis. The emission patterns for dipoles oriented at various angles (θ, ϕ) and for various amounts of defocusing can be theoretically calculated. Various simulated emission patterns are shown in **Figure 3** and **Figure 4**. When dipole direction

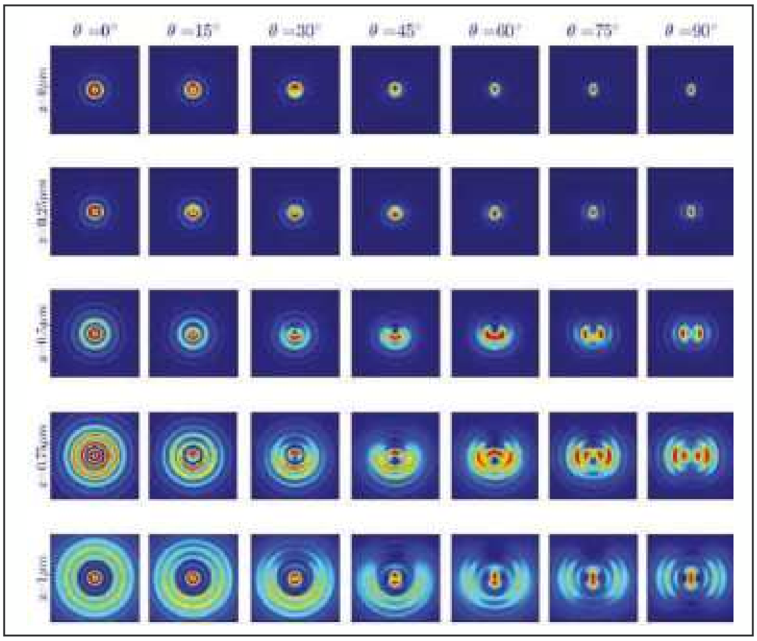

Figure 3: *Simulated dipole emission patterns for various axial angles θ under various amounts of defocusing (z values) for ϕ = 90°.*

is along x axis i.e. $\theta = 90°$ from the optical axis and ϕ = 0°, the observed emission pattern of such alignment is doughnut like distribution. And when, dipole is along the optical axis, i.e. $\theta = 0°$ and $\phi = 0°$ emission pattern observed in such alignment is circular ring field around the dipole axis. Under focused condition we miss these fine emission patterns, but under defocused condition the rather outward emission fields are collected in to the higher refractive index media. That is, dipole emission field in water media of n = 1.33 are efficiently collected into the cover-slip (of n> 1.5) and relayed to the objective for projection onto detector. Different polar and azimuthal angles will result in different emission pattern of the respective oscillating dipole

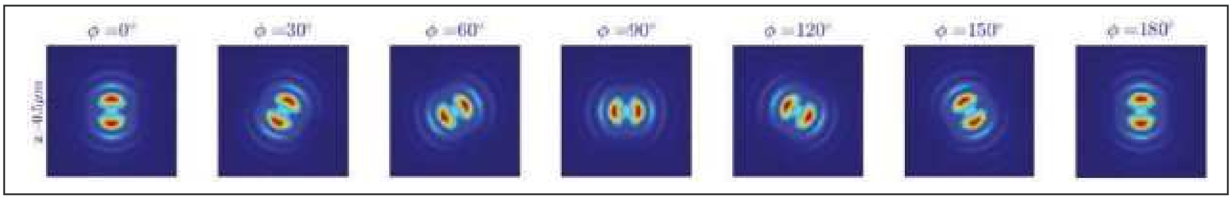

Figure 4: *Simulated dipole emission patterns for various azimuthal angles ϕ at a particular defocusing (z = 0.5 μm).*

In practice, it is these patterns that are imaged on to a CCD camera. It is clearly visible that, as θ changes the emission pattern of the circular fringes, becomes dark because the dipole orientation going away from optical axis and, when it became 90° to the optical axis, the doughnut shape pattern was visible. Change in ϕ shows how the dipole orientation changes in the plane.

4. Results and Discussion

4.1 Demonstration of Dipole Orientation Imaging with RhB

First we checked our home build setup for orientation imaging under defocused condition, and for that we recorded images of RhB in PVA matrix, spin coated on a cover slip. The sample is moved in the z-direction from the focus by a distance of -0.7 μm using a motorized scanner and defocused images are recorded. The recorded images were parametrically fitted with the calculated images (shown above) taking the angles θ and ϕ as fitting parameters. The best fit parameters obtained by a least square fitting algorithm[14] gives the location and orientation angles of the dipole. The recorded and fitted images are shown in **Figure 5**.

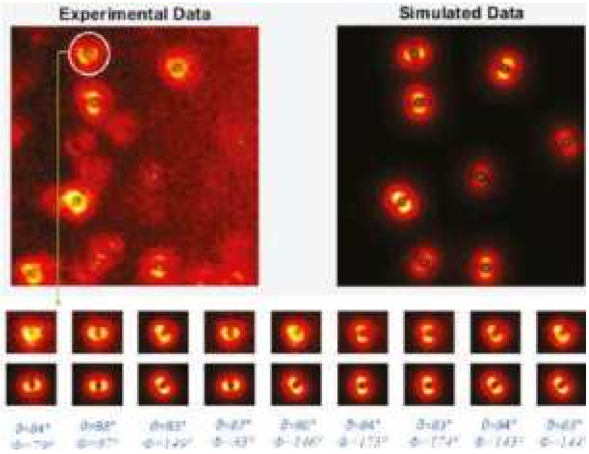

Figure 5: *Defocused fluorescence image of RhB (in PVA solution) coated onto No. 1 thickness cover slip is shown on top left. The theoretically simulated pattern for this recorded image is shown on the top right corner. The green dots represent the localization point for individual dipoles. The reorientation motion of a dye (marked with white circle) as observed in different time frames are shown in the bottom panel (both experimental and stimulated image). The corresponding values of θ and ϕ, obtained from pattern matching algorithm are mentioned below the individual dipole images.*

4.2 Orientation Imaging NR Bound to Fibril Structures

Wide field image of fibril in TIRF condition is shown in **Figure 6a**. Theoretical data fitting of small region of the wide field image is done by Gaussian function fitting, results in super resolved fibril structure under transient dye binding condition, cf. **Figure 6b**.

Confocal intensity and lifetime images of fibril stained with NR are shown in **Figure 7**. The lifetime of NR in all the samples were observed to be single exponential in the range of 3.0 - 3.5 ns. This indicates that hydrophobic surface on fibril where NR binds is not appreciably different. In **Figure 7** right graph show the decay curve of the marked area and also the lifetime distribution of the whole region.

To record the dipole orientation of dyes residing on fibril structures, we first recorded the wide-field image, shown in left side images in **Figure 8 & 9**. After selecting a region, we record images by defocusing into the solution by around 500 nm. This ensures that maximum of emission field from the single dipole is collected through the high refractive index media (cover slip) and projected on to the CCD. A representative defocused image, showing the emission patterns are shown in the right side in **Figure 8 & 9**.

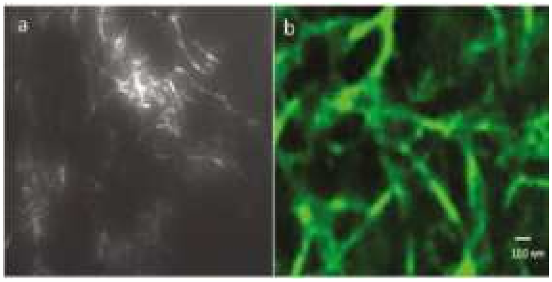

***Figure 6**: Wide field image of fibril labeled with 50 nM NR (CW 532 nm, TIRF excitation) is shown on left. The right side image represents the final processed super-resolved image (following SMLM-TAB scheme) of a small region of fibril under transient binding condition with <10 nM NR. 10,000 frames were recorded with single molecule PSF density of around 5-10 per 10 μm^2 image area. Localization of each PSF with sub-pixel accuracy was performed in ImageJ (inset) and super-resolved image was constructed by stacking these 10,000 frames. With our setup, we could resolve structures up to 50 nm. 100x NA 1.46 oil immersion objective with cover slip of No. 1 thickness was used for imaging.*

Our orientation measurements indicate mostly in-plane polar angles ($\theta \approx 90°$) with azimuthal orientations (ϕ) aligned to the long axis of amyloid for NR dye. These results suggest that NR molecules preferentially bind to surfaces of β-sheets with their transition dipoles parallel to

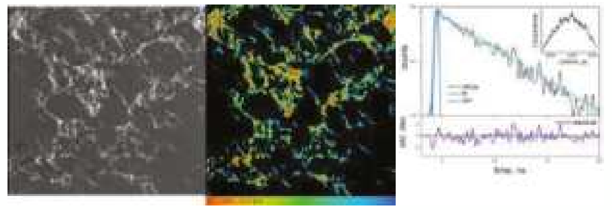

Figure 7: *Confocal Fluorescence-lifetime imaging microscopy (FLIM) of fibril stained with NR using pulsed in-tune 535 nm excitation (pulse width < 10 ps, < 10 μW, pinhole 100 μm, Dichroic 535c, LongPass 635 nm) and Hybrid PMT as detector. The pixel and microtimes were recorded with photon counting card SPC-154. Lifetime images were analysed with B&H simpleTAU routines. Decay curve of the marked region (red circle on FLIM image) along with life time distribution of the whole region is shown in right.*

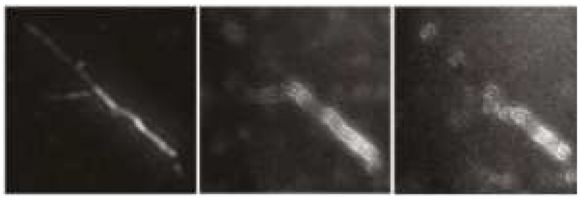

Figure 8: *Wide field image of fibril labelled with 50 nM NR (CW 532 nm, TIRF excitation) is shown on left. The others are defocussed image of the same fibril. To observe the single dipoles from a relatively bright region, we made time series of defocused images and tried to see their random blinking in some of the frames, which are well separated to analyze their individual patterns to extract angular coordinates.*

the fibril backbones. Further analysis of data to ascertain the distribution of dye orientation with respect to the fibril axis is underway. Advanced setup with improved S/N for faster acquisition is under development.

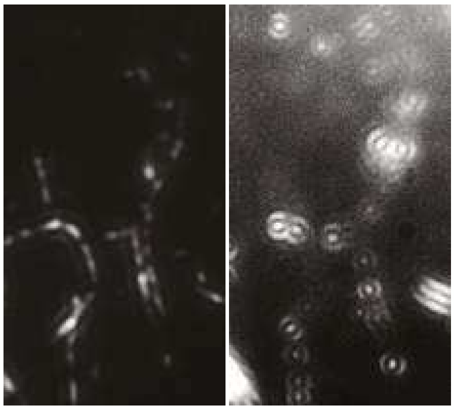

Figure 9: *Wide field image of fibril labelled with 50 nM NR (CW 532 nm, TIRF excitation) is shown on left. And right image is defocused pattern of the emission field.*

5. Conclusion

To explore the binding of dye on ordered structures like fibril we have used advance imaging methods. Dipole orientation of RhB dyes were first recorded and characterized. Different fibril samples were prepared and viewed them under the fluorescence microscope. It has been observed that surface chemical environment is similar in all the prepared fibrils. Defocused imaging experiments with fibril using NR clearly indicate preferential sticking along the fibril axis. Further analysis for their binding orientation is under investigation.

6. Acknowledgements

This work is supported by DAE, India. Authors acknowledge all the co-authors and collaborators of our published works cited in the references. We thank Dr. A. C. Bhasikuttan, Head, MPS, RPCD and Dr. Awadhesh Kumar, Head, RPCD, BARC, for their encouragement and support. Authors also acknowledge the encouragement received from Drs. H. Pal, D. K. Palit, P. D. Naik, A. K. Tyagi, B. N. Jagtap, S. K. Sarkar, T. Mukherjee and J. P. Mittal.

References

1. Betzig, E.; Patterson, G. H.; Sougrat, R.; Lindwasser, O. W.; Olenych, S.; Bonifacino, J. S.; Davidson, M. W.; Lippincott-Schwartz, J.; Hess, H. F. *Science* 2006, 313, 1642-1645.
2. Rust, M. J.; Bates, B.; Zhuang, X. *Nat. Methods* 2006, 3, 793-795.
3. Linde, S. v. d.; Löschberger, A.; Klein, T.; Heidbreder, M.; Wolter, S.; Heilemann, M.; Sauer, M. *Nat. Protocols* 2011, 6, 991-1009.
4. Yildiz, A.; Forkey, J. N.; McKinney, S. A.; Ha, T.; Goldman, Y. E.; Selvin, P. R. *Science* 2003, 300, 2061-2065.
5. Jasny, J.; Sepiol, J. *Chem. Phys. Lett.* 1997, 273, 439-443.
6. Bartko, A. P.; Dickson, R. M. *J. Phys. Chem. B* 1999, 103, 3053-3056.
7. Sepiol, J.; Jasny, J.; Keller, J.; Wild, U. P. *Chem. Phys. Lett.* 1997, 273, 444-448.
8. Toprak, E.; Enderlein, J.; Syed, S.; McKinney, S. A.; Petschek, R. G.; Ha, T.; Goldman, Y. E.; Selvin, P. R. *Proc. Natl. Acad. Sci.* 2005, 103, 6495-6499.
9. Shaban, H. A.; Valades-Cruz, C. A.; Savatier, J.; Brasselet, S. *Sci. Reports* 2017, 7, 12482.
10. Spehar, K.; Ding, T.; Sun, Y.; Kedia, N.; Lu, J.; Nahass, G. R.; Lew, M. D.; Bieschke, J. *Chembiochem* 2018, 19, 1944-1948.
11. Takai, E.; Ohashi, G.; Ueki, R.; Yamada, Y.; Fujita, J.-I.; Shiraki, K. *Am. J. Biochem. Biotech.* 2014, 10, 31-39.
12. Böhmer, M.; Enderlein, J. *J. Opt. Soc. Am. B* 2003, 20, 554-559.
13. Enderlein, J. *Opt. Lett.* 2000, 25, 634-636.
14. Patra, D.; Gregor, I.; Enderlein, J. *J. Phys. Chem. A* 2004, 108, 6836-6841.

About the authors

Aranyak Sarkar *obtained his Master's degree in Physics from the IIT Kanpur in 2013 and joined RPC Division, BARC in 2016. He is currently pursuing research for his PhD degree in Chemistry from Homi Bhabha National Institute, Mumbai under the supervision of Dr. Manoj Kumbhakar, RPCD, BARC, since 2019. His research interests include advance single molecule fluorescence spectroscopy and functional super-resolution imaging for bio-speciation of lanthanides and actinides.*

Sonali Gupta *obtained her Master's degree in Chemistry from the Mumbai University in 2018 and joined Homi Bhabha National Institute, Mumbai for PhD degree in Chemistry. She got introduced to the field of single molecule fluorescence spectroscopy under the supervision of Dr. Manoj Kumbhakar, RPCD, BARC. She is currently working for her PhD with Dr. K. C. Barick, ChD, BARC.*

Vinu V. Namboodiri *obtained his PhD in physics from Jacobs University Bremen, Germany in 2010 under the supervision of Prof. Arnulf Materny. He was awarded IISc post-doctoral research associateship in the same year and joined the laser spectroscopy group under Prof. Siva Umapathy. He joined as a KSKRA fellow in BARC in the year 2013. His research interests include theoretical & experimental ultrafast spectroscopy, coherent control, fluorescence spectroscopy & imaging.*

Manoj Kumbhakar *joined RPC Division, BARC, in 2001 and obtained PhD degree in 2008 from University of Mumbai. He is an Alexander von Humboldt Fellow for postdoctoral research for the period 2010-2012. His recent research interests include bio-speciation and bio-sequestration of lanthanides and actinides using single molecule fluorescence spectroscopy and super-resolution imaging. He is the recipient of the Homi Bhabha Award in Chemistry for the year 2000–2001, the National Academy of Sciences, India, Young Scientist Award in 2007, the Department of Atomic Energy Young Scientist Award in 2008, and the Indian National Science Academy Young Scientist Award in 2010.*

INDIAN SOCIETY FOR RADIATION AND PHOTOCHEMICAL SCIENCES
(Reg. No. 617/1985, GBBSD, Bombay; Trust No. F-10965)
Radiation & Photochemistry Division
Bhabha Atomic Research Centre, Mumbai - 400 085

Member Enrolment Form

Photograph

1. Name in Block Letters:
2. Date of Birth:
3. Highest Academic Qualification:
4. Present Position:
5. Addresses:

Office	Residence
  Telephone E-mail	 Telephone E-mail

6. Address for Correspondence: Office / Residence
7. Category of Membership Applied for: Annual / Life /Corporate member
8. Remittance: DD in favour of 'ISRAPS' payable at MUMBAI
   For Bank Transfer:
   A/c No.10536133801, SBI, BARC Branch, IFSC SBIN0001268
   (e-mail the money transfer details along with the details requested above to
   israps.secretary@gmail.com and CC to jyotim@barc.gov.in)

Category	Fees	Admission fee	Total Amount
Annual	Rs 200/-	Rs 100/-	Rs 300/-
Life Member	Rs 1500/-	Rs 100/-	Rs 1600/-
Corporate Member	Rs 20000/-	Rs 1000/-	Rs 21000/-

9. Brief Resume of activities and research interests:
10. List of memberships of other professional bodies, if any:
11. List of prizes/awards/fellowships received, if any:
12. Number of Publications:

I agree to abide by the constitution and bye-laws, and rules and regulations of the SOCIETY.

Place:

Signature

Date:


New Launch:
Water LC-MS
Grade
Water LC-MS
ADVENT
CAS No. [7732-18-5]
M.F.: H_2O
FW : 18.02
Product Code : 98717 - 4 L
Pack : 4 L
Water LC-MS
ADVENT


ADVENT
CHEMBIO PVT. LTD.

For Limited Circulation Only

ATOS ATOSCOPE

HYPERSPECTRAL IMAGING DETECTORS CCD TUNABLE LASERS SCMOS INFRARED MULTISPECTRAL COOLED NITROGEN LITTROW CRYOSTATS ASTRONOMY HELIUM LITTMAN/METCALF SOLAR CELL CONFOCAL ANALYTICS INSTRUMENTATION SPECTROGRAPHS MICROSCOPY GAS MIXERS NANOTECHNOLOGY METROLOGY LIDAR EMCCD UV VACUUM THERMOGRAPHY MONOCHROMATORS UNCOOLED SCIENTIFIC ICCD LIQUEFIERS CRYOGENICS THERMICS QUANTUM XRAY VIS FEMTO MEMS PICO TESTING SWIR DIODE SIMULATORS SURVEYING DYNAMIC DIAGNOSTICS PULSED TERAHERTZ NDT COMPRESSORS MICROFLUIDICS

ANDOR

Ultrafast ICCD detectors, High resolution spectrographs, Imaging accessories, Raman, Fluorescence, Micro spectroscopy (UV-VIS-NIR), Plasma spectroscopy

Stinger ColdEdge

Cryostats for Optical/Electrical/Magnetic measurements.

4K Closed Cycle Cooling System with ultra low vibration, Customized designs

Sacher Lasertechnik

Tunable Diode Lasers – Littrow & Littman
External & Vertical Cavity Surface Emitting
Tera Hertz & Quantum Cascade Lasers

FYLA WE LASER THE NEW INDUSTRY

Supercontinuum white light lasers Femto , Pico & Nano second pulse width laser and accessories very high Power, MHz repetition rates.

mcq instruments

Gas mixing &
dilutions solutions.
Software controlled
With feedback.

OXFORD INSTRUMENTS

Flow Cryostats for 3K and 77K measurements with ultra-low vibration system. Cryogen free cryostats for 4K measurements.

ATOS Instruments Marketing Services

ATOSCOPE Instruments Pvt. Ltd.

www.atosindia.com Tel: 9148195382 atos@atosindia.com